

GEOF 271

Processing of earthquake data

Jens Havskov
jens@geo.uib.no

Department of Earth Science
University of Bergen
Norway

September 2006

Introduction

The purpose of this course is to get a practical understanding of the most common processing techniques in earthquake seismology. The course will deal with manual methods and computer assisted methods, although most exercises are computer based.

In order to follow the course, the student must have basic seismological knowledge based on 'Modern Global Seismology', by Lay and Wallace or 'An introduction to seismology, earthquakes and earth structure' by Seth Stein and Michael Wysession as given in the course GEOF270. The two courses are given in parallel with the intention that the student follow both courses at the same time in order to get practical hands on experience while studying the background for the exercises. The main background material is thus covered in Lay and Wallace or Stein and Wysession, while additional material and similar material is given in these notes.

The SEISAN software is used for the computer processing and a SEISAN manual is required. The software, including manual and training course, can be downloaded from http://www.geo.uib.no/Seismologi/SOFTWARE/SEISAN_8.1/. The software should be installed on the student's local PC before starting the exercises since it will be used throughout.

A written report has to be made for each exercise and the reports count for 50 % of the course grade.

There are 10 exercises covering the topics:

- 1 Seismic phases and the Wadati diagram.
- 2 Manual earthquake location and earthquake catalogs
- 3 SEISAN: Seismic data in the computer: Data bases, epicenter maps and digital waveform data
- 4 Picking phases and doing earthquake location by computer
- 5 Seismograms and response functions
- 6 Magnitude and b-value
- 7 Using a single station or array for azimuth determination and earthquake location
- 8 Fault plane solution
- 9 Spectral analysis
- 10 Analysis of a set of local events

Additional material included:

Seismic phases, Kulhanec	p	43
Selected NMSOP (Bormann, 2002) notes and exercises:		
Section IS 11.1 Earthquake location	p	87
Section 3.4 Fault plane solution	p	117
Section Ex 3.2 Exercise in fault plane solution	p	131
Section Ex 3.4 Exercise in spectral analysis	p	139

Other material

At (http://www.geo.uib.no/Seismologi/SOFTWARE/SEISAN_8.1.2/)
SEISAN Version 8.1 – introductory training course

At http://www.geo.uib.no/seismo/REPORTS/COURSE_MATERIAL/
Bullen travel time tables
Old exams

Pensum: Mainly the result of the exercises and the material in this document.

This document found at http://www.geo.uib.no/seismo/REPORTS/COURSE_MATERIAL/

EXERCISE 1

Seismic phases and Wadati diagram

The purpose of this exercise is to become familiar with analog seismograms, identify basic seismic phases and use the Wadati diagram for checking the observations and calculate the V_p/V_s velocity ratio.

For this exercise, SEISAN program lsq can be used for least squares.

Exercise 1

Calculate V_p/V_s using travel time tables

Use the travel time table for crustal phases in Kulhanek, p53. Assume a constant velocity, calculate the corresponding V_p/V_s values for Pg/Sg, P*/S* and Pn/Sn at a 160 km's distance.

-How do they compare, explain any differences.

-Calculate the average P-velocities for the 3 types of phases at 160 km epicentral distance.

-Plot the travel time curves and calculate the true Pn and P* velocities from the slope of the curve.

-Explain the differences with the average velocities.

Exercise 2

Read local seismic phases and make a Wadati diagram (see Appendix 2, IS 11.1)

Figure 1.1 shows a seismogram with traces of some stations. Read the P and S-arrival times for all stations, assume all to be first arrivals (just P and S).

-Make a table of the readings.

-Make a Wadati diagram to determine if the readings are reasonable. Put station names on the plot.

-One of the stations probably has a timing problem (on the plot, the point representing the station is off the line). Which station? How much is the error?

-Determine V_p/V_s , is it reasonable?

-Determine the origin time (measuring on graph is easiest).

Exercise 3

Read global seismic phases

Figures 1.2 and 1.3 show LP Z seismograms for 2 different events. The goal of the exercise is to determine as many phases as possible using the Bullen tables and/or travel-time figures.

One event is shallow and one is deep. Some idea of the depth might be obtained by comparing the surface waves, since a shallow event will have larger amplitude surface wave relative to P and S waves than a deep event.

-For the shallow event, identify prominent phases on the seismograms and transfer the arrival times to a strip of paper which has the same time scale as one of the figures of the travel time

curves (Figure 1.4, figure in Bullen, also found in text books). Slide the strip of paper to different distances in order to fit as many phases as possible, see Figure 1.5. Once the best fit is obtained, write the names of the identified phases on the seismograms.

- For the deep one event, identify the pP phase (assuming it to be the first phases after P) and find the depth (assume a distance of 51 degrees). Then identify other phases using the Bullen tables or TTIM program.

-Determine the origin time for both events and epicentral distance for the shallow event using the Bullen travel time table.

Exercise 4

Calculate travel times with a program

The program TTIM in SEISAN calculates travel times using the IASP91 traveltime tables. These calculations should be more accurate than the Bullen travel times. Note that the program uses distance in degrees, not km. One degree is 111.1 km.

-Compare the traveltimes for at least 5 different phases identified above as calculated with the Bullen tables and the IASP91 tables. Use the approximate distance calculated above

-What is the % difference in travel times.

Use the Kulhanec (p 53) travel time table for Sweden and read travel times at 250 km distance.

-Make a table with the crustal phases Pg, Pn and Pb(P*), Sg, Sn and Sb. Compare travel times to IASP91 times and give difference in % of travel times.

-Which crust is the fastest, IASP91 or Sweden

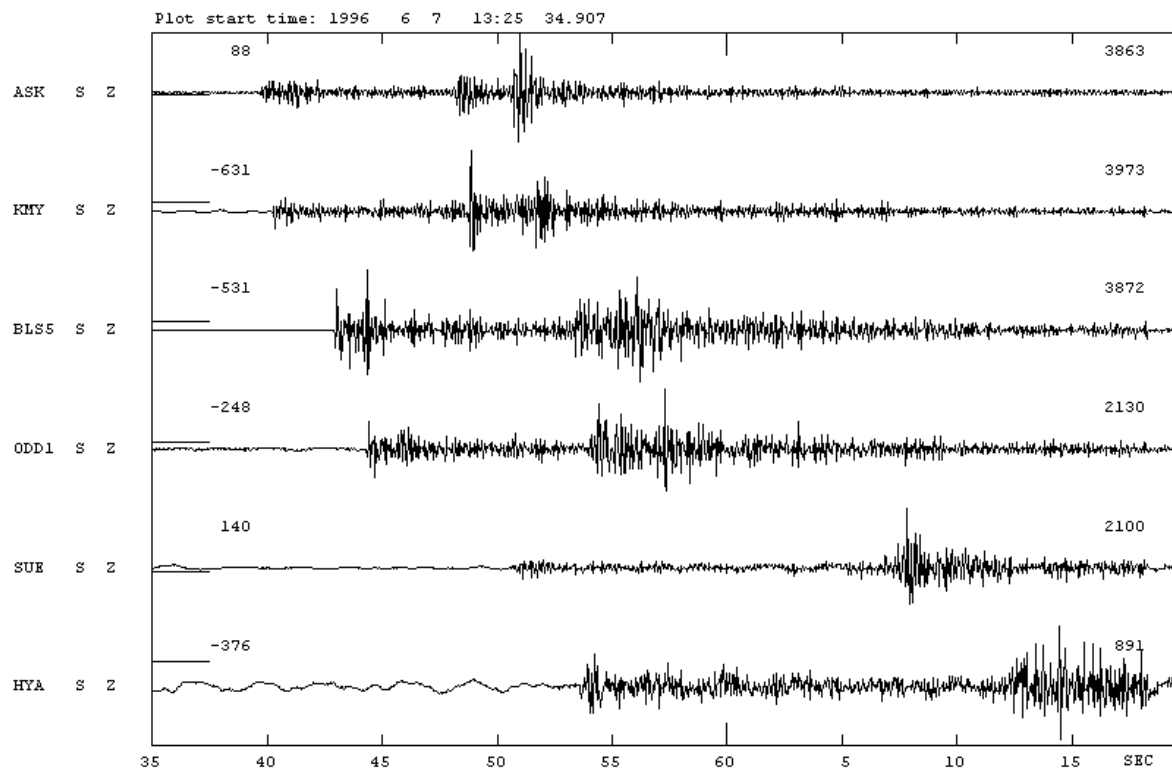


Figure 1 A seismogram of a local earthquake in Western Norway. The numbers above the traces to the right is the maximum count and the numbers to the left are the DC values (counts). The time scale on the printed page is 3 mm/s.

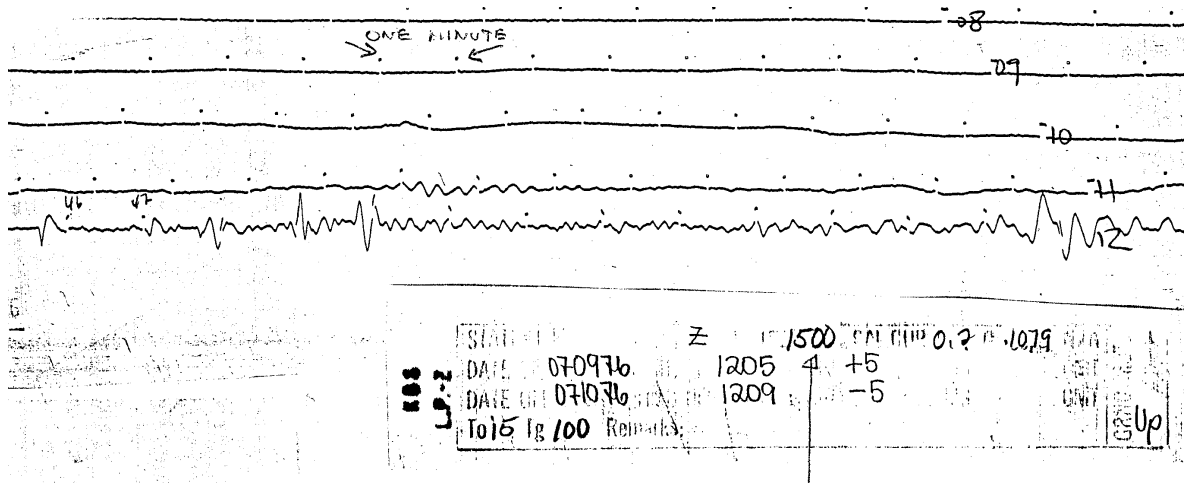


Figure 1.2 LP seismogram. The figure shows the seismogram of distant earthquake recorded on the WWSSN photographic system. The gain is 1500. The hand written numbers are hour marks and there is one minute between dots. The time scale on the printed page is 10 mm/min.

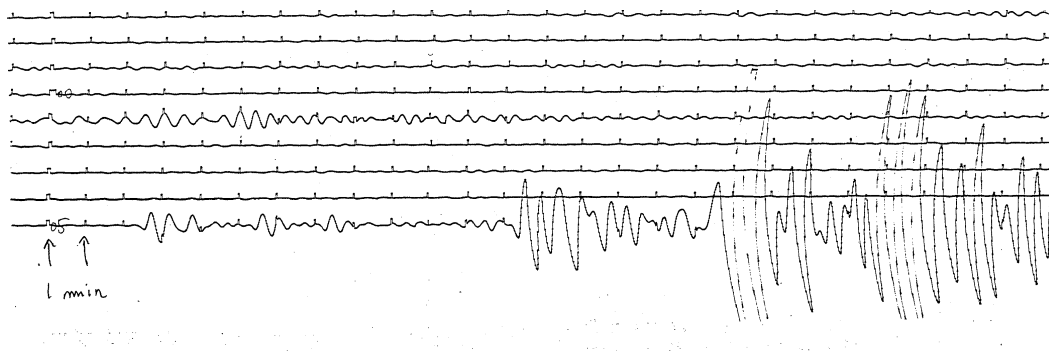


Figure 1.3 LP seismogram. The figure shows a LP seismogram of a distant earthquake. The distance between the dots is one minute. The time scale on the printed page is 5 mm/min.

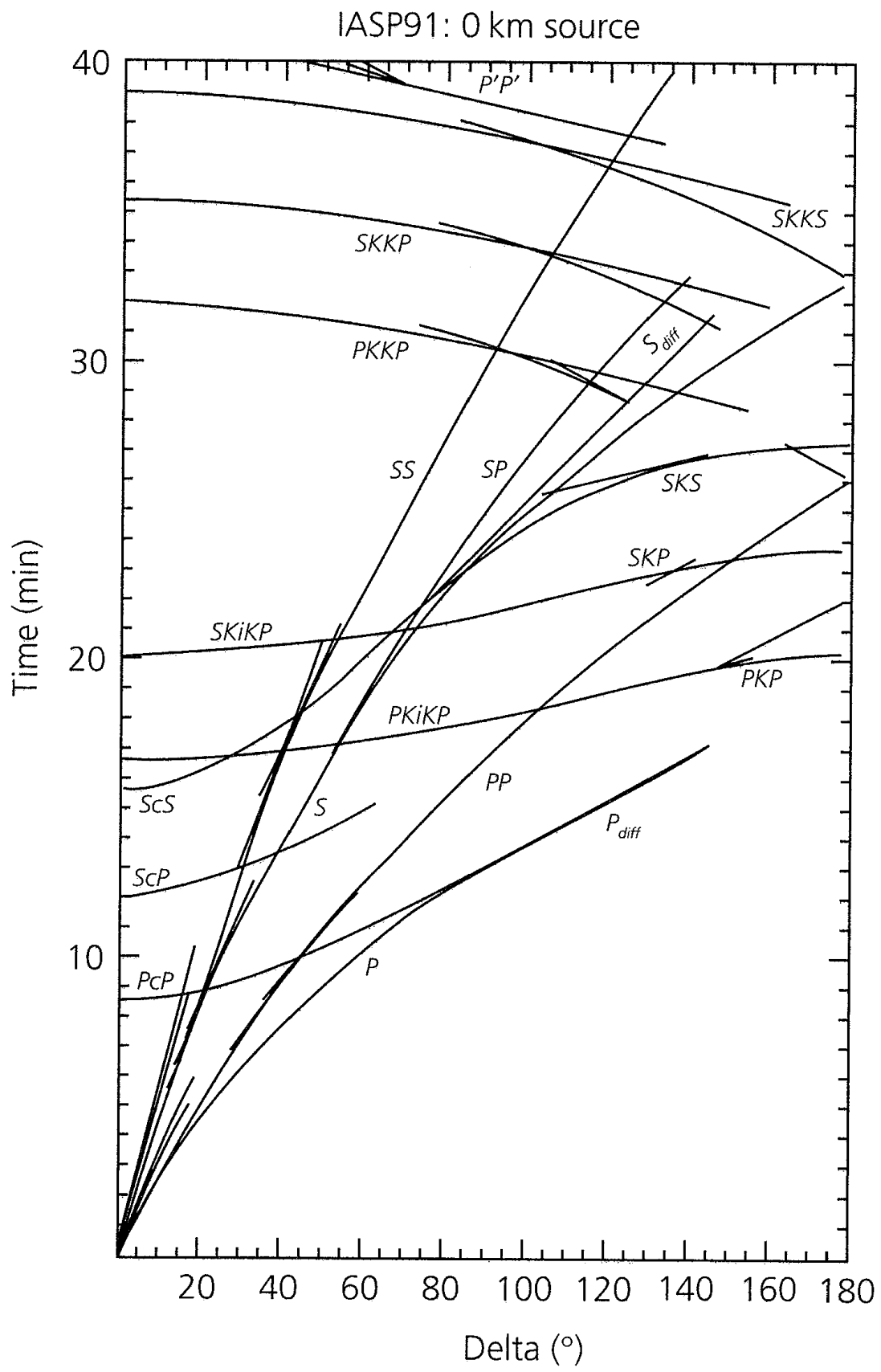


Figure 1.4 Global travel time curves for a shallow source

EXERCISE 2

Manual earthquake location and earthquake catalogs

In this exercise, the purpose is to get familiar with the most basic earthquake parameters, the earthquake location. The first exercise deals with manual location of a local earthquake using S-P times while the second exercise shows how to get data from international data bases.

Exercise 1

Manual location using S-P times

Use the arrival times read for the local event in exercise 1.

- Assuming a P-wave velocity of 7.0 km/sec and $V_p/V_s = 1.73$, determine the distance to each station using only first arrivals and the S-P arrival times.
- Locate the earthquake by drawing circles, the station map is found in Figure 2.1.
- Evaluate the error in the epicenter location.
- Will the clock problem found for one of the station in exercise 1.2 affect the solution ?

Exercise 2

Manual location using origin time

The origin time was determined in exercise 2.1.

- Using a P-velocity of 7.0 km/sec, calculate the epicentral distances, how do they compare to the distances calculated in exercise 1 ?
- Locate the earthquake as above, how does the location compare the location in the previous exercise ?
- Will the clock problem found for one of the station in exercise 1.2 affect the solution ?

Exercise 3

Get data from international data bases

The most comprehensive location for information about epicenters anywhere in the world is the International Seismological Center (ISC). Connect to ISC www.isc.ac.uk.

- Select events in are 59-62 N and 0-10 E for the time period January to June, 1999
- Make a map of the epicenters.
- Extract the readings for the first event in the list
- Repeat above for events in an area of your own interest

Connect to the USGS earthquake information system <http://neic.usgs.gov/>.

- Find list of most recent earthquakes, print map
- Find largest earthquake in the last 5 days, give detailed information

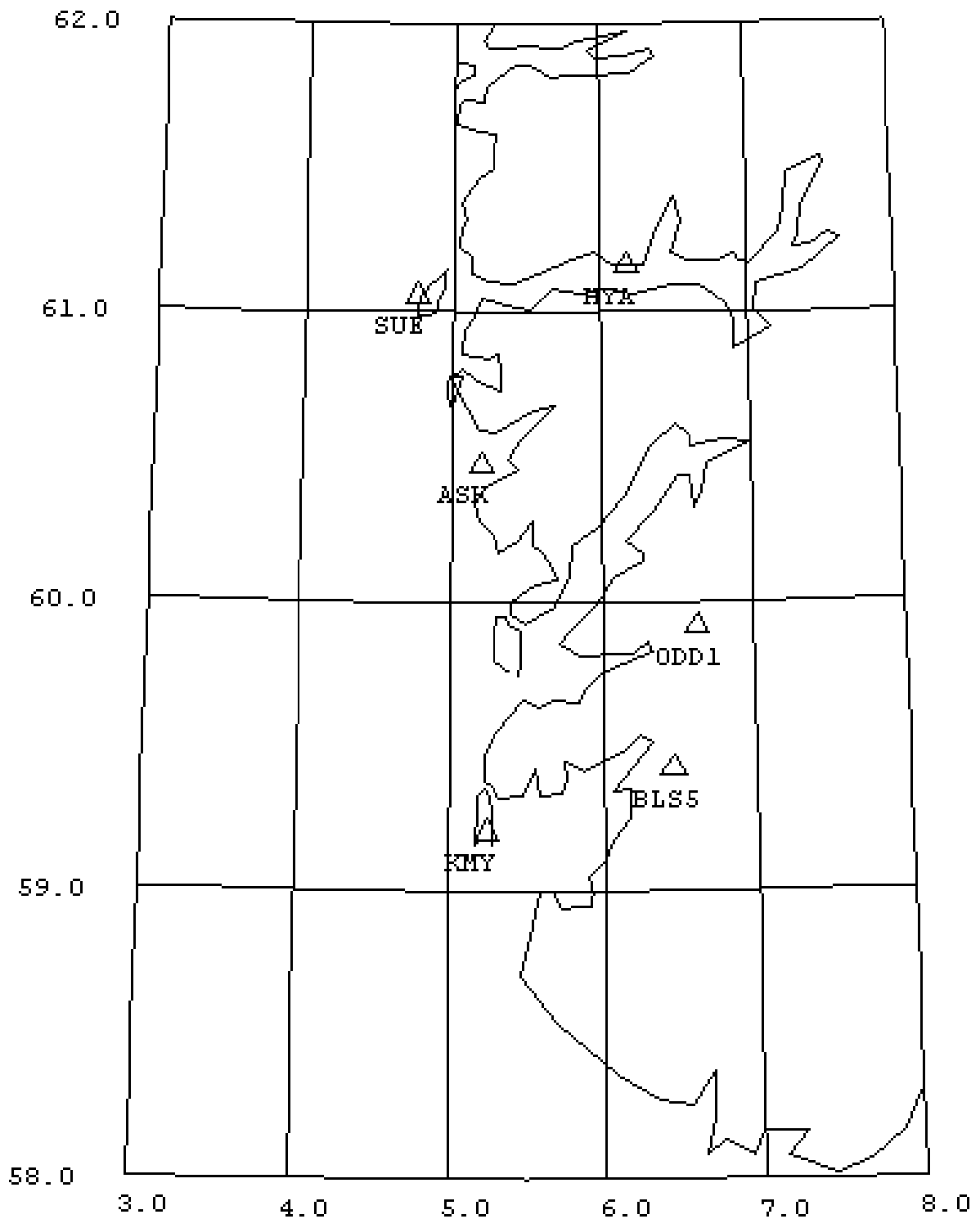


Figure 2.1 Station map. Location of some of the stations in Western Norway. The map has the same scale in y and x the scale can be determined knowing that one deg latitude is 111 km.

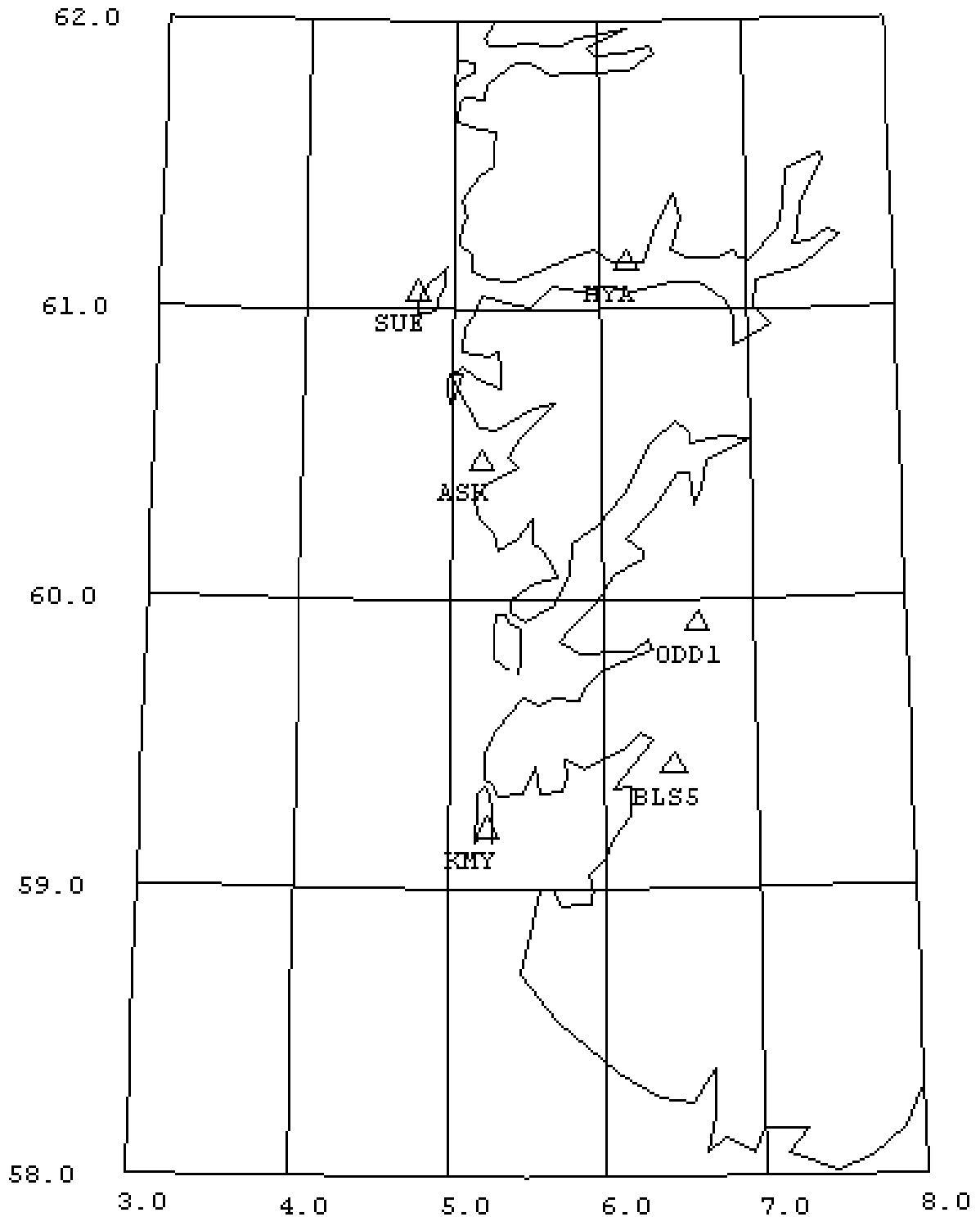


Figure 2.1 EXTRA COPY. Station map. Location of some of the stations in Western Norway. The map has the same scale in y and x the scale can be determined knowing that one deg latitude is 111 km.

EXERCISE 3

Introduction to SEISAN

This exercise has the purpose to get an introduction to how to use computers for data processing. In previous exercises, some of the basic parameters have been described: Seismic phases and earthquake location. Still to be described is the magnitude of seismic events, the fault plane solution and spectral parameters. These are the basic parameters. A seismic processing system must handle all these and more parameters for many events. In addition, the original seismograms are in digital form, not paper records as seen so far. The SEISAN system can store and process all of this. In this exercise the user will get an introduction to the basic data base operation and how to do simple data manipulation.

Background material: SEISAN manual and Appendix 3.

Exercise 1

The SEISAN exercises 1-4 is done. All questions must be answered and plots given in the report.

EXERCISE 4

Picking phases and doing earthquake location using the computer

Manual earthquake locations have already been done. In practice all phase picking and earthquake location is done with a computer. In this exercise, both a local and a global events will be processed doing phase picking and location. The local event is located using a flat layered crustal model while the distant event is located using the IASP91 travel time table.

Exercise 1

-Do all exercises in SEISAN exercise 5, answer all questions.

Exercise 2

-Do SEISAN exercise 12, 'Wadati diagram'

EXERCISE 5

SEISMOGRAMS AND RESPONSE FUNCTION

Raw seismograms do not record the ground motion in displacement, velocity or acceleration directly. The aim of the exercise is to calculate true ground motion from seismograms.

Seismic instruments can be divided into analog and digital instruments. In this exercise we will first deal with analog seismographs, then with digital instruments.

The seismograph can be understood as a linear system where the input is the ground motion (displacement) and the output is the displacement on the seismogram. This can be visualized as follows

Input of ground motion --> seismograph --> seismogram

Mathematically we can write:

$$A_{out}(f) = A_{in}(f) * Gain(f)$$

where A_{out} is the output amplitude, A_{in} the input amplitude and $Gain$ the gain of the seismograph, all values are frequency dependent. A typical gain curve for a classical analog seismograph is seen in Figure 5.2. The analog seismograph will consist of several elements each contributing to the gain, however the combined gain curve is often what is given. In the exercise, we know A_{out} and can therefore calculate A_{in} as

$$A_{in}(f) = A_{out}(f)/Gain(f)$$

Digital seismographs can in principle be described in a similar way giving just one gain curve. Since digital systems has the possibility to digitally process the data, the gain curve or gain function will normally be complex to take into account the phase response. In this exercise we will calculate the gain function using the individual elements of the seismic system:

Ground motion -> seismometer -> amplifier -> filter -> A/D converter -> Output number

Each unit will linearly treat the signal so the complete gain for ground velocity G_v can be written:

$$G_v(f) = G_{seism}(f) * G_{amp}(f) * G_{filt}(f) * G_{conv}(f)$$

G_{seism} is the gain of the seismometer. At a given frequency the gain could have been expressed as V/m , however, almost all electrodynamic seismometers have a flat response for velocity for frequencies above the natural frequency so gain constants for seismometers are expressed in terms of gain as a function of ground velocity. The gain constant is called seismometer generator constant and has the unit of $V/(m/s)$. In a seismic system, it would also be possible to use an accelerometer as a sensor, which has a flat response for acceleration. The gain constant for an accelerometer is expressed in terms of V/g where g is the gravitational constant.

G_{amp} is the gain of the amplifier. The gain has the unit V/V (Volt in and Volt out) or number of times it amplifies. It is often expressed in dB which is $20 \cdot \log(\text{gain})$.

G_{filt} is the filter gain. In terms of amplitude it is here assumed to have unity gain, but the filter will change the phase response. The filters used here are assumed to be Butterworth filters. The filter frequency, whether it is high pass or low pass must be known as well as the steepness of the filter. The steeper the filter, the more it filters and the steepness is measured in number of poles. For a low pass filter with e.g. 2 poles, the amplitude will decay as $1/(f^2)$ when f is above the filter corner frequency. The unit is the same as for an amplifier.

G_{conv} is the gain of the A/D converter (analog to digital converter). This unit converts the analog signal to a number to be used in the following digital processing. This number is often called the count value or just counts.

Remember that the relationships between displacement, velocity and acceleration are:

$$\begin{aligned} \text{velocity} &= 2 \cdot \pi \cdot \text{displacement} \cdot f \\ \text{acceleration} &= 2 \cdot \pi \cdot \text{velocity} \cdot f \end{aligned}$$

This implies that the relationship between the gain functions for velocity and displacement, G_v is

$$G_v = G_d / 2\pi f$$

Exercise 1

Instrument correction for a LP and SP record

Figure 5.1 and 1.2 respectively gives a short period and long period records of an earthquake and the response curves are found in Figure 5.2.

- Read maximum, amplitude and corresponding period on the SP and LP seismograms.
- Using the response curve, calculate the corresponding ground displacement, velocity and acceleration. Remember to use the gain given on the seismograms to select the correct response curve (peaks at 1 and 25 secs for SP and LP respectively). Do interpolation if needed. It is convenient to calculate the amplitudes in nm or μm (micrometers).

Exercise 2

Correction of a broad band record

Figure 5.3 shows seismograms from a broad band station and Table 5.1 the response function. Calculate peak ground displacement for the earthquake by reading the maximum amplitude on the seismograms. Use the component with the largest amplitude. Note that the maximum count for each trace is shown on the seismogram.

Exercise 3

Manual gain calculation

Given a seismic station with the following characteristics;

Seismometer free period: 1.0 sec
Damping ratio 0.7
Loaded generator constant: 200 V/m/s
Amplifier gain : 10 000
Filter : A low pass filter at 30 Hz, gain 1
Recording media gain : 1000 counts/V

- Calculate manually the system gain at 10 Hz in terms of counts/(m/s) and counts/m.

Exercise 4

Correcting digitally for response

In SEISAN it is possible to remove the effect of the instrument and generate a seismogram showing displacement in nm. This is done in picking mode in mulplt. The requirement is that the response file is present in the system.

- Where is the response file and how is it made ? Print an example of the text response file.

Chose the local earthquake (June 25 3:36, 1996) and generate the true ground motion signal (option Groun). Since the instrument is short period, you cannot correct for the response down to very low frequencies and a filter must be chosen at the same time as the instrument removal is done. Make displacement, velocity and acceleration signals without a filter.

-How do the signal look, all reasonable ? If not, why ?

Use a filter 0.1 to 10 Hz and make all 3 signals.

-How do the signal compare to the above without filter ?

-How do the frequency content compare in the 3 types of signals.

Present plots of the results in your report, do not forget to put on units..

Frequency	Amplification	Phase
0.000000	0.000000	0.000000
0.010000	0.006406	350.329346
0.020000	0.084660	271.075684
0.030000	0.242995	223.886673
0.040000	0.437667	194.064651
0.050000	0.644228	173.418274
0.060000	0.852485	158.173187
0.070000	1.058805	146.361877
0.080000	1.262181	136.857971
0.090000	1.462557	128.972443
0.100000	1.660183	122.262146
0.200000	3.536685	82.503510
0.300000	5.289946	58.372360
0.400000	6.921759	38.281265
0.500000	8.409451	19.822296
0.600000	9.728251	2.184758
0.700000	10.856073	345.020508
0.800000	11.774674	328.155762
0.900000	12.470419	311.495850
1.000000	12.934443	294.986572
1.500000	11.838434	214.447144
2.000000	7.175508	142.704559
2.500000	3.439356	89.242126
3.000000	1.617056	52.226334
3.500000	0.806973	25.679688
4.000000	0.431738	5.582578
4.500000	0.245927	349.651611
5.000000	0.147779	336.556641

Table 5.1 Response curve for station NRS. The unit for the amplification is counts/nm and degrees for the phase. The frequency is in Hz.

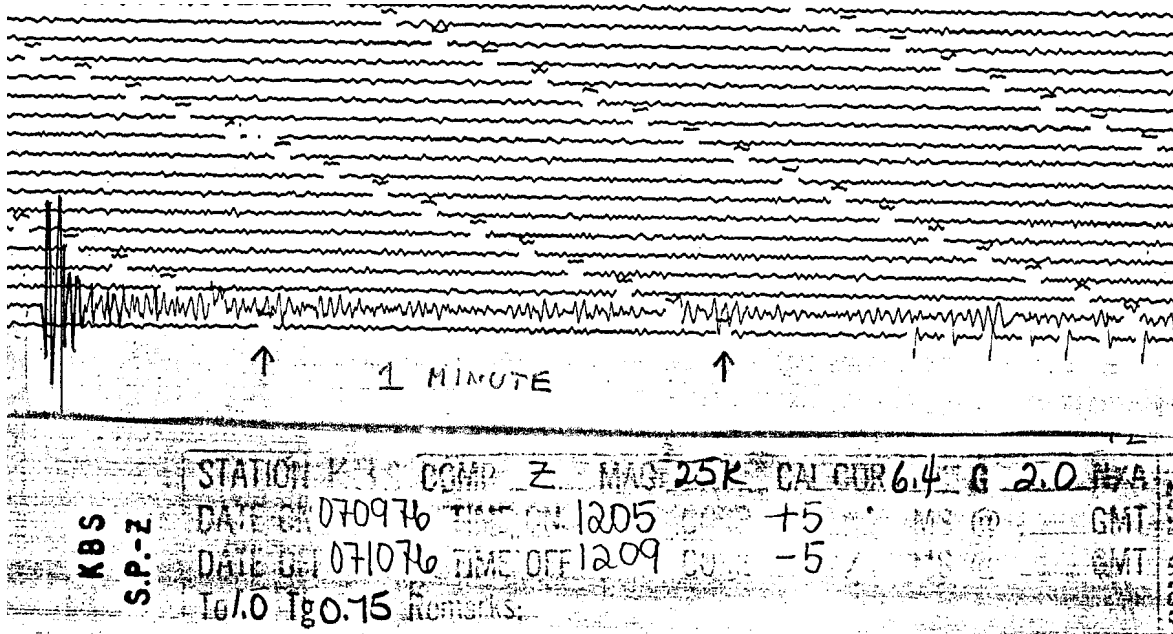


Figure 5.1 SP seismogram. The figure shows a SP seismogram from the WWSSN. The gain is 25 000. The time scale on printed paper is 60mm/min like the original seismogram.

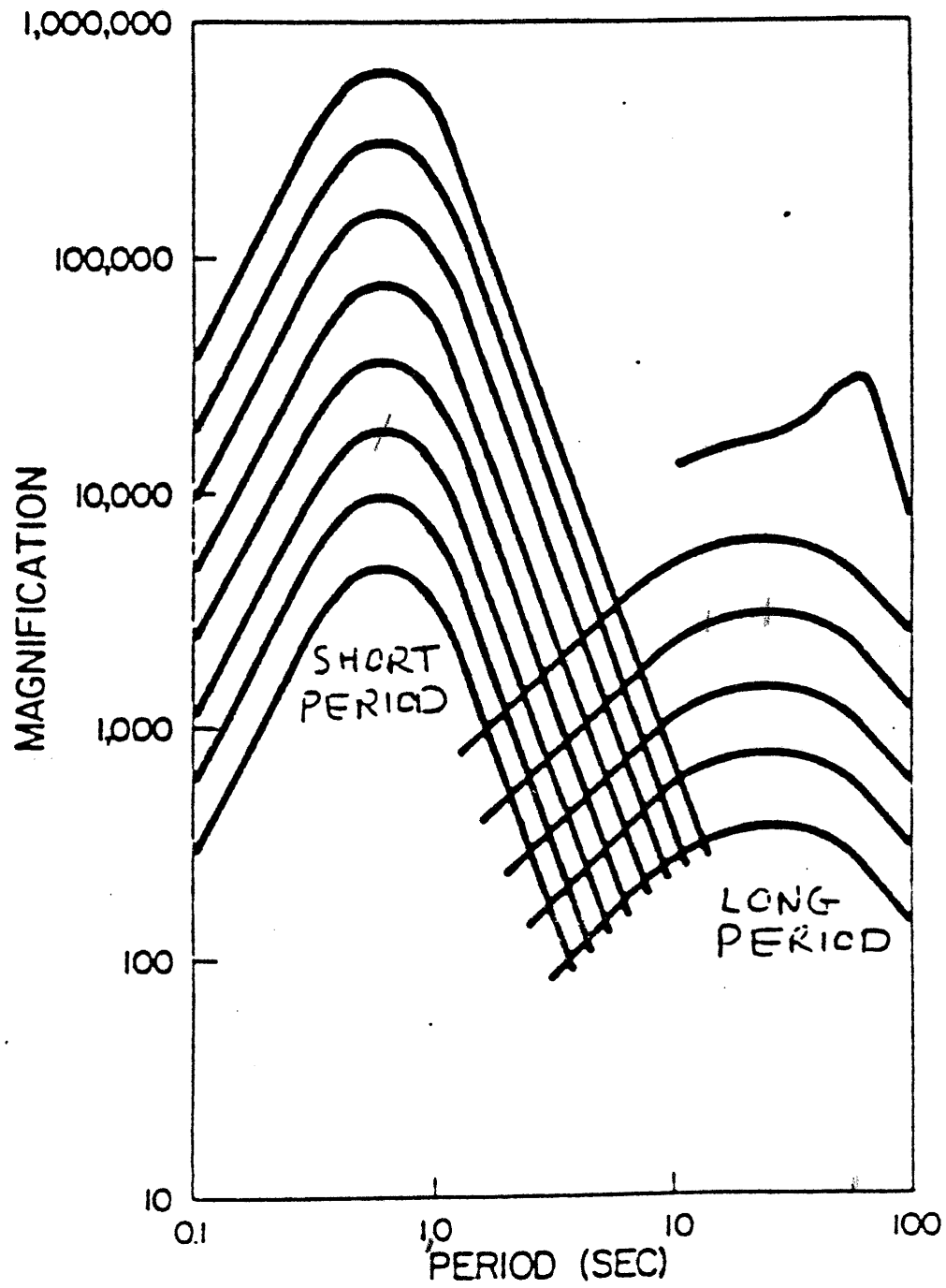


Figure 5.2 WWSSN displacement response curve. The maximum gain on the curve corresponds to the gain given on the seismogram.

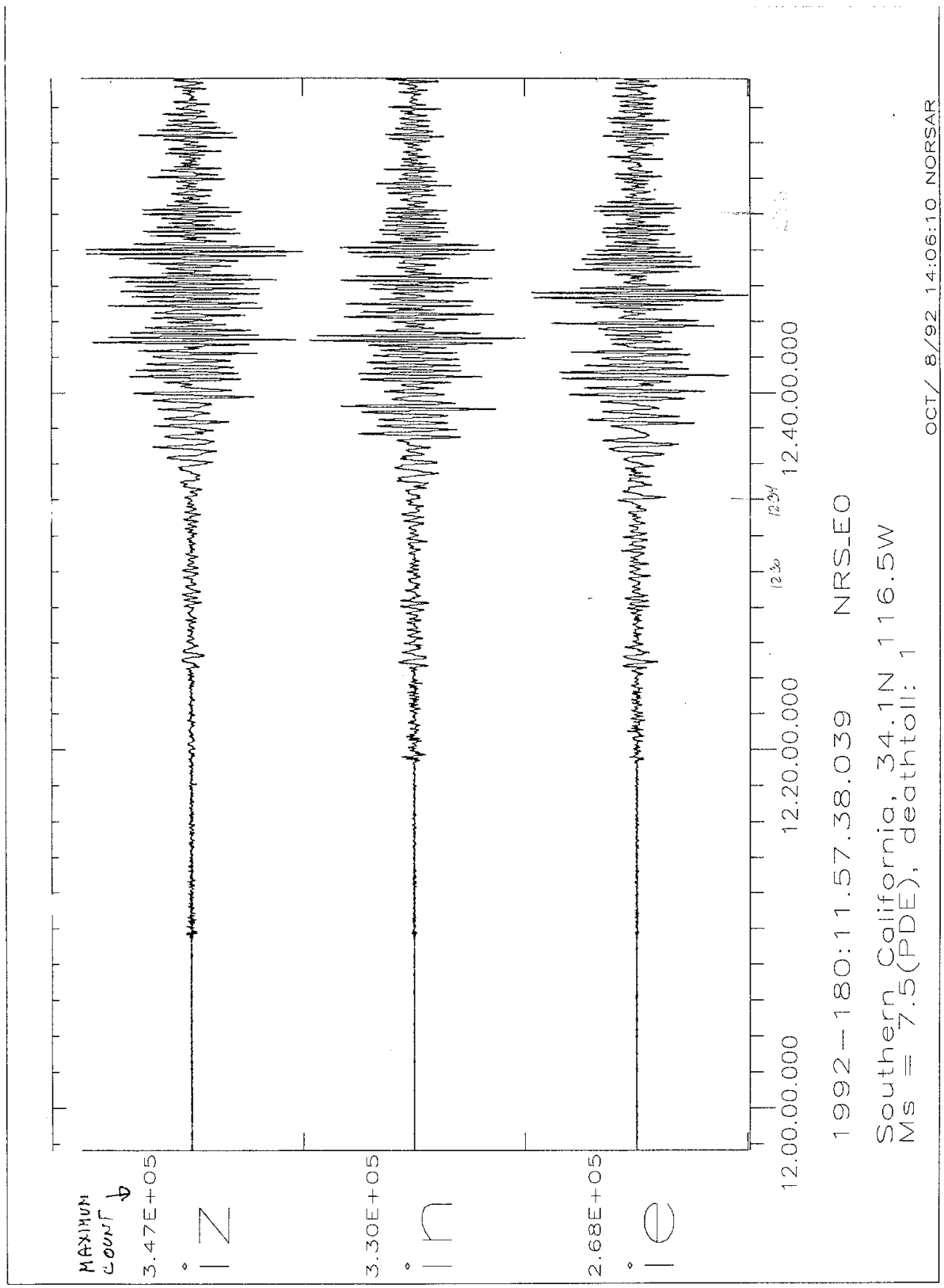


Figure 5.3 A broad band seismogram The time scale is 20 sec/mm or 2 min between ticks. The start time is June 28, 1992 at 11:57 38.039.

EXERCISE 6

MAGNITUDE AND b-VALUE

The purpose is to calculate magnitude both manually and by computer and use magnitude statistics to calculate earthquake recurrence (b-value).

Exercise 1 Coda magnitude

The simplest magnitude to use for local earthquakes is the coda magnitude (also called duration magnitude). The coda length (t_{coda}) is defined as the total duration in seconds of the earthquake recording. The end of the record is most easily seen on filtered records or if the record is zoomed near the end of the recording.

Coda waves are scattered waves radiating from the earthquake hypocenter. Figure 6.1 shows how scattered energy arrives.

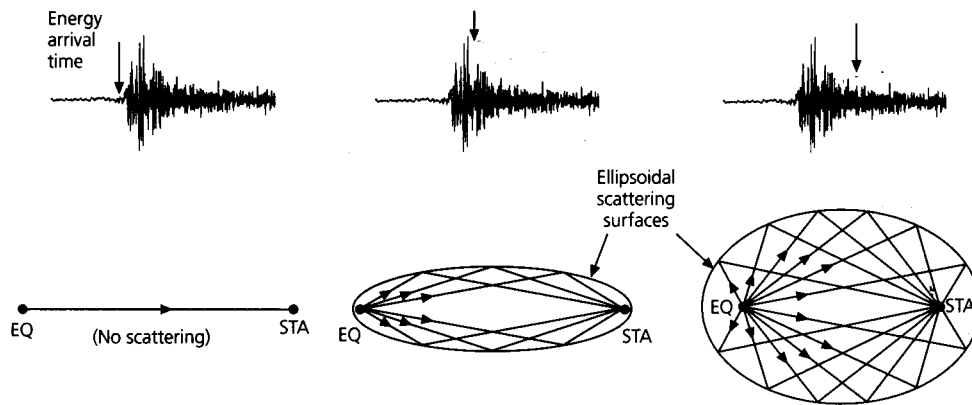


Figure 6.1 Development of P-wave coda due to scattering. Left: The energy arrives directly to the station STA from the hypocenter EQ, this is the direct P-wave. Center: Scattered energy arrives after the first P-arrival. If the scattering takes place further away (right), scattered energy arrives even later, however with a smaller amplitude.

At some time, the amplitude of the scattered arrival is smaller than the amplitude of the background noise and this is considered the end of the coda. If the initial amplitude of the signal is larger (a larger magnitude), the coda length will also be larger so this explains why the coda length is proportional to the earthquake magnitude. The strongest amplitude of the earthquake signal is the S-waves, so usually it is the S-wave scattered energy that is observed at the end of the signal.

The decay of amplitude of the scattered signal is inversely proportional to the distance it has travelled, in other words, the theoretical amplitude of the scattered will be inversely proportional to the travel time t_c of the coda wave (time from origin time t_0 to arrival time t):

$$t_c = t - t_0 \quad (6.1)$$

and ideally we should use t_c to measure the magnitude, which can be expected to only depend on t_c . The coda magnitude scale could then be expected to have the form

$$M_c = a \text{Log}(t_c) + c \quad (6.2)$$

where a and c are constants. However, the coda length t_{coda} is traditionally measured from the P-arrival time t_p to the end of the signal

$$t_{\text{coda}} = t - t_p \quad (6.3)$$

By inserting 6.1 in 6.3 we then get

$$t_{\text{coda}} = t_c - (t_p - t_0) \quad (6.4)$$

The measured coda length t_{coda} is therefore too short compared to the true coda length t_c and the further the station is away from the earthquake, the smaller becomes t_{coda} for the same event, since t_p increases with distance. To correct for the use of t_{coda} instead of t_c , a compensation must therefore be made for distance and we can expect the scale to look like

$$M_c = a \log(t_{\text{coda}}) + b \text{ dist} + c \quad (6.5)$$

where dist is the hypocentral distance and b is a constant.

- Given the seismograms in Figure 6.1, determine the coda wave magnitude M_c for each station using the relationship

$$M_c = 2.6 * \log t_{\text{coda}} + 0.001 * \text{dist}(\text{km}) - 3.0$$

The distances dist come from exercise 2.

- Calculate the average magnitude.
- How sensitive is the magnitudes to coda lengths ?

Exercise 2

Local magnitude M_l

The local magnitude M_l is defined as

$$M_l = \log(A) + Q(\text{dist})$$

Where A is the maximum amplitude on a Wood-Anderson seismogram (displacement record) in mm and $Q(\text{dist})$ is a distance correction function. The distance correction function for California is given in Table 6.1.

Figure 6.2 shows the displacement seismogram for the local event used in exercise 2. The units of displacement is in nm. The gain of the Wood Anderson seismograph is 2180.

- Read the peak displacement for the stations on Figure 6.2.
- Convert to amplitude on a Wood-Anderson seismogram
- Calculate M_l for all stations
- Compare to the M_c values and evaluate

Exercise 3

Manual determination of M_b and M_s

M_s is calculated from the maximum surface wave amplitude on the vertical trace using the formula

$$M_s = \log(A/T) + 1.66 \log(\Delta) + 3.3$$

where A is the maximum amplitude in micrometers, T is the period in seconds and Δ is the epicentral distance in degrees. Magnitude m_b is calculated as

$$M_b = \log(A/T) + Q(\Delta, h)$$

where A is the maximum amplitude in the P-wave train (first 60 seconds) in nm, Δ is the epicentral distance in degrees and h the focal depth in km. Q is a calibration function found in Figure 6.4.

- Calculate M_s for the event in Figure 5.3 (use results from exercise 5). Assume a shallow depth. The distance can be calculated using the location given on the plot and Figure 7.2
- Calculate M_b for event in Figure 6.3. Assume a depth of 33 km and calculate distance from Figure 7.2.
- Compare to the reported values (can be found in ISC printed bulletin or on ISC web site), try to explain any deviations.

Exercise 4

b-value

Table 6.2 gives a catalog of earthquakes for Western Norway.

- Calculate number of earthquakes in 0.2 magnitude intervals (use coda magnitude), and the accumulative numbers N . Show table.
- Plot $\log N$ vs M and determine the b-value using coda magnitude. Give the relation with both a and b .
- How often will you statistically get a $M \geq 6$ earthquake ?
- Can the detection threshold be estimated ?

Do SEISAN exercise 6

dist	Q(dist)	dist	Q(dist)	dist	Q(dist)
0	1.4	150	3.3	390	4.4
5	1.4	160	3.3	400	4.5
10	1.5	170	3.4	410	4.5
15	1.6	180	3.4	420	4.5
20	1.7	190	3.5	430	4.6
25	1.9	200	3.5	440	4.6
30	2.1	210	3.6	450	4.6
35	2.3	220	3.65	460	4.6
40	2.4	230	3.7	470	4.7
45	2.5	240	3.7	480	4.7
50	2.6	250	3.8	490	4.7
55	2.7	260	3.8	500	4.7
60	2.8	270	3.9	510	4.8
65	2.8	280	3.9	520	4.8
70	2.8	290	4.0	530	4.8
80	2.9	300	4.0	540	4.8
85	2.9	310	4.1	550	4.8
90	3.0	320	4.1	560	4.9
95	3.0	330	4.2	570	4.9
100	3.0	340	4.2	580	4.9
110	3.1	350	4.3	590	4.9
120	3.1	360	4.3	600	4.9
130	3.2	370	4.3		
140	3.2	380	4.4		

Table 6.1 The distance correction table for Southern California. Dist is the epicentral distance in km and Q(dist) the distance correction.

Year	Date	HRMM	Sec	Latitud	Longitud	Depth	Mc	Ml
2003	7 2	1237	56.6	59.246	6.105	9.4	0.9	
2003	710	1303	7.0	59.292	5.616	11.5	1.4	1.2
2003	718	1930	22.1	60.871	5.005	0.0	1.4	1.1
2003	721	1428	57.4	60.952	1.437	15.0	2.5	1.5
2003	722	0335	26.3	60.927	1.627	15.0	2.2	1.4
2003	729	1542	37.7	60.696	3.744	15.0	2.3	2.5
2003	8 2	1912	41.6	60.108	7.204	19.7	1.1	1.0
2003	8 4	1943	52.6	60.692	5.507	0.1	1.0	0.6
2003	811	1349	42.5	60.291	4.894	52.3	0.8	1.5
2003	812	1537	15.1	60.192	2.486	15.0	1.8	1.3
2003	821	0723	1.4	60.086	4.791	0.0	2.2	2.0
2003	821	1159	3.0	60.839	5.029	0.6	1.4	
2003	825	1321	21.6	59.904	6.958	3.9	0.8	
2003	825	1823	18.0	59.281	5.298	20.0	1.3	1.1
2003	827	1621	32.5	59.075	5.812	0.0	1.8	1.8
2003	828	1501	42.5	60.694	5.594	0.0	1.3	
2003	9 3	1334	38.5	59.242	5.706	13.1	1.6	
2003	9 4	1402	21.2	60.863	4.987	15.0	1.2	0.8
2003	9 5	1440	2.0	60.567	4.966	0.0	0.6	0.7
2003	9 5	2117	57.1	59.474	5.675	15.0	2.2	1.9
2003	9 8	1027	15.2	59.646	5.581	0.0	1.5	1.0
2003	9 9	1332	36.6	59.211	6.178	15.6	1.3	1.0
2003	9 9	1803	53.0	60.691	5.378	0.1	1.6	0.8
2003	912	1619	11.9	60.443	4.815	0.6	1.3	1.4
2003	917	0155	30.4	59.604	7.316	15.3	1.7	1.4

2003	917	1435	41.7	59.349	6.077	0.3	1.5	1.1	
2003	918	1806	38.7	59.759	7.061	17.5	1.3		
2003	919	0818	2.0	60.040	4.719	0.0	2.0	2.1	
2003	920	1315	42.4	60.247	5.216	12.4	1.0	1.4	
2003	920	1709	20.5	59.694	7.087	15.5	1.4		
2003	925	1131	45.7	60.466	5.407	0.0	0.8		
2003	928	1654	54.1	60.000	5.861	0.0	1.4	1.2	
2003	928	2025	8.4	60.346	4.738	0.0	1.7	1.5	
2003	929	1552	29.2	60.290	5.128	0.0	1.0		
2003	10	2	1330	35.3	59.153	6.200	15.0	1.3	
2003	10	2	1611	4.4	60.817	4.912	0.1	1.5	1.0
2003	10	9	0108	0.9	60.163	5.314	0.1	1.2	1.3
2003	1014	1355	39.1	60.501	4.919	0.0	1.5	0.9	
2003	1020	0508	10.6	60.417	6.012	13.0	0.9	0.9	
2003	1020	1331	16.0	59.378	6.034	13.8	1.4		
2003	1020	1620	21.0	59.150	7.611	11.3	1.7		
2003	1021	1432	41.3	60.674	5.460	0.0	1.6	0.9	
2003	1022	1400	44.5	60.519	4.944	0.0	1.3		
2003	1023	1419	18.9	60.300	5.295	3.5	1.1		
2003	1028	1803	55.8	60.758	5.242	1.5	1.2		
2003	1031	1605	51.0	60.832	5.013	9.2	1.5		
2003	11	6	0343	50.8	60.747	4.573	0.0	0.9	1.1
2003	11	9	0459	58.9	59.619	7.105	12.6	1.6	0.8
2003	1110	2302	54.9	59.215	5.805	0.0	1.2	1.0	
2003	1113	1301	3.6	60.512	5.349	0.0	0.7	1.4	
2003	1113	1306	21.2	60.677	5.487	0.1	1.4	0.8	
2003	1120	1109	31.8	59.333	5.657	2.3	1.6	1.2	
2003	1121	1310	8.1	60.477	5.350	0.0	0.5	0.8	
2003	1122	1908	58.2	60.218	2.545	15.0	2.6	2.2	
2003	1125	1832	15.8	59.665	2.465	0.0	1.9	1.1	
2003	1127	0317	49.6	59.914	6.215	0.0	0.7	0.6	
2003	1128	1252	0.6	60.276	5.301	6.2	0.2	0.5	
2003	1128	1529	31.3	60.189	5.312	11.4	0.8	0.8	
2003	12	1	1404	6.6	60.713	5.339	0.0	1.6	1.1
2003	12	1	1501	52.0	60.162	5.237	16.1	0.7	0.4
2003	12	4	1449	16.1	60.544	4.959	0.1	1.4	1.3
2003	12	8	2353	9.8	60.323	7.252	3.1	1.8	1.7
2003	12	9	1400	1.2	59.492	4.473	0.1	1.2	1.6
2003	1211	1404	50.0	60.291	5.294	0.0	0.8	1.1	
2003	1211	1454	29.8	60.695	5.568	1.8	1.4	0.8	
2003	1212	0007	13.4	60.489	4.734	21.1	1.1	1.0	
2003	1212	0315	6.7	59.857	6.523	0.0	1.5	1.3	
2003	1212	1516	7.0	60.846	5.102	1.5	1.4	0.6	
2003	1217	1433	40.9	59.315	5.675	0.0	1.5	1.1	
2003	1219	1020	30.0	59.376	6.078	0.1	1.1		
2003	1219	1328	25.4	60.669	5.558	0.1	1.5		
2003	1225	1400	27.7	59.655	6.000	15.0	1.9	1.8	

Table 6.2 Catalog of events

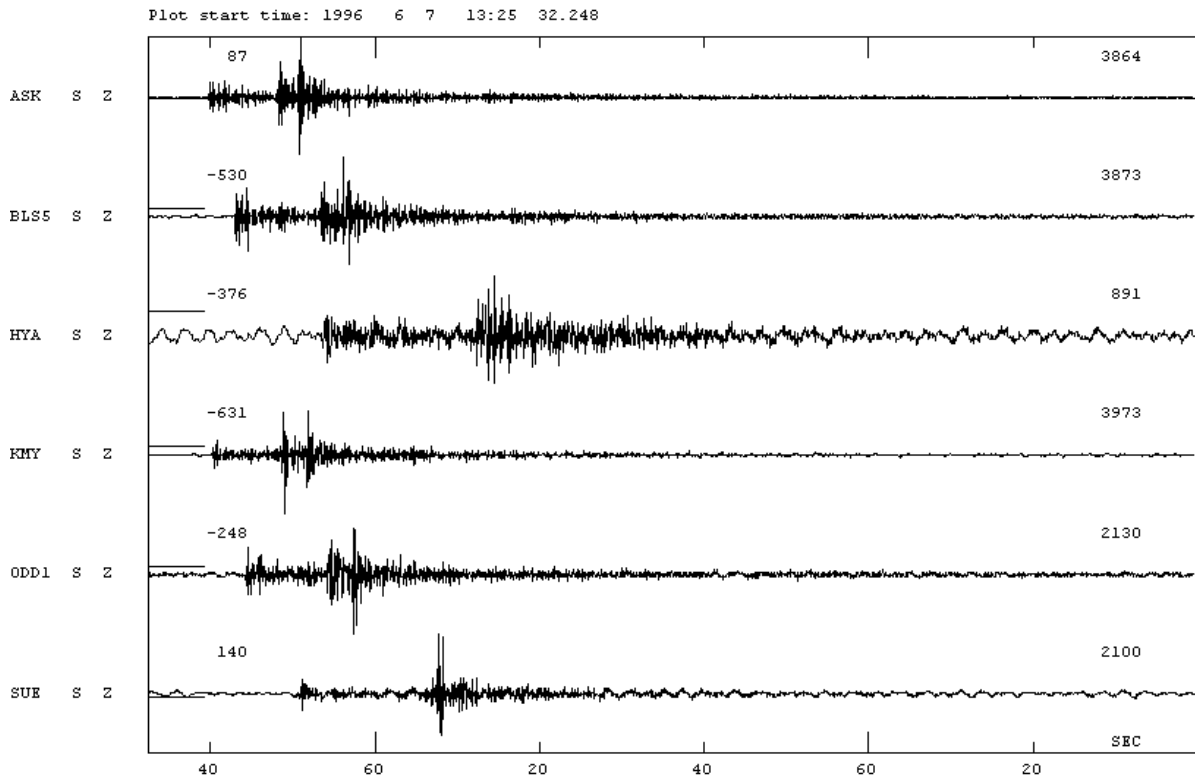


Figure 6.1 Seismogram of a local earthquake, same as in exercise 2

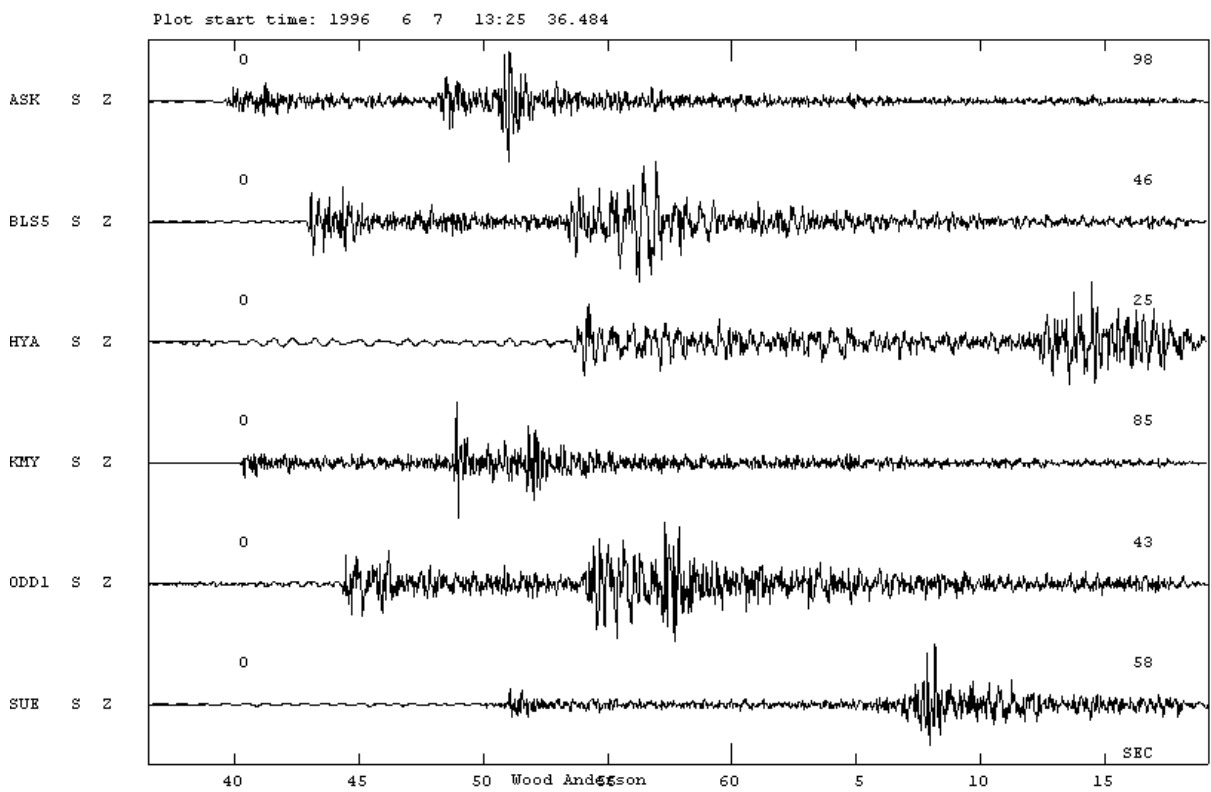


Figure 6.2 Wood Anderson simulated displacement seismogram. The number above traces to the right is maximum amplitude in nm.

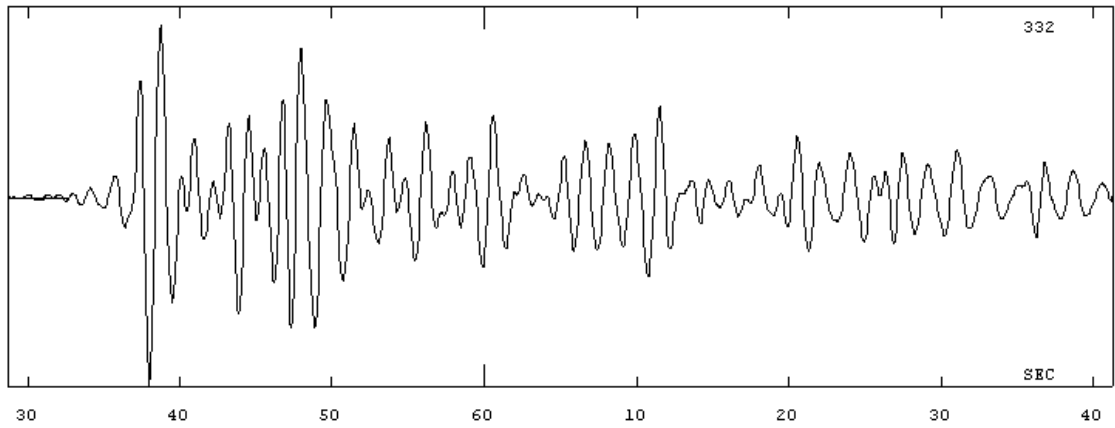


Figure 6.3 P-wave for a distant earthquake recorded in S. Norway. The vertical scale is nm and the maximum amplitude is marked above the trace to the right. The origin is 1996 0603 1955 31.8, the hypocenter has latitude 46.787 N, longitude 153.722 W and depth 33.0 km. The time scale is 2 mm/sec.

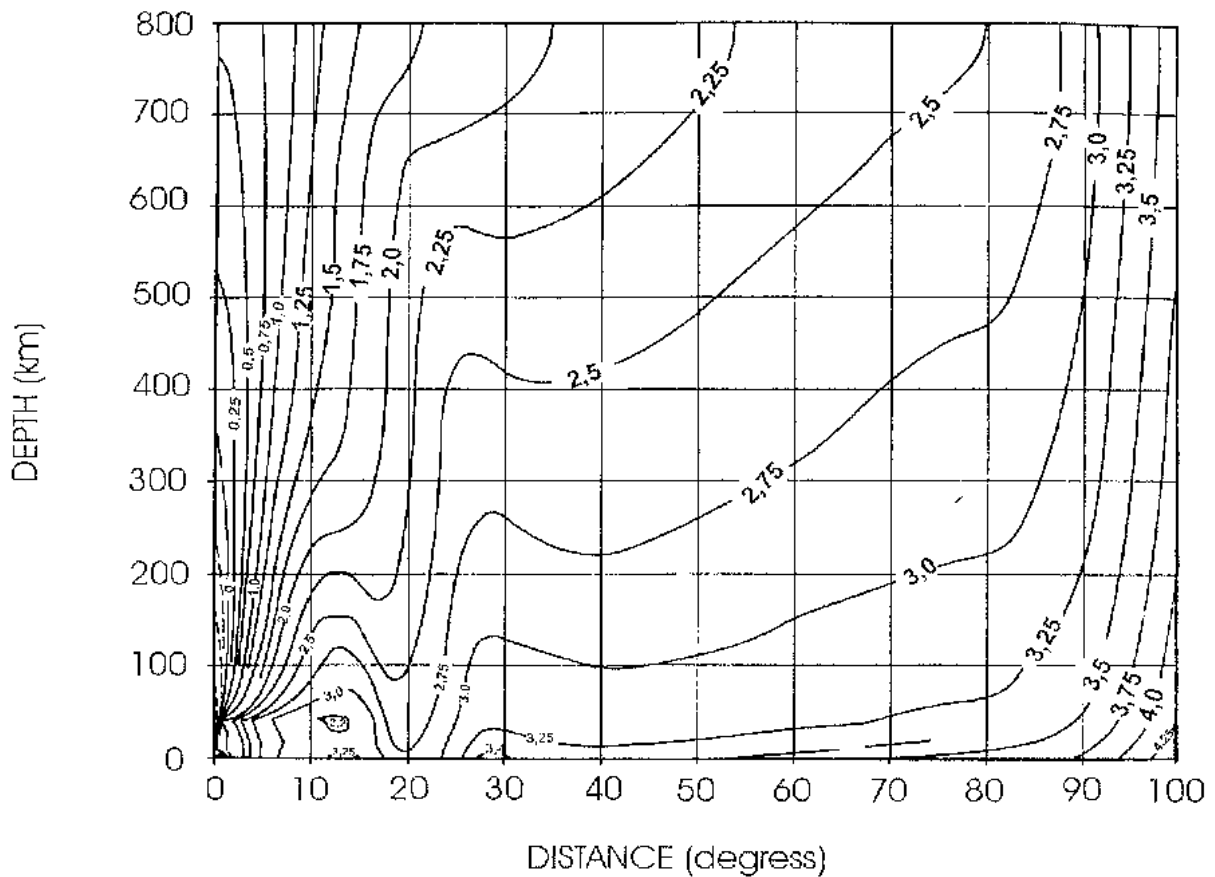


Figure 6.4 Calibration function for mb. It is assumed that the amplitude is measured in nm.

EXERCISE 7

Using a single station or array for azimuth determination

The purpose of this exercise is to locate an event with a single three component station or an array.

Global phases are best recorded on standard LP and SP seismographs sine most of the energy is below 1 Hz. On high gain local networks, a few global events are also located. Global (and local) events can be located with a single 3C station or a seismic array. The 3C location method is described in Appendix 2.

Using a seismic array, the apparent velocity and azimuth to the event can be determined as follows: Considering a plane wave arriving at the 3 stations shown below at times t_0 , t_1 and t_2 , then the following equations can be set up:

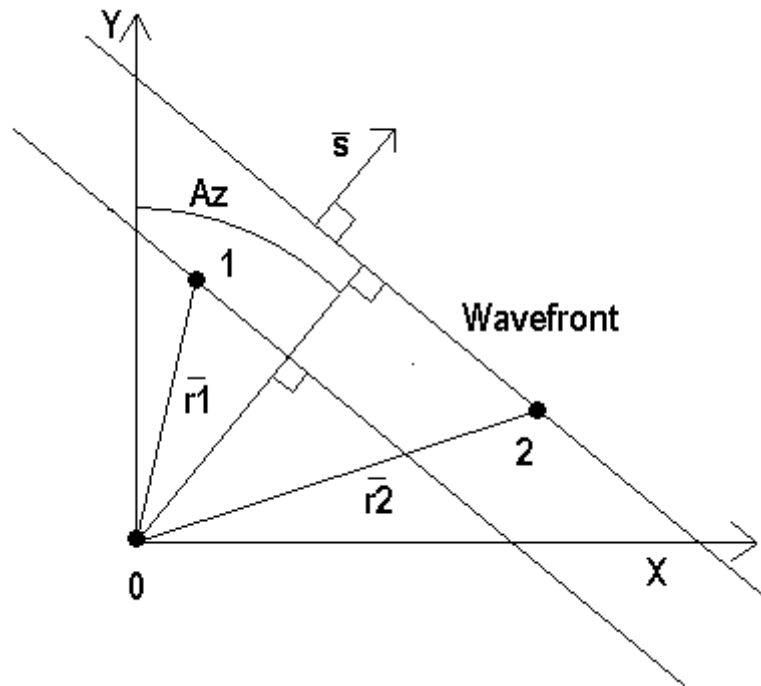


Figure 7.1 A 3 station array. The stations are labeled 0,1,2 and station 0 is placed at the origin of the coordinate system. The vectors from the origin to station 1 and two are labeled \underline{r}_1 and \underline{r}_2 respectively and Az is the azimuth of arrival.

$$\begin{aligned} t_1 - t_0 &= \underline{r}_1 \cdot \underline{p} \\ t_2 - t_0 &= \underline{r}_2 \cdot \underline{p} \end{aligned} \quad (1)$$

where \underline{r}_1 and \underline{r}_2 are the vectors from station 0 to station 1 and 2 respectively and \underline{p} is the slowness vector defined as $\underline{p} = \underline{s}/v$, where \underline{s} is the normal vector to the wave front and v the apparent velocity. Equation 1 can be written out as

$$t_1 - t_0 = r_{1x} \cdot p_x + r_{1y} \cdot p_y \quad (2)$$

$$t_2 - t_0 = r_{2x} * p_x + r_{2y} * p_y$$

where p_x and p_y are the x and y components of the p-vector and corresponding for r_{1x} etc. Thus knowing the arrival times at the 3 stations, p_x and p_y can be determined (2 equations with 2 unknowns). From p_x and p_y , v and azimuth can be determined:

$$\text{tg}(Az) = p_x/p_y$$

$$v = \text{sqrt}(1/(p_x * p_x + p_y * p_y))$$

Note that the azimuth above is away from the event, while the azimuth needed to find the epicenter is from the station to the event and 180 deg must be added. Since it is possible to get the epicentral distance from the apparent velocity, a location can be made.

Exercise 1

Azimuth and velocity from a three station array

An array has the following station location (coordinates in km):

Station 0 (0,0)

Station 1 (100,0)

Station 2 (0,200)

A P-wave is arriving at times $t_0=0$ sec, $t_1=7$ sec and $t_2=13$ sec.

-Calculate the azimuth and apparent velocity.

-From the Bullen table, get the distance to the earthquake. Remember that the Bullen table gives the apparent velocity in sec/degree, so the easiest is to convert from km/sec to sec/deg before looking up in the table (1 degree = 111.1 km). Assume a depth of 33 km.

-Use Figure 7.2 to get an approximate location assuming the array is located in Bergen.

-Describe how you would find p_x and p_y if you had e.g. 10 stations.

Exercise 2

Azimuth from a three component station

-Using the 3C seismogram in Figure 7.3, calculate the az of approach.

-Read the S-P time on Figure 7.4 and find the distance from Bullen or a travel time curve assuming a depth of 33 km..

-Locate the event using Figure 7.2 and give latitude, longitude and origin time..

-Compare to the real solution (found e.g. in ISC bulletin).

Exercise 3

Azimuth determination by computer

-Do SEISAN exercise 12, '3 component analysis for azimuth determination'. Describe results and uncertainties in determination.

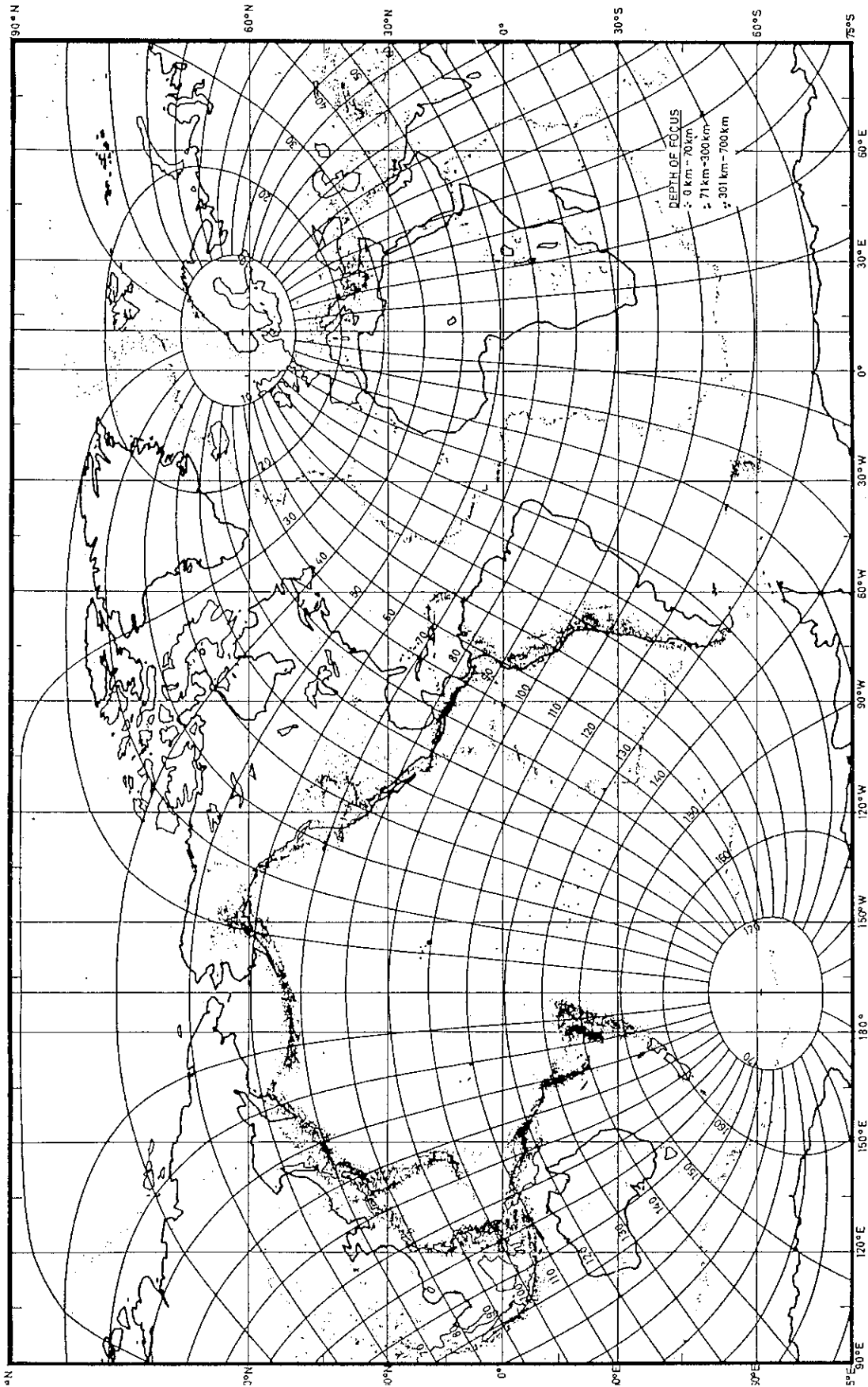


Figure 7.2 World map

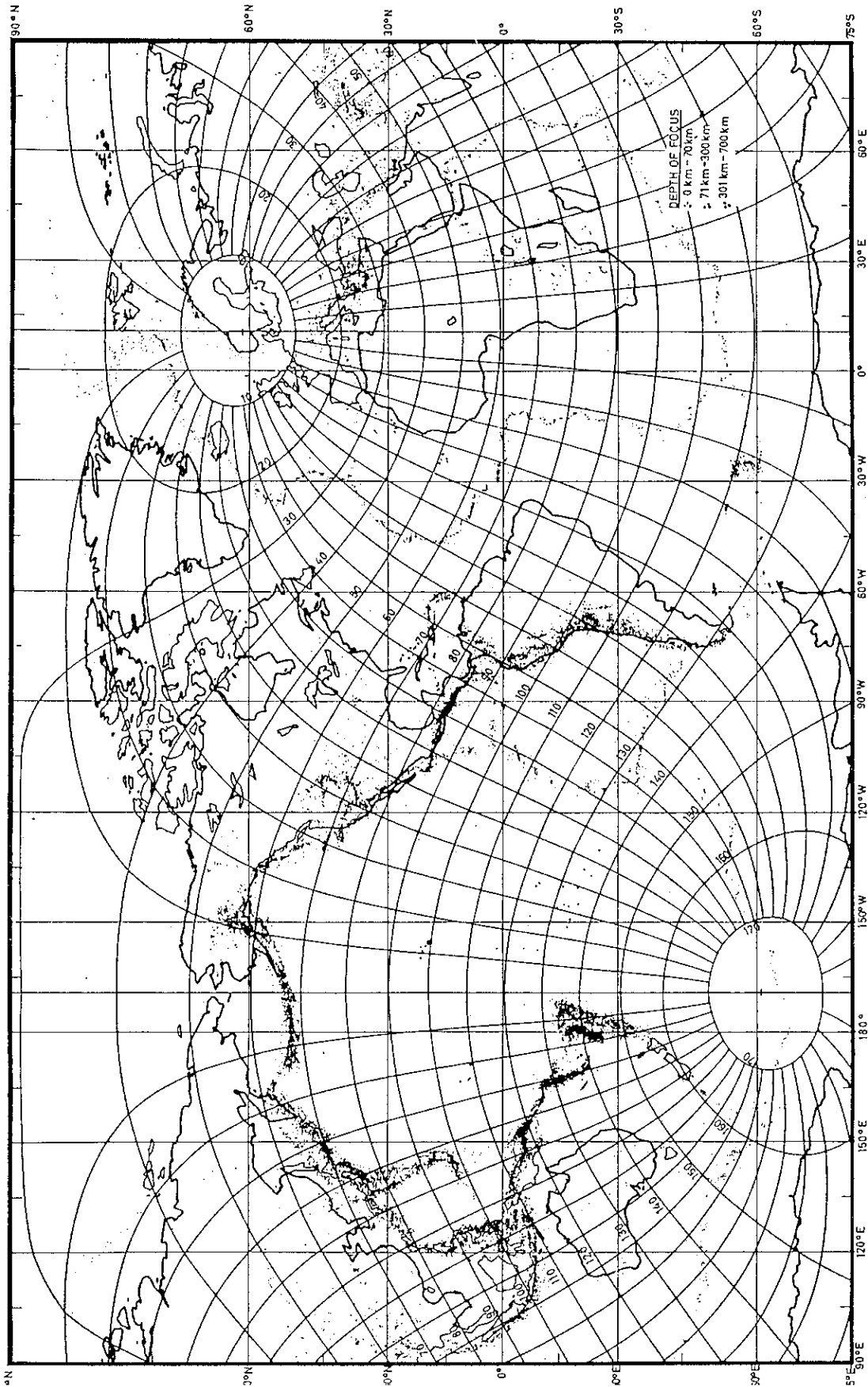


Figure 7.2 World map, extra copy

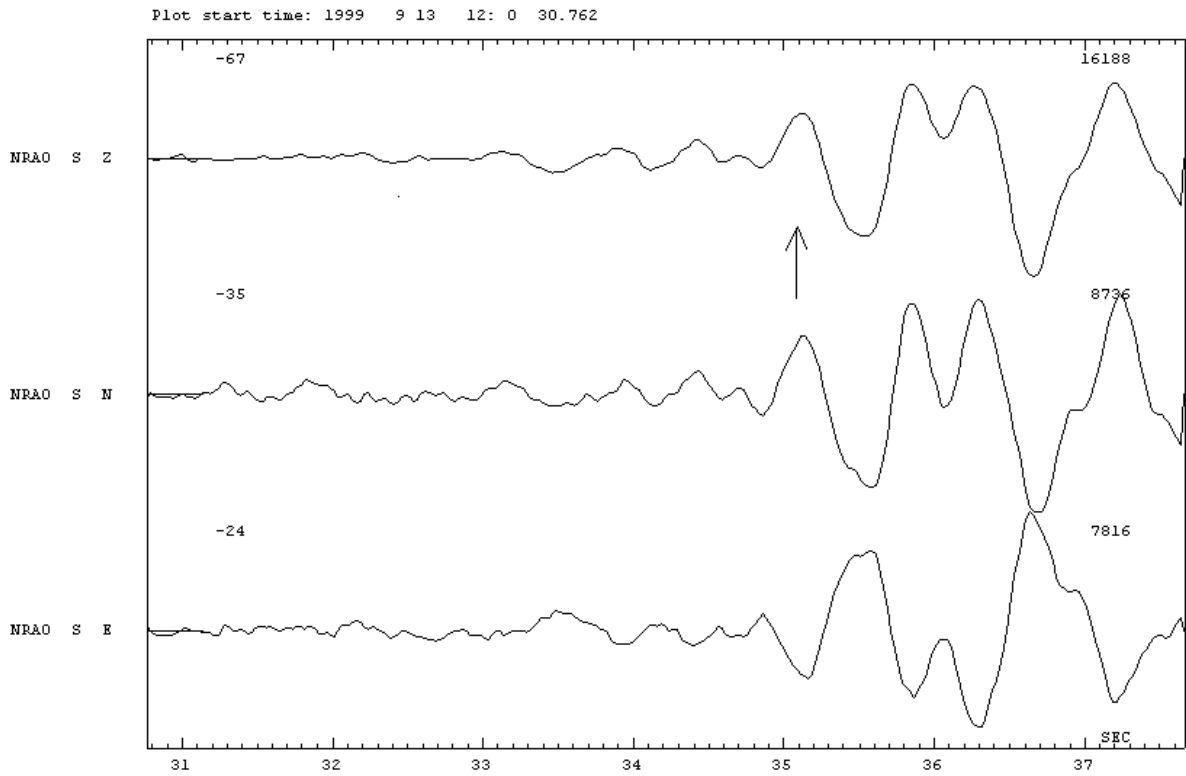


Figure 7.3 A three component recording, only the first P is shown. the time scale is 20 mm/sec.

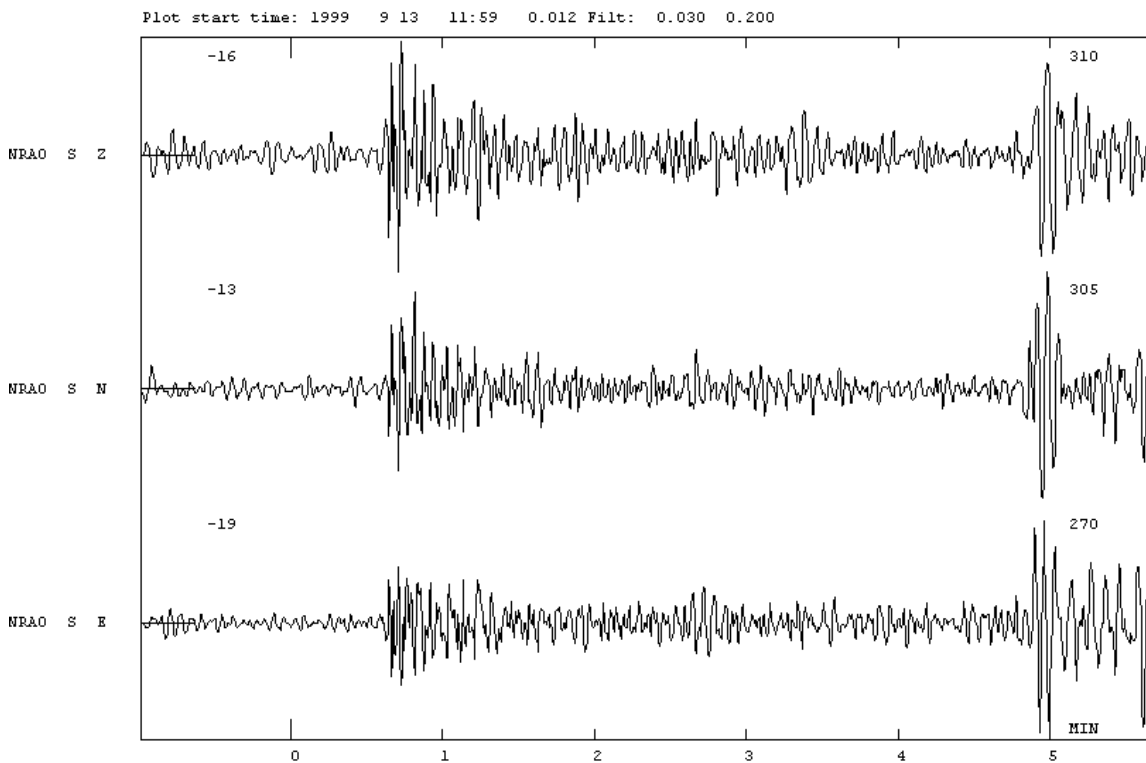


Figure 7.4 The complete cording of the event in Figure 7.2. A filter is used to enhance the low frequencies. The time scale is 20 mm/min.

EXERCISE 8

FAULT PLANE SOLUTION

In this exercise, fault plane solutions will be determined both manually and with SEISAN for both local and global events. Background material is found in Appendix 2 including a stereo net.

Exercise 1

Manual fault plane solution for a local event

Do exercise 3.2 in Appendix 2, task 1-7, 9, 12-14.

Exercise 2

Manual fault plane solution from a distant event

Table 8.1 is an earthquake bulletin for ISC. Only stations which reported polarity (p or d) are given.

Get angle of incidence from distances using Table 8.2. For stations at distances less than 20 deg., calculate the angle assuming all phases to be Pn and the Moho velocity is 8 km/s and the velocity above Moho is 7 km/s. Then plot on a stereo net and find the fault plane solution. Put the T and P-axis on the solution. Measure the angles of the 2 fault plane solutions and the T and P-axis. From the angles of the P and T axis, calculate strike, dip and rake using the Focmec program type focmec a. Compare to the solution given by ISC by plotting the solution on the same figure.

-Which kind of fault do the solution represent.

Exercise 3

Fault plane solution done by computer

Do SEISAN exercise 7

Err	rms	OT_error	Smajor	Sminor	Az	Err	mdist	Mdist	Err	Err
Err	Quality									
2000/01/06 10:42:22.8			58.0180	-141.0300		1.0 f		5 351	MS 5.7	mb 5.1
mb 5.5	BER		3544558							
	1.60	+- 4.86	94.3	581.3	-1					
2000/01/06 10:42:25.0			58.0000	-136.9000		5.0		58	Ms 6.5	6.1
mB 5.9	BJI		3017104							
	1.70									
2000/01/06 10:42:25.0	f		58.0400	-136.8700	f	1.0 f		371 31	5.9 73	Me 6.2
Mw 6.1	NEIC		3050653							

1.29 150.19

fe

```
(#FAULT_PLANE Typ Strike Dip Rake NP NS Plane Author )
(# BB 345.00 78.00 -178.00 NEIC )
(+ BB 255.00 88.00 -12.00 NEIC )
(#PRINAX sc T_val T_azim T_pl B_val B_azim B_pl P_val P_azim P_pl Author )
(# 300.00 7.00 0.00 0.00 209.00 10.00 NEIC )
(#MOMTENS sc MO fCLVD MRR MTT MPP MRT MTP MPR NST1 NST2 Author )
(# eMO eCLVD eRR eTT ePP eRT eTP ePR NCO1 NCO2 duration )
(# 18 1.500 0.170 -0.950 0.780 0.120 1.180 -0.080 43 NEIC )
(# )
(#FAULT_PLANE Typ Strike Dip Rake NP NS Plane Author )
(# BDC 252.00 86.00 -3.00 NEIC )
(+ BDC 342.00 87.00 -176.00 NEIC )
(#PRINAX sc T_val T_azim T_pl B_val B_azim B_pl P_val P_azim P_pl Author )
(# 18 1.380 117.00 1.00 0.180 16.00 85.00 -1.560 207.00 5.00 NEIC )
```

(Depth from synthetics of broadband displacement seismograms. Energy computed from BB mechanism.)

(After preliminary solution from PGC.)

(Felt strongly at Elfin Cove, Gustavus, Haines, Hoonah, Juneau and Sitka. Also felt at Petersburg, Skagway and Yakutat. Felt as far a)

(Whitehorse, Yukon Territory)

(#PARAM BROADBAND_DEPTH=12.0 SEISMIC_ENERGY=4.8E13+0.7E13)

2000/01/06 10:42:25.8			58.0680	-136.8081		1.0 f	9	6	ML 6.1	4
PGC			3443410							
	0.37		3.3	1.8	-1				+-0.2	

ke

(Coast of southeastern Alaska.)

2000/01/06 10:42:27.0			58.2071	-136.7483		0.0 f	21	17 155	ML 4.8	3 MS 5.8	11
mb 4.9	11	EIDC	3009581								
	0.73	+- 0.77	19.1	12.0	33			3.55 147.87	+-0.4	+-0.1	
	+-0.1	uk									

2000/01/06 10:42:29.4			58.2074	-136.7458		33.0	28	28	Mb 5.5	31 Ms 5.9	6
LDG			3029562								
	+- 0.42		21.4	14.7	11	+- 0.0	61.97	98.38	+-0.2	+-0.1	

ke

2000/01/06 10:42:29.8			58.1230	-136.9790		33.0	109		MS 5.8	34 mb 5.7	31
MOS			3023607								
	+- 1.07		11.5	4.1	21						

2000/01/06 10:42:32.8			58.2700	-136.8000					Mw 6.1		
HRVD			3050654								
	+- 0.10		0.0	0.0	-1						

se

```
(#CENTROID)
(#MOMTENS sc MO fCLVD MRR MTT MPP MRT MTP MPR NST1 NST2 Author )
(# eMO eCLVD eRR eTT ePP eRT eTP ePR NCO1 NCO2 duration )
```

```

(#      18 1.600      -0.120 -0.840  0.960  0.800  1.030 -0.160  60  55 HRVD      )
(#      0.010  0.010  0.010  0.040  0.010  0.040  151 105      5.40 )
(#FAULT_PLANE Typ Strike  Dip  Rake  NP  NS Plane Author  )
(#      BDC 343.00 65.00 -166.00      HRVD      )
(+      BDC 247.00 77.00 -25.00      HRVD      )
(#PRINAX sc  T_val T_azim T_pl  B_val B_azim B_pl  P_val P_azim P_pl Author  )
(#      18 1.460 297.00  8.00  0.260 42.00 62.00 -1.720 203.00 27.00 HRVD      )
(Data Used: GSN.)
(#PARAM pP_DEPTH=15)
2000/01/06 10:42:44.5      60.7430 -140.4150      1.0 f      5      mb 4.6
NAO      3544559

2000/01/06 10:42:55.1      61.8000 -134.1000      10.0      27  27 358  mb 5.9 27
ZUR      3529774
0.26      66.75  68.36  +-0.3
uk
2000/01/06 10:42:25.3      58.1340 -136.9340      1.0 f  476 515 117  MS 5.9      mb 5.5
ISC      3630399
1.14 +- 0.13      2.6  2.3  90      1.38 157.06
m i
(#PARAM pP_DEPTH=8.7+1.64 )

```

SOUTHEASTERN ALASKA

ta	Dist	EvAz	Phase	Date	Time	TRes	Azim	AzRes	Slow
HYT	2.71	354.1	d PN	2000/01/06	10:43:11.1	0.3			
WHY	2.74	21.6	d PN	2000/01/06	10:43:11.5	0.3			
BNAB	5.85	140.0	c PN	2000/01/06	10:43:51.6	-3.6			
DAWY	6.07	349.7	d PN	2000/01/06	10:43:58.0	-0.4			
BMBC	8.33	98.2	d P	2000/01/06	10:44:27.2	-2.9			
DOWB	12.49	114.1	c P	2000/01/06	10:45:25.7	-1.2			
PNT	13.49	123.4	c P	2000/01/06	10:45:40.6	0.3			
ULM	24.94	90.5	d P	2000/01/06	10:47:50.4	-0.6			
KLR	50.79	302.2	di P	2000/01/06	10:51:28.7	0.0			
BOD	51.35	319.6	ci P	2000/01/06	10:51:32.6	-0.2			
IRK	59.21	321.2	ce P	2000/01/06	10:52:29.0	-0.8			
SNY	60.14	301.8	d P	2000/01/06	10:52:34.2	-2.2			
MOY	60.80	322.8	ce P	2000/01/06	10:52:41.3	0.6			
UKR	66.06	332.6	ci P	2000/01/06	10:53:14.5	-0.7			
MOS	66.40	3.4	ci P	2000/01/06	10:53:13.9	-3.4			
CLL	68.18	19.8	c P	2000/01/06	10:53:28.8	0.1			
SLE	70.67	23.9	de P	2000/01/06	10:53:43.5	-0.5			6.4
BOURR	70.75	24.9	de P	2000/01/06	10:53:44.7	0.2			6.4
ZLA	70.92	24.1	de P	2000/01/06	10:53:45.4	-0.1			6.4
KAMOR	71.33	23.4	de P	2000/01/06	10:53:48.6	0.6			6.4
APL	71.39	24.4	de P	2000/01/06	10:53:48.7	0.3			6.4
BNALP	71.50	24.3	de P	2000/01/06	10:53:49.9	0.8			6.4
HASLI	71.55	24.5	de P	2000/01/06	10:53:50.0	0.6			6.4
LLS	71.65	23.9	de P	2000/01/06	10:53:50.3	0.4			6.4
LLS	71.65	23.9	de P	2000/01/06	10:53:50.6				6.4
AIGLE	71.68	25.5	de P	2000/01/06	10:53:50.2	0.1			6.4
DAVON	71.83	23.4	de P	2000/01/06	10:53:52.1	1.1			6.4
FUSIO	71.95	24.3	de P	2000/01/06	10:53:52.7	1.0			6.4
BOG	72.00	111.1	ci P	2000/01/06	10:53:57.5	4.9			
DIX	72.03	25.2	de P	2000/01/06	10:53:52.8	0.6			6.4
DIX	72.03	25.2	de P	2000/01/06	10:53:53.2				6.4
OSS	72.05	23.2	de P	2000/01/06	10:53:52.9	0.6			6.4
VDL	72.09	23.7	de P	2000/01/06	10:53:53.8	1.2			6.4
MMK	72.18	24.9	de P	2000/01/06	10:53:54.4	1.3			6.4

MCGN	72.27	24.9	c	P	2000/01/06 10:53:55.3	1.6	
BERNI	72.28	23.3	de	P	2000/01/06 10:53:54.9	1.2	6.4
WHN	73.63	301.6	d	P	2000/01/06 10:54:01.6	-0.2	
ASS	76.02	22.5	c	P	2000/01/06 10:54:15.9	0.6	
MNS	76.69	22.6	c	P	2000/01/06 10:54:19.3	0.2	
NURP	85.83	332.6	ci	P	2000/01/06 10:55:04.2	-3.1	
SHL	87.23	317.1	ci	P	2000/01/06 10:55:14.0	-0.3	

Table 8.2 ISC bulletin, extract.

TABLE 8.2

EXTENDED DISTANCES AND ANGLES OF INCIDENCE
 TABLE FOR THE EXTENDED DISTANCES AND THE ANGLES OF INCIDENCE OF P WAVES

AT SOURCE
 AT SURFACE 889

DISTANCE	DEPTH = 0 KM.				DEPTH = 15 KM.				DEPTH = 40 KM.			
	EX.D.	I_r	I_h	I_o	EX.D.	I_r	I_h	I_o	EX.D.	I_r	I_h	I_o
20.0	1.302	37.53	37.53	37.53	1.067	43.14	43.15	37.34	0.755	52.93	54.21	36.93
20.5	1.346	36.62	36.62	36.62	1.109	42.05	42.04	36.43	0.798	51.43	52.60	36.05
21.0	1.390	35.73	35.73	35.73	1.151	40.99	40.97	35.55	0.838	50.03	51.09	35.20
21.5	1.436	34.86	34.86	34.86	1.194	39.95	39.93	34.70	0.877	48.74	49.66	34.38
22.0	1.482	34.02	34.02	34.02	1.237	38.95	38.94	33.87	0.915	47.55	48.31	33.59
22.5	1.527	33.22	33.22	33.22	1.280	38.01	38.00	33.09	0.951	46.44	47.07	32.85
23.0	1.569	32.50	32.50	32.50	1.319	37.16	37.16	32.39	0.986	45.41	45.96	32.17
23.5	1.609	31.85	31.85	31.85	1.356	36.40	36.40	31.75	1.019	44.46	44.97	31.57
24.0	1.647	31.27	31.27	31.27	1.391	35.72	35.73	31.19	1.050	43.60	44.09	31.02
24.5	1.680	30.76	30.76	30.76	1.422	35.12	35.13	30.68	1.077	42.88	43.32	30.54
25.0	1.711	30.31	30.31	30.31	1.449	34.61	34.61	30.24	1.100	42.27	42.65	30.12
25.5	1.738	29.92	29.92	29.92	1.474	34.16	34.16	29.86	1.120	41.77	42.08	29.76
26.0	1.761	29.59	29.59	29.59	1.495	33.79	33.78	29.54	1.136	41.36	41.60	29.46
26.5	1.781	29.32	29.32	29.32	1.512	33.48	33.47	29.28	1.149	41.04	41.22	29.21
27.0	1.796	29.11	29.11	29.11	1.526	33.24	33.23	29.08	1.158	40.81	40.92	29.02
27.5	1.808	28.95	28.95	28.95	1.536	33.06	33.06	28.93	1.164	40.65	40.71	28.89
28.0	1.815	28.85	28.85	28.85	1.543	32.95	32.95	28.84	1.168	40.57	40.59	28.81
28.5	1.820	28.79	28.79	28.79	1.547	32.88	32.88	28.78	1.170	40.51	40.51	28.76
29.0	1.823	28.74	28.74	28.74	1.550	32.82	32.82	28.73	1.173	40.44	40.44	28.72
29.5	1.826	28.71	28.71	28.71	1.553	32.78	32.78	28.69	1.177	40.35	40.39	28.69
30.0	1.829	28.67	28.67	28.67	1.556	32.73	32.73	28.65	1.181	40.25	40.43	28.64
30.5	1.834	28.60	28.60	28.60	1.561	32.65	32.65	28.58	1.186	40.13	40.21	28.57
31.0	1.842	28.50	28.50	28.50	1.567	32.54	32.54	28.49	1.192	40.00	40.06	28.47
31.5	1.849	28.40	28.40	28.40	1.574	32.43	32.43	28.40	1.198	39.86	39.90	28.37
32.0	1.856	28.31	28.31	28.31	1.580	32.33	32.33	28.31	1.204	39.72	39.76	28.28
32.5	1.862	28.23	28.23	28.23	1.586	32.23	32.23	28.22	1.210	39.58	39.63	28.19
33.0	1.869	28.15	28.15	28.15	1.593	32.13	32.13	28.14	1.216	39.44	39.50	28.11
33.5	1.875	28.07	28.07	28.07	1.599	32.02	32.02	28.05	1.222	39.30	39.37	28.02
34.0	1.883	27.97	27.97	27.97	1.606	31.91	31.91	27.96	1.228	39.16	39.22	27.93
34.5	1.891	27.88	27.88	27.88	1.613	31.80	31.80	27.86	1.235	39.01	39.07	27.83
35.0	1.899	27.77	27.77	27.77	1.620	31.68	31.68	27.76	1.241	38.85	38.92	27.73
35.5	1.907	27.67	27.67	27.67	1.628	31.56	31.56	27.66	1.249	38.69	38.75	27.62
36.0	1.916	27.56	27.56	27.56	1.636	31.43	31.43	27.54	1.256	38.52	38.58	27.51
36.5	1.926	27.44	27.44	27.44	1.645	31.30	31.30	27.43	1.265	38.34	38.40	27.40
37.0	1.936	27.32	27.32	27.32	1.654	31.16	31.16	27.31	1.273	38.15	38.22	27.28
37.5	1.946	27.20	27.20	27.20	1.663	31.02	31.02	27.19	1.282	37.96	38.04	27.16
38.0	1.956	27.08	27.08	27.08	1.672	30.88	30.88	27.07	1.290	37.78	37.85	27.04
38.5	1.966	26.96	26.96	26.96	1.682	30.74	30.74	26.95	1.299	37.60	37.67	26.92
39.0	1.976	26.85	26.85	26.85	1.691	30.60	30.60	26.83	1.307	37.42	37.49	26.80
39.5	1.985	26.73	26.73	26.73	1.700	30.46	30.46	26.72	1.315	37.28	37.32	26.68

DISTANCE	DEPTH = 0 KM.				DEPTH = 15 KM.				DEPTH = 40 KM.			
	EX.D.	I_r	I_h	I_o	EX.D.	I_r	I_h	I_o	EX.D.	I_r	I_h	I_o
40.0	1.995	26.62	26.62	26.62	1.710	30.32	30.32	26.60	1.324	37.07	37.14	26.57
40.5	2.005	26.50	26.50	26.50	1.719	30.19	30.19	26.48	1.332	36.90	36.97	26.45
41.0	2.016	26.39	26.39	26.39	1.728	30.05	30.05	26.36	1.341	36.72	36.79	26.33
41.5	2.026	26.27	26.27	26.27	1.738	29.91	29.91	26.25	1.349	36.55	36.61	26.22
42.0	2.036	26.15	26.15	26.15	1.748	29.78	29.78	26.13	1.358	36.37	36.44	26.10
42.5	2.047	26.03	26.03	26.03	1.757	29.64	29.64	26.01	1.367	36.19	36.26	25.98
43.0	2.058	25.91	25.91	25.91	1.767	29.50	29.50	25.90	1.376	36.01	36.08	25.86
43.5	2.069	25.79	25.79	25.79	1.777	29.37	29.37	25.78	1.385	35.83	35.90	25.74
44.0	2.081	25.67	25.67	25.67	1.788	29.22	29.22	25.66	1.394	35.65	35.72	25.62
44.5	2.092	25.54	25.54	25.54	1.798	29.08	29.08	25.53	1.404	35.46	35.53	25.50
45.0	2.104	25.42	25.42	25.42	1.809	28.94	28.94	25.41	1.414	35.27	35.35	25.37
45.5	2.116	25.29	25.29	25.29	1.820	28.79	28.79	25.28	1.424	35.08	35.16	25.25
46.0	2.129	25.16	25.16	25.16	1.831	28.64	28.64	25.15	1.434	34.89	34.97	25.12
46.5	2.141	25.03	25.03	25.03	1.843	28.49	28.49	25.02	1.445	34.69	34.77	24.99
47.0	2.154	24.91	24.91	24.91	1.854	28.34	28.34	24.89	1.455	34.50	34.58	24.86
47.5	2.166	24.78	24.78	24.78	1.866	28.19	28.19	24.76	1.465	34.31	34.39	24.74
48.0	2.179	24.65	24.65	24.65	1.878	28.04	28.04	24.64	1.476	34.12	34.20	24.61
48.5	2.192	24.52	24.52	24.52	1.889	27.89	27.89	24.51	1.486	33.93	34.01	24.48
49.0	2.205	24.40	24.40	24.40	1.901	27.74	27.74	24.38	1.497	33.75	33.82	24.35
49.5	2.217	24.27	24.27	24.27	1.913	27.60	27.60	24.25	1.507	33.57	33.64	24.23
50.0	2.230	24.15	24.15	24.15	1.925	27.45	27.45	24.13	1.517	33.39	33.45	24.10
50.5	2.243	24.03	24.03	24.03	1.937	27.31	27.31	24.01	1.528	33.21	33.27	23.98
51.0	2.256	23.90	23.90	23.90	1.948	27.17	27.17	23.89	1.538	33.03	33.09	23.86
51.5	2.269	23.78	23.78	23.78	1.960	27.03	27.03	23.77	1.548	32.85	32.92	23.74
52.0	2.282	23.66	23.66	23.66	1.972	26.89	26.89	23.65	1.559	32.66	32.74	23.62
52.5	2.295	23.54	23.54	23.54	1.984	26.75	26.75	23.53	1.569	32.51	32.57	23.50
53.0	2.309	23.42	23.42	23.42	1.996	26.61	26.61	23.41	1.580	32.33	32.40	23.38
53.5	2.322	23.30	23.30	23.30	2.008	26.48	26.48	23.29	1.591	32.16	32.22	23.26
54.0	2.336	23.18	23.18	23.18	2.020	26.34	26.34	23.17	1.601	31.98	32.04	23.14
54.5	2.349	23.06	23.06	23.06	2.033	26.20	26.20	23.05	1.612	31.81	31.87	23.02
55.0	2.363	22.94	22.94	22.94	2.045	26.06	26.06	22.92	1.623	31.64	31.69	22.90
55.5	2.377	22.82	22.82	22.82	2.058	25.91	25.91	22.80	1.634	31.46	31.51	22.78
56.0	2.391	22.70	22.70	22.70	2.071	25.77	25.77	22.68	1.646	31.29	31.33	22.66
56.5	2.405	22.57	22.57	22.57	2.084	25.63	25.63	22.56	1.657	31.11	31.16	22.53
57.0	2.420	22.45	22.45	22.45	2.097	25.49	25.49	22.44	1.668	30.94	30.98	22.41
57.5	2.435	22.33	22.33	22.33	2.111	25.35	25.35	22.31	1.680	30.76	30.80	22.29
58.0	2.450	22.21	22.21	22.21	2.124	25.21	25.21	22.19	1.692	30.59	30.62	22.16
58.5	2.465	22.08	22.08	22.08	2.138	25.07	25.07	22.07	1.703	30.41	30.44	22.04
59.0	2.479	21.97	21.97	21.97	2.151	24.93	24.93	21.95	1.715	30.25	30.27	21.93
59.5	2.494	21.85	21.85	21.85	2.164	24.80	24.80	21.84	1.727	30.08	30.10	21.81

TABLE—Continued

DISTANCE	DEPTH = 0 KM.				DEPTH = 15 KM.				DEPTH = 40 KM.			
	EX.D.	I _r	I _h	I _o	EX.D.	I _r	I _h	I _o	EX.D.	I _r	I _h	I _o
60.0	2.508	21.74	21.74	21.74	2.177	24.67	24.67	21.72	1.738	29.92	29.94	21.70
60.5	2.522	21.63	21.63	21.63	2.190	24.54	24.54	21.61	1.749	29.76	29.78	21.59
61.0	2.536	21.52	21.52	21.52	2.203	24.42	24.42	21.51	1.761	29.60	29.62	21.48
61.5	2.551	21.41	21.41	21.41	2.215	24.29	24.29	21.40	1.772	29.44	29.47	21.37
62.0	2.565	21.30	21.30	21.30	2.228	24.17	24.17	21.29	1.783	29.28	29.31	21.26
62.5	2.579	21.19	21.19	21.19	2.241	24.04	24.04	21.18	1.795	29.13	29.16	21.15
63.0	2.594	21.08	21.08	21.08	2.255	23.92	23.92	21.07	1.806	28.97	29.01	21.05
63.5	2.609	20.97	20.97	20.97	2.268	23.79	23.79	20.96	1.818	28.82	28.86	20.95
64.0	2.624	20.86	20.86	20.86	2.282	23.67	23.67	20.85	1.829	28.66	28.71	20.84
64.5	2.639	20.75	20.75	20.75	2.296	23.54	23.54	20.74	1.841	28.51	28.55	20.73
65.0	2.654	20.65	20.65	20.65	2.309	23.41	23.41	20.63	1.853	28.35	28.39	20.62
65.5	2.669	20.54	20.54	20.54	2.323	23.29	23.29	20.52	1.865	28.19	28.21	20.50
66.0	2.685	20.43	20.43	20.43	2.337	23.16	23.16	20.42	1.878	28.04	28.05	20.39
66.5	2.701	20.32	20.32	20.32	2.351	23.04	23.04	20.31	1.891	27.88	27.89	20.28
67.0	2.717	20.21	20.21	20.21	2.366	22.91	22.91	20.20	1.903	27.72	27.74	20.17
67.5	2.733	20.10	20.10	20.10	2.380	22.79	22.79	20.09	1.917	27.55	27.59	20.06
68.0	2.750	19.98	19.98	19.98	2.396	22.66	22.66	19.97	1.930	27.39	27.43	19.95
68.5	2.768	19.87	19.87	19.87	2.412	22.52	22.52	19.86	1.944	27.22	27.26	19.83
69.0	2.785	19.75	19.75	19.75	2.428	22.38	22.38	19.73	1.959	27.04	27.09	19.71
69.5	2.803	19.62	19.62	19.62	2.446	22.24	22.24	19.61	1.974	26.87	26.91	19.59
70.0	2.825	19.50	19.50	19.50	2.464	22.09	22.09	19.48	1.989	26.69	26.72	19.46
70.5	2.846	19.36	19.36	19.36	2.483	21.94	21.94	19.35	2.005	26.50	26.53	19.32
71.0	2.869	19.22	19.22	19.22	2.503	21.78	21.78	19.21	2.024	26.30	26.33	19.18
71.5	2.892	19.07	19.07	19.07	2.524	21.61	21.61	19.06	2.042	26.09	26.13	19.04
72.0	2.915	18.93	18.93	18.93	2.545	21.45	21.45	18.92	2.060	25.89	25.94	18.90
72.5	2.937	18.80	18.80	18.80	2.567	21.29	21.29	18.79	2.078	25.70	25.74	18.77
73.0	2.959	18.68	18.68	18.68	2.586	21.14	21.14	18.65	2.095	25.51	25.55	18.63
73.5	2.979	18.55	18.55	18.55	2.605	21.00	21.00	18.53	2.111	25.34	25.37	18.51
74.0	3.000	18.44	18.44	18.44	2.622	20.88	20.88	18.42	2.127	25.18	25.21	18.39
74.5	3.020	18.32	18.32	18.32	2.639	20.76	20.76	18.32	2.142	25.03	25.06	18.29
75.0	3.041	18.20	18.20	18.20	2.656	20.63	20.63	18.21	2.157	24.87	24.91	18.18
75.5	3.062	18.09	18.09	18.09	2.675	20.49	20.49	18.09	2.173	24.71	24.75	18.06
76.0	3.084	17.97	17.97	17.97	2.696	20.35	20.35	17.96	2.190	24.55	24.58	17.95
76.5	3.106	17.85	17.85	17.85	2.717	20.20	20.20	17.84	2.207	24.37	24.41	17.82
77.0	3.129	17.72	17.72	17.72	2.739	20.05	20.05	17.70	2.226	24.19	24.23	17.70
77.5	3.153	17.60	17.60	17.60	2.762	19.90	19.90	17.57	2.245	24.01	24.05	17.57
78.0	3.178	17.47	17.47	17.47	2.784	19.76	19.76	17.44	2.265	23.82	23.86	17.44
78.5	3.203	17.34	17.34	17.34	2.806	19.62	19.62	17.32	2.285	23.64	23.68	17.31
79.0	3.229	17.21	17.21	17.21	2.827	19.48	19.48	17.20	2.305	23.46	23.49	17.18
79.5	3.254	17.08	17.08	17.08	2.849	19.34	19.34	17.08	2.325	23.28	23.31	17.05

DISTANCE	DEPTH = 0 KM.				DEPTH = 15 KM.				DEPTH = 40 KM.			
	EX.D.	I _r	I _h	I _o	EX.D.	I _r	I _h	I _o	EX.D.	I _r	I _h	I _o
80.0	3.280	16.95	16.95	16.95	2.872	19.20	19.20	16.95	2.345	23.10	23.14	16.92
80.5	3.305	16.83	16.83	16.83	2.895	19.05	19.05	16.83	2.365	22.92	22.96	16.80
81.0	3.333	16.70	16.70	16.70	2.919	18.91	18.91	16.70	2.384	22.76	22.79	16.67
81.5	3.359	16.58	16.58	16.58	2.944	18.76	18.76	16.57	2.403	22.59	22.62	16.55
82.0	3.387	16.45	16.45	16.45	2.971	18.60	18.60	16.43	2.423	22.43	22.44	16.43
82.5	3.417	16.31	16.31	16.31	2.998	18.45	18.45	16.30	2.443	22.24	22.25	16.29
83.0	3.448	16.17	16.17	16.17	3.027	18.28	18.28	16.15	2.471	22.03	22.03	16.13
83.5	3.482	16.02	16.02	16.02	3.057	18.11	18.11	16.01	2.499	21.81	21.81	15.97
84.0	3.517	15.87	15.87	15.87	3.088	17.94	17.94	15.86	2.526	21.60	21.60	15.82
84.5	3.554	15.72	15.72	15.72	3.120	17.77	17.77	15.70	2.551	21.40	21.40	15.68
85.0	3.590	15.57	15.57	15.57	3.151	17.61	17.61	15.56	2.576	21.22	21.22	15.55
85.5	3.621	15.44	15.44	15.44	3.179	17.46	17.46	15.43	2.598	21.05	21.05	15.43
86.0	3.647	15.33	15.33	15.33	3.203	17.34	17.34	15.33	2.620	20.89	20.89	15.32
86.5	3.670	15.24	15.24	15.24	3.224	17.23	17.23	15.23	2.640	20.75	20.75	15.21
87.0	3.693	15.15	15.15	15.15	3.245	17.13	17.13	15.14	2.659	20.61	20.61	15.12
87.5	3.718	15.05	15.05	15.05	3.265	17.03	17.03	15.05	2.677	20.49	20.49	15.03
88.0	3.743	14.96	14.96	14.96	3.286	16.93	16.93	14.96	2.693	20.37	20.37	14.94
88.5	3.765	14.87	14.87	14.87	3.306	16.83	16.83	14.88	2.709	20.26	20.26	14.86
89.0	3.785	14.80	14.80	14.80	3.325	16.74	16.74	14.80	2.723	20.16	20.16	14.79
89.5	3.801	14.74	14.74	14.74	3.342	16.66	16.66	14.73	2.736	20.08	20.08	14.73
90.0	3.813	14.70	14.70	14.70	3.353	16.61	16.61	14.68	2.747	20.00	20.00	14.68
90.5	3.821	14.67	14.67	14.67	3.358	16.58	16.58	14.66	2.757	19.94	19.94	14.63
91.0	3.825	14.65	14.65	14.65	3.359	16.58	16.58	14.66	2.758	19.89	19.89	14.60
91.5	3.828	14.64	14.64	14.64	3.361	16.57	16.57	14.65	2.769	19.86	19.86	14.57
92.0	3.831	14.63	14.63	14.63	3.364	16.55	16.55	14.64	2.771	19.84	19.84	14.56
92.5	3.833	14.62	14.62	14.62	3.368	16.54	16.54	14.62	2.772	19.83	19.83	14.56
93.0	3.836	14.61	14.61	14.61	3.371	16.52	16.52	14.61	2.774	19.82	19.82	14.55
93.5	3.840	14.60	14.60	14.60	3.374	16.51	16.51	14.60	2.777	19.80	19.80	14.53
94.0	3.844	14.58	14.58	14.58	3.377	16.49	16.49	14.58	2.780	19.78	19.78	14.52
94.5	3.848	14.57	14.57	14.57	3.381	16.48	16.48	14.57	2.783	19.76	19.76	14.50
95.0	3.851	14.56	14.56	14.56	3.384	16.46	16.46	14.56	2.786	19.74	19.74	14.49
95.5	3.854	14.54	14.54	14.54	3.387	16.45	16.45	14.54	2.789	19.73	19.73	14.48
96.0	3.858	14.53	14.53	14.53	3.390	16.44	16.44	14.53	2.791	19.71	19.71	14.47
96.5	3.861	14.52	14.52	14.52	3.393	16.42	16.42	14.52	2.794	19.69	19.69	14.45
97.0	3.865	14.51	14.51	14.51	3.396	16.41	16.41	14.51	2.797	19.68	19.68	14.44
97.5	3.869	14.49	14.49	14.49	3.399	16.39	16.39	14.49	2.799	19.66	19.66	14.43
98.0	3.872	14.48	14.48	14.48	3.403	16.38	16.38	14.48	2.802	19.64	19.64	14.42
98.5	3.876	14.47	14.47	14.47	3.406	16.36	16.36	14.47	2.805	19.62	19.62	14.40
99.0	3.879	14.45	14.45	14.45	3.409	16.35	16.35	14.45	2.808	19.60	19.60	14.39
99.5	3.883	14.44	14.44	14.44	3.412	16.33	16.33	14.44	2.810	19.59	19.59	14.38
100.0	3.887	14.43	14.43	14.43	3.415	16.32	16.32	14.43	2.813	19.57	19.57	14.37

TABLE—Continued

EXERCISE 9

SPECTRAL ANALYSIS

The purpose is to determine common spectral parameter: Seismic moment, corner frequency, source size and stress drop.

Exercise 1

Manual spectral analysis

Do exercise 3.4 from Appendix 2

Exercise 2

Spectral analysis of a local event using SEISAN

-Do SEISAN exercise 8, give screen dumps of results.

Exercise 3

Velocity and acceleration spectra

-Using the event for exercise 2, select a good station and make the velocity and acceleration spectra. Do not use station KONO since it has a low sample rate. Limit the frequency band of spectrum to range with good signal to noise ratio.

-Explain how spectra are expected to look and why.

-Do the spectra look as expected ?

-What is the y-axis unit of all 3 types of spectra ?

Question 4

Spectrum and Q

The spectral shape is dependent on the Q-values used for spectral correction. Make the P-wave displacement spectrum for the signal used for one station under exercise 2 using $Q_0=10$ and $Q_0=100$ and $q_{\alpha}=0.5$. The Q-value is changed in file MULPLT.DEF in directory DAT.

-Compare the spectral values and spectral shape and explain any differences.

EXERCISE 10

Analysis of a set of local events

Using the skills acquired in previous exercises, a set of 10 local events will be used to do a comprehensive analysis. The data set consists of 10 waveform files, a station file and calibration files.

Exercise 1

Create a data base with a name of your choice, register the events into the data base. Install calibration files and station files.

Exercise 2

Locate all events and calculate M_c , M_l and M_w , check all events for reasonable fit, RMS should be less than 1.0 s. Check that, for each event, that there is a consistency between different types of magnitudes.

Exercise 3

Make an epicentral map.

Exercise 4

Compare the magnitude types obtained using program mag. This means plotting M_l versus M_c and M_l versus M_w . How is the comparison ?

References

Bormann, P. (2002) IASPEI New Manual of Seismological Observatory Practice, GFZ Potsdam.

Kulhanek, O. Anatomy of seismograms, Elsevier

Payo, G. (1986) Introducion al analysis de sismogramas, Published by Instituto Geografico Nacional, Spain.

ANATOMY OF SEISMOGRAMS

OTA KULHÁNEK

**DEVELOPMENTS IN
SOLID EARTH GEOPHYSICS**

18

ELSEVIER

Chapter 4

SEISMIC WAVES

4.1 BASIC TYPES AND ESSENTIAL PROPERTIES

When the strain accumulated in the rock exceeds its elastic limit a fault ruptures, rock masses are abruptly displaced and seismic waves begin to radiate from the fault. As the rupture propagates, it successively releases the strain energy stored along the activated part of the fault. Thus, each point of the fault contributes, with a certain time delay (due to the finite velocity of the rupture propagation), to the total picture of seismic waves, which at a certain distance from the causative fault interfere with each other and give rise to quite a complicated wave train. At first sight, it seems that there is a contradiction between the duration of the rupture at the source, which takes between a fraction of a second and a few minutes, and the length of the observed seismogram which for large and distant earthquakes can extend over several hours. In fact, the length of the seismogram depends primarily on various wave propagation effects such as reflection, refraction, conversion, dispersion, etc and has very little to do with the duration of the quake. Seismologists use the term *coda* to denote the part of the seismogram with decreasing amplitudes which follows the principal phases.

Essentially, there are two types of seismic waves, **body waves** that propagate through the Earth's interior and **surface waves** that propagate along the Earth's free surface or along other discontinuities in the Earth's interior. Surface waves carry the greatest amount of energy from shallow shocks and are usually the primary cause of destruction that can result from earthquakes affecting densely populated areas. Body waves radiated by the source propagate in all directions (free waves) while surface waves start to propagate first after body waves (different types) have been interacting along boundaries. Thus, surface waves are always concentrated near discontinuity surfaces and are, therefore, sometimes called **bounded waves** or **guided waves**. In other words, for homogeneous media, i.e. for media with no boundaries, there are no surface waves.

Body waves, which travel faster than surface waves, are of two types: **compressional (longitudinal)** and **shear (transverse)**. That an elastic body should be able to transmit two different types of body waves was first postulated by S.D. Poisson in 1829. At any given point of the body, the velocity of propagation is determined by the density and elastic moduli at that point. Compressional waves travel about 1.7 times faster than transverse

waves and are often called *P* waves or primary waves (from Latin *undae primae*). Transverse waves are frequently called *S* waves or secondary waves (from Latin *undae secundae*). *P* waves are always the first among seismic waves that reach the recording station. Rock particles affected by a propagating *P* wave oscillate backward and forward in the same direction as the wave propagates (see Fig. 6), analogous to, e.g., sound waves. In the case of *S* waves, particles are displaced in planes perpendicular to the direction of travel (Fig. 6) analogous to, e.g., light or electromagnetic waves. However, since earthquakes generate *P* and *S* waves, studies of recorded seismic waves are, broadly speaking, more complicated than studies of sound or electromagnetic waves. Fluids do not sustain shear strain, and therefore *S* waves do not travel through liquid parts of the Earth's interior. *P* waves, on the other hand, propagate through both the solid and liquid divisions of the Earth. *P* and *S* waves had already been revealed on actual seismic records at the end of the nineteenth century.

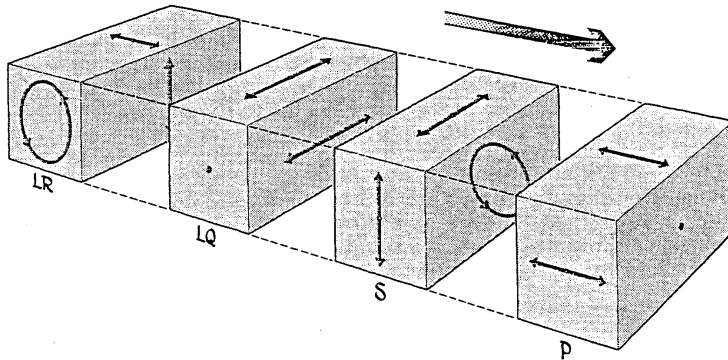


Fig. 6. Motion of rock particles (small arrows) that lie in the path of propagating *P*, *S*, *LQ* and *LR* waves. Note that the waves propagate from the source to the receiver at the recording site, i.e. from left to right in the sketch. Due to different propagation velocities, the waves will appear on the seismogram separated in time in the order: *P*, *S*, *LQ* and *LR*. The large arrow indicates the direction of wave propagation.

As far as surface waves are concerned, we shall here limit ourselves to a brief description of two basic types, namely to Love waves and Rayleigh waves which are often the dominant wave types seen on actual seismograms. It is usual to denote Love waves by *LQ* and Rayleigh waves by *LR* where *L* stands for long (i.e. long waves), *Q* for *Querwellen*, an alternative name from German for Love waves, and *R* for Rayleigh waves. *LR* and *LQ* waves propagate along the Earth's free surface or in layers bounded by velocity

discontinuities, through the crust and upper mantle. They can also travel by different modes (overtones) which are often seen on records as higher-frequency components superimposed on the surface-wave train. We talk then about fundamental-mode and higher-mode surface waves. Higher modes are most frequently observed for waves traversing purely continental paths. In some cases, higher modes have also been associated with oceanic paths. However, surface-wave higher modes disappear when the waves cross the transition between continental and oceanic structures. Higher modes propagate faster than the fundamental mode and are, therefore, recorded ahead of LQ and LR .

Amplitudes of LR and LQ waves are largest at or near the surface and decrease rapidly (roughly exponentially) with depth. Consequently, shallow (crustal) earthquakes generate large surface waves but with increasing focal depth, surface waves become smaller and smaller. For crustal earthquakes, surface waves usually dominate the seismogram while for deeper shocks ($h > 100$ km) they often become insignificant. Obviously, this fact provides the analyst with a powerful tool for a quick (at first glance) and reliable discrimination of shallow earthquakes against deep shocks.

Both Love and Rayleigh waves exhibit an important property called velocity dispersion or, for short, dispersion. The velocity of propagation of dispersed surface waves is not period (or frequency) invariant, as is the case of P and S waves, but increases with increasing wave period (normal dispersion). In practice, this means that the long surface waves approach the station first and are recorded ahead of the "slower" shorter waves. Hence, ideally the seismogram of surface waves LQ or LR will start with rather long-period motion which gradually, as time increases, will turn into shorter and shorter periods.

In Rayleigh waves, the motion of rock particles follows a retrograde elliptical orbit in a vertical plane pointed in the direction of the generating earthquake (see Fig. 6). In Love waves, there is no particle motion in the vertical direction. Particles move in a horizontal plane at right angles to the direction of the wave propagation (see Fig. 6). As in the case of body waves, different polarization of particle motions is an important clue which often makes it possible to distinguish between different surface waves LQ and LR . For example, as follows from the above description, vertical-component seismographs cannot record Love waves. Another important clue is that LQ waves travel somewhat faster and therefore precede LR waves on seismograms.

If the studied earthquake exceeds a certain magnitude, its seismic waves can be recorded by sensitive seismographs placed all around the world on the surface of the Earth, in boreholes, abandoned mines, on the ocean bottom,

etc. Generally speaking, as we depart from the focus, the wave amplitudes diminish due to the anelastic attenuation (rocks are not perfectly elastic), by geometrical spreading (the area of the wavefront increases with increasing propagated distance) and by losses at interfaces (reflection, refraction, mode conversion, diffraction, scatter). The anelastic attenuation is frequency dependent (high frequencies are subject to high attenuation) so that high-frequency seismic signals die out rather rapidly and may be recorded only by proper instruments placed at relatively short epicentral distances. The attenuation of geometrical spreading is frequency invariant.

Due to the internal structure of the Earth, at certain distance, e.g. around 20° or 144° , concentration (focusing) of energy of traveling seismic waves takes place. Seismic signals recorded close to these distances often show an increase of amplitude even with increasing distance, from the focus. This phenomenon, which is limited to a few rather narrow distance intervals, should be considered as an exception from the general behaviour of amplitudes decaying with increasing epicentral distance.

Other factors influencing the amplitude of arriving seismic waves are the source mechanism and the associated source radiation characteristics. Tectonic earthquakes, in contrast to underground explosions, cannot be treated as spherically symmetric point sources because the radiated seismic energy transported by certain wave types is beamed in certain directions. Therefore, two or more seismographs placed at the same epicentral distance but at different azimuths with respect to an earthquake may, and most likely will, show significantly different amplitudes of recorded seismic waves. It is also likely that seismographs deployed at different azimuths will show different amplitude ratios between arriving *P* and *S* waves.

The plot in Fig. 7 serves to illustrate some of the basic properties of body and surface waves described above. There is a sharp *P* onset followed after approximately three and a half minutes by a clear *S* onset (we neglect the minor trace wiggles). About two minutes after the *S* arrival, we observe a gradual increase of the amplitude due to the arriving *LR* wave (vertical-component seismogram). At the beginning of the *LR* wave, the wave period is about 40 s but it decreases to about 25 s after three or four swings, clearly demonstrating the normal dispersive character of the recorded *LR* wave. In this particular case (Fig. 7), the *LR* wave dominates the seismogram indicating a shallow-focus earthquake.

Since various types of seismic waves propagate with different velocities, they arrive at the recording site well separated in time so there should theoretically be no difficulties in their identification on seismograms. This behaviour has also been demonstrated by making use of the Greek earthquake record shown in Fig. 7. However, it has to be emphasized that in this

609

17

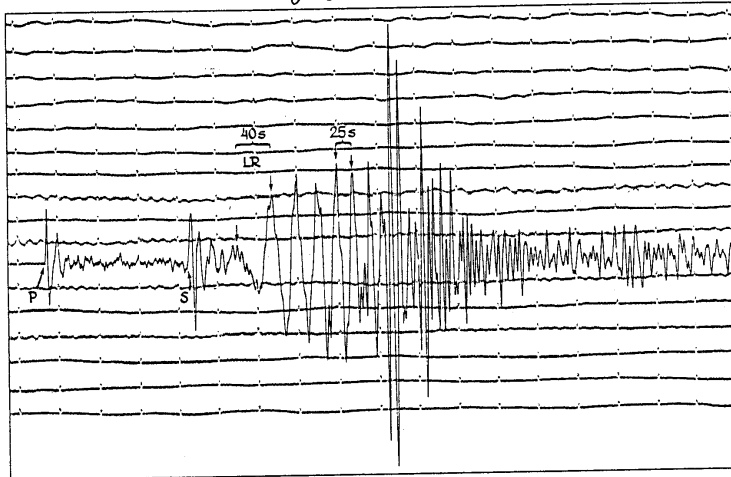


Fig. 7. Seismogram of the earthquake in northern Greece on May 23, 1978, (magnitude $M=5.7$, focal depth $h=9$ km), made at Uppsala, Sweden, at an epicentral distance of 2160 km. The trace has been made on a long-period Press-Ewing seismograph (see Chapter 6) and shows the vertical motion of the ground. Time advances from left to right and there is 1 minute between successive time marks (small upward offsets).

particular case, chosen for tutorial reasons, the noise level (of the portion of the record preceding the P onset) is very low when compared with amplitudes of recorded P or S waves. Also, the decay of P wave amplitudes, so called P coda, is rather rapid so that not only the P onset but also the S onset can easily be identified and the corresponding arrival times accurately measured. Unfortunately, it is quite common that the analyst, in his daily work, has to examine records with high background noise and to identify various wave arrivals masked by noise, which often is a task in itself. This may be especially true in cases of weaker and/or distant earthquakes.

The ground is practically always in motion. Various human activities such as traffic, construction work, industries etc generate so called cultural noise with dominant frequencies usually above 1 Hz. A similar type of noise is also generated by action of wind, smaller water basins or rivers etc. Various interactions between atmospheric effects, oceans and the solid Earth give rise to microseismic noise sometimes also called ocean microseisms. Dominant frequencies of microseisms occupy a broad low-frequency range from less than 0.01 Hz to, say, 0.5 Hz, i.e. periods from 2 s to more than 100 s. The most common microseisms have more or less regular periods of about 6 s.

Cultural noise is recorded with standard instruments at epicentral distances usually not exceeding several tens of kilometers and is, therefore, only of local importance. Microseisms, on the other hand, can travel many hundreds of kilometers and hence, are a continental phenomenon. They are correlated with stormy weather conditions in some adjacent oceanic regions and may persist from several hours to several days or weeks. Oceanic microseisms often show strong seasonal variations in both the amplitude level and the dominant period.

A variety of sources radiate a variety of noise types and to list commonly valid characteristics is rather difficult. Generally speaking, cultural noise due to its relatively high frequency content, affects records of near events (epicentral distance less than about 1000 km). Microseisms, on the other hand, interfere with records of distant events and make the interpretation difficult and sometimes even impossible. Examples of "noisy" seismograms are shown in Fig. 8.

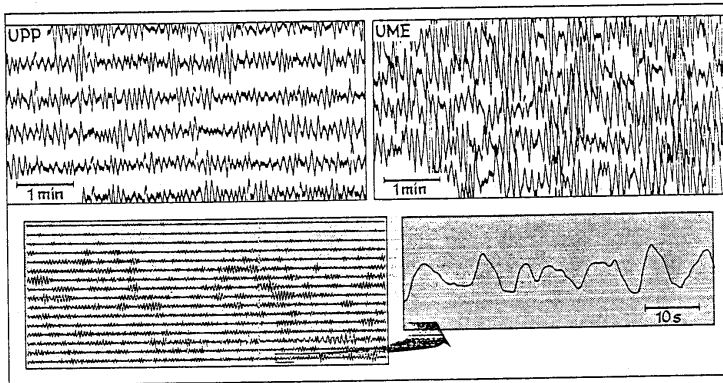


Fig. 8. Examples of seismograms with oceanic microseisms. Upper part: strong microseisms recorded on November 27, 1978 at Swedish seismographic stations Uppsala (left) and Umeå (right). In both cases, the traces are produced by standard long-period Press-Ewing seismographs and show the ground motion in the E-W direction. While the noise level in the Uppsala record would still allow the seismic phases to be picked, to identify weak arrivals in the Umeå record would certainly be a difficult task even for an experienced interpreter. Lower part: seismic noise recorded on November 22-23, 1986 by a broad-band vertical-component instrument at Gräfenberg, Bayern, FRG. The analog monitoring (left) and the enhanced analog display of the digital recording (right) are exhibited. The enhanced trace reveals the typical dominant period of 6-8 s. (Gräfenberg records provided by D. Seidl).

To complicate matters further, seismic waves encountering a discontinuity are reflected and/or refracted (at the Earth's free surface, seismic waves are reflected downward) and an incident *P* or *S* wave gives rise to both *P* and *S*

waves (mode conversion). Thus, a seismogram from a distant earthquake will often show a number of more or less distinct waves, commonly called phases, distributed in time, which have traveled along different propagation paths and which were subjected to different mode conversions P to S or S to P .

Wave energy is also scattered by velocity heterogeneities crossing the propagation path. For the given wave period, the scatter affects S waves more than P waves. Scattered waves reach the Earth's surface after the P wave and contribute to the buildup of P coda which in its turn obscures the later phases. Hence, except for the first P onset, all later arrivals are contaminated by codas of preceding phases so that on the record there is virtually no interval of quiescence between individual arriving phases.

Before we proceed further, it is worthwhile to summarize the most important characteristics of seismic waves which deserve our attention, and which are invaluable in any seismogram interpretation. Firstly, different waves travel with different velocities. At any epicentral distance, P is recorded first, followed by S , LQ and LR . Secondly, different waves are polarized in a different way (P linearly, LR elliptically, etc). This provides a means of identifying phase types. Thirdly, various phases show certain characteristic features (amplitude, period, dispersion, etc) which again are of primary importance for correct interpretation.

4.2 PROPAGATION PATHS

The propagation of seismic waves through the Earth's interior is governed by exact mathematical laws similar to the laws of light waves in optics. If the propagation velocities and other elastic properties were uniform throughout the Earth, seismic waves would radiate from the focus of the earthquake in all directions through the Earth along rectilinear paths or rays. In general, however, the wave velocity increases with depth and consequently, seismic rays are not straight lines but lines curved with the concave side upward providing the shortest time-path through the Earth. To be able to simulate various discontinuities in the Earth and at the same time to simplify the associated ray geometry, we shall, hereafter, assume the Earth to be a sphere, made of a finite number of concentric spheroidal homogeneous shells. Elastic properties vary from shell to shell but remain constant within each shell. For a spherical Earth model, it is common practice to express the distance between the focus and the recorded station as the angle (denoted Δ) subtended at the center of the Earth by the arc between the source and receiver ($1^\circ = 111$ km).

In the following discussion, we introduce, for the sake of clarity, three

different categories of seismic events. The classification is based upon the distance between the event and the recording site (i.e. upon the epicentral distance) which in its turn governs propagation paths along which seismic waves travel through the Earth's interior. The main reason for this classification, which does not provide any sharp line of demarcation, is that seismic waves from different categories may be discriminated from each other due to their different appearance on seismograms.

First, we shall consider waves from regional events, i.e. from events at epicentral distances not larger than about 10° . For this range of distances, a dominant portion of recorded seismic waves have propagated through the crust and/or along the Moho discontinuity and are commonly called **crustal waves**. The second category will include seismic waves recorded at an epicentral distance between 10° and about 103° . Within this distance range, seismograms are relatively simple and dominated by waves that have traveled through the mantle. The travel paths through the crust in the vicinity of the source (shallow focus) and the station are relatively short and often considered of less significance for the total appearance of the seismogram. The last category will treat seismograms obtained from epicentral distances 103° and larger. Records from these distances become complicated again and contain waves (phases) that have traveled through the Earth's core (**core waves**) or have been diffracted by the Earth's core. Earthquakes recorded at distances less than 10° are called **local events** or **regional events**, while shocks recorded from distances larger than 10° are called **teleseismic events** or simply **teleseisms**. Some agencies refer to events between 10 and 20° as regional and those beyond 20° as teleseismic.

4.2.1 Crustal waves; recording distances 0 - 10°

In order to explain the structure of seismic records made at epicentral distances between 0 and 10° (some workers use the limit 1000 km), let us first assume a much simplified structural model of the crust, depicted in Fig. 9. Note that for the distances considered here, we can neglect the effects of curvature of the Earth's surface.

Consider waves (rays) leaving the focus F and reaching the recording stations S_1 , S_2 and S_3 . Since the source radiates both P and S waves, there will be direct longitudinal and transverse waves recorded along the Earth's surface. These waves have ray paths such as FS_1 (see Fig. 9) and are encoded as Pg and Sg or sometimes as \bar{P} and \bar{S} . The subscript g indicates the travel path, which for seismic events in the upper crust (most of the crustal earthquakes) is entirely confined to the granitic layer. A reflected ray (e.g. ray path FR_1S_1) is also possible from the Moho, and the corresponding reflected P and S waves are labeled as PmP and SmS , respectively. Note that

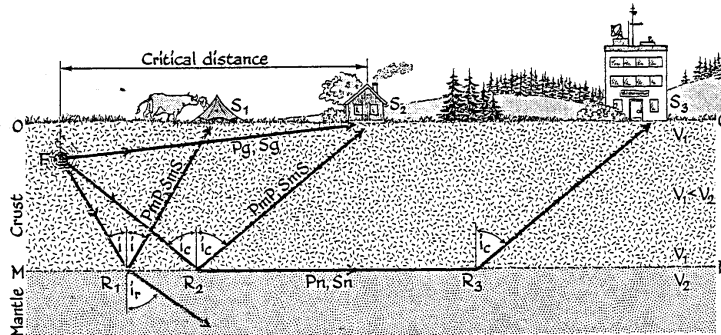


Fig. 9. Principles of wave propagation from the focus of earthquake F through a simplified one-layer crustal model. Symbols O and M designate the Earth's free surface and Moho discontinuity, respectively. S_k is the k -th recording seismographic station, i is angle of incidence, i_r is angle of reflection, i_c is critical angle and V is velocity of propagation for P or S . R_i are the points of reflection at the Moho discontinuity for rays that travel to the k -th station. Ray paths are defined by points of origin, reflection and recording. For example, FS_1 is the ray between the focus and station S_1 . For notation of crustal waves see the text.

in this case, it is only a part of the incident energy that is reflected from Moho back into the crust and recorded at S_1 . The rest of the energy is refracted into the mantle and will never show up on the record made at S_1 . It follows from Fig. 9 that as the epicentral distance increases, the angle of incidence i and the angle of refraction i_r also increase. At a certain critical epicentral distance, $i_c = 90^\circ$, which means that the energy of the refracted ray does not penetrate into the mantle but travels along the Moho discontinuity (cf the ray path FR_2S_2). The associated angle of incidence, i , called the critical angle, is denoted i_c . Corresponding P and S waves called head waves, recorded at S_2 are labeled P_n and S_n , respectively. Waves propagating along discontinuities separating two layers with two different velocities move with the higher of the two velocities. Thus, P_n and S_n waves depicted in Fig. 9 travel with velocities of the uppermost mantle. As can be seen in the figure, P_g and S_g exist for all epicentral distances from $\Delta = 0$ and outwards whereas P_n and S_n phases cannot be observed at distances shorter than that corresponding to the location of the station S_2 (Fig. 9), i.e. at distances shorter than the critical distance, which for the continental crust is about 100 km.

Structural models, like the model depicted in Fig. 9, should be as simple as possible to make the seismogram interpretation manageable. On the other hand, the model should also be accurate enough to reflect the actual

structure. Evidently, these are two opposing constraints and a proper compromise must, in each particular case, be made to make the interpretation possible. It should be stressed that in the above presentation and in Fig. 9, a number of simplifications has been made.

Firstly, a homogeneous, one layer, crust will in many cases be a rather poor approximation of the true structure. It is common to employ two crustal layers, separated by the Conrad discontinuity, to interpret crustal phases. In special studies, multilayered crustal models are used.

Secondly, the true Moho and Conrad discontinuities are not planar and strictly horizontal boundaries. In reality, they will show a certain dip and some degree of undulation. Therefore, a two-layer crustal model with somewhat irregular boundaries, as shown, in Fig. 10, will be more realistic than that discussed above (Fig. 9). Further refinements of the model in terms of additional discontinuities and their geometry will here be considered as a domain of research rather than of an analyst in his daily seismogram interpretation.

Lastly, the assumption of Pg or Sg traveling as direct waves (P or S) over large distances, as shown in Fig. 9, is again a gross simplification. The true case is that direct waves, denoted \bar{P} and \bar{S} , are recorded only from local events, i.e. at very short epicentral distances usually not exceeding several tens of kilometers. Pg and Sg waves are then understood as channel or refracted waves traveling along less pronounced boundaries within the granitic layer.

Accepting the model in Fig. 10, we realize that starting from a certain epicentral distance, approximately 100 km, we record new phases, namely the refracted P and S traveling along the Conrad discontinuity. An asterisk in the superscript position, P^* and S^* , indicates this phase. An alternative code sometimes used is Pb and Sb . The subscript b refers to basaltic layer.

At very short distances, less than 150 km or so, the first seismic wave arriving at the recording station is \bar{P} or Pg , traveling with a velocity of about 6 km/s. For distances larger than critical but less than about 150 km, Pg is followed by P^* and Pn , in this order. P^* and Pn travel with velocities of about 6.6 and 8.0 km/s, respectively, i.e. significantly faster than Pg . Therefore, at distances larger than approximately 150 to 200 km (depending upon the true propagation velocities and thicknesses of the granitic and basaltic layers) crustal waves change their order of arrival. For distances larger than about 200 km, the first arriving phase is Pn , next arrives P^* and then Pg . Obviously, this is true only for continental travel paths. Seismograms from earthquakes beneath the sea bottom, made at island or coastal stations, will not show Pg or Sg phases since there is no granitic

I
O
Crust
M
Mantle
Fig.
di.
fig.
la
cr
H
di.
di.
if
w
 \bar{P}
th
th
o:
c:
b:
e:
T.
o:
th
o:
ci

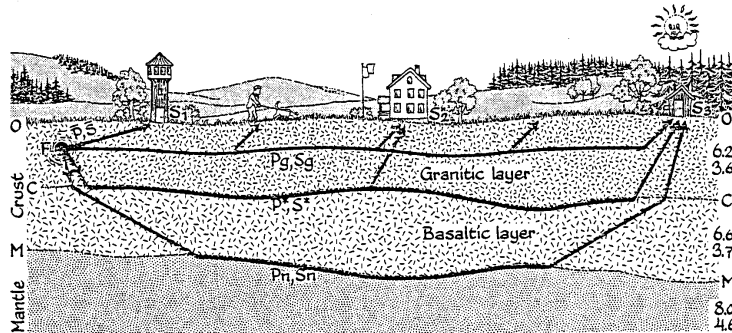


Fig. 10. Principles of the wave propagation through a continental crust consisting of two layers with dipping and non-planar interfaces. Symbol *C* designates the Conrad discontinuity and figures in the right margin give approximate velocities of propagation in km/s for *P* (upper figures) and *S* waves (lower figures). Conventions as for Fig. 9.

layer in the oceanic crust. Similarly, earthquakes originating in the lower crust, beneath the Conrad discontinuity, do not produce *Pg* or *Sg* phases. Hence, first arrivals on records from these earthquakes will be *Pn* or *P**.

For ease of phase identification, rather than relying on the epicentral distance, which of course may not be available, we can make use of time differences between arrivals of various phases (see Chapter 5). For example, if the arrival-time differences *S-P* is less than about 20 s, the first wave within the *P* and *S* group to arrive at the recording site is probably *Pg* (or \bar{P}) and *Sg* (or \bar{S}), respectively. If on the other hand, the difference is more than 25 s, the first arrival is most likely *Pn*. Details obviously depend upon the true structure and upon the focal depth. It should be emphasized that only seldom are all the above phases identified on one record. The usual case is that one or several of these waves are too weak or hidden in the background noise to be discernible on the seismogram.

With a certain time delay following the *P* phases, proportional to the epicentral distance, the crustal *S* waves arrive in the same order as *P* waves. Thus, for local events (earthquakes, mine explosions, quarry blasts, etc) the order of *S* onsets will be *Sg*, *S**, *Sn* while for events from distances larger than about 300 km we observe first *Sn* followed by *S** and *Sg*.

As far as *P* or *S* waves reflected at Moho are concerned, corresponding onsets on seismograms are rather scarce and difficult to identify. The best chance to record *PmP* or *SmS* is at very short distances where the

contamination by P_g and P_n (or S_g and S_n) is not severe. In rare instances, additional so called depth phases, arriving between P_n and P_g , are present on seismograms. These leave the focus as P waves, travel upward with a small angle of incidence, are reflected as P at the free surface and continue further as P_n . Notation for this phase is pP_n . Similarly, sP_n denotes a depth phase leaving the focus as S , converted through the reflection at the free surface and continuing as P_n . Ray paths of pP_n and sP_n are depicted in Fig. 11. Both pP_n and sP_n are of great importance in focal depth estimations but at the same time rather difficult to identify on actual records.

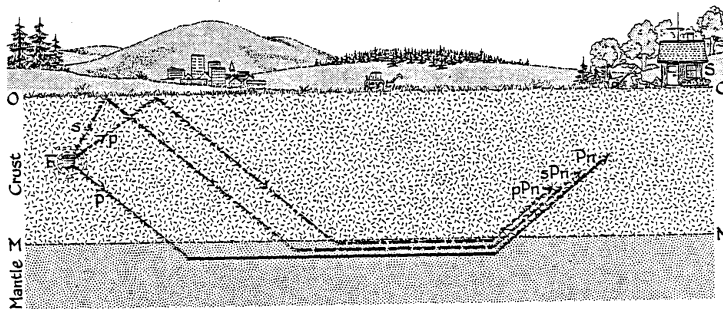


Fig. 11. Principles of propagation of P_n , pP_n and sP_n waves. For the sake of graphical simplicity, an one-layer crustal model is used. Conventions as for Fig. 9.

Short-period S waves multiply reflected between the free surface and Moho, or between other crustal velocity discontinuities, interfere with each other and give rise to a wave group labeled L_g which follows the S_g arrival. The subscript g again refers to granitic layer. At distances of several hundred kilometers and larger (continental paths), L_g waves, which propagate as guided waves, supercritically incident on the Moho and multiply reflected within the crust, and with a typical velocity of about 3.5 km/s, may dominate the seismograms, especially the horizontal channels. L_g is usually recorded at epicentral distances of about 5° and larger. Cases are known where L_g propagated over distances of several thousand kilometers (e.g. from USSR-China border region to Sweden, see Plate 33) and were recorded as prominent phases on the seismograms.

Near-surface regional events (earthquakes, industrial explosions, rockbursts etc) also generate short-period surface waves of Rayleigh type, labelled R_g . The presence of short-period R_g in the seismogram is a reliable indicator of a very shallow event with focal depth of the order of one or a few

kilometers. On the other hand, if short-period *Rg* waves are absent (near station, epicentral distance of several hundred kilometers or less), we are concerned with a deeper natural event, i.e. with a crustal earthquake at a depth most likely between about 5 to 25 km, since all types of man-made events as well as triggered mine tremors can be excluded. Short-period *Rg* waves, which travel as guided waves through the crust across continental paths with velocity of 3 km/s or slightly higher, are exposed to more effective attenuation when compared with crustal body waves and their range of propagation is therefore limited to distances less than about 600 km (Båth, 1983). However, at short epicentral distances, of say, less than 100 or 200 km, the *Rg* phase from a near-surface event often dominates the recorded wave train (see Plate 5).

Seismic waves from local and regional earthquakes of low or moderate magnitude are of short period and therefore almost exclusively recorded by short-period seismographs. The seismogram length depends upon the magnitude but generally does not exceed 5 minutes or so. The number of clear pulses seen on the record, indicating arrivals of various *P* and *S* waves, is often higher than one would expect from models displayed in Figs. 9, 10, and 11, demonstrating the departure of models used from the true structure. For continental travel paths, the most prominent phase is usually *Sg*, best recorded by horizontal-component instruments. Generally speaking, *Sg* arrivals start with large amplitudes which successively decrease as the time increases forming the coda of the event. Coda duration is related to the magnitude. *Rg* phases, best recorded on vertical-component seismograms, often display a clear dispersion. As an example, a record from a regional earthquake is displayed in Fig. 12. The first discernible phase is *Pn*, weakly recorded on the vertical component. It is followed by *Pg*, *Sn* and *Sg* which are recognizable on all three channels. Largest amplitudes are exhibited by the *Lg* wave trains on the two horizontal channels. The focal depth of about 15 km prevents the development of *Rg* waves. Note the high-frequency character of all recorded phases.

Strong events (magnitudes about 6 and larger) recorded at local or regional distances ($\Delta < 10^\circ$) will produce seismograms with duration of several hours. Associated large amplitudes of ground vibrations often saturate the recording system (clipped records) and the resulting seismogram is not of much use except for measuring the arrival time and polarity of the very first recorded phase. In this respect, digital systems with higher dynamic range are superior to analog instruments (for more details see Section 6.4).

Similar to the LVL in the upper mantle, there is also a low-velocity channel in the deep ocean. Depending upon the salinity and temperature of water, the sound velocity decreases from the sea surface to a minimum of about 1.5 km/s at about 700 - 1300 m depth and increases again from that

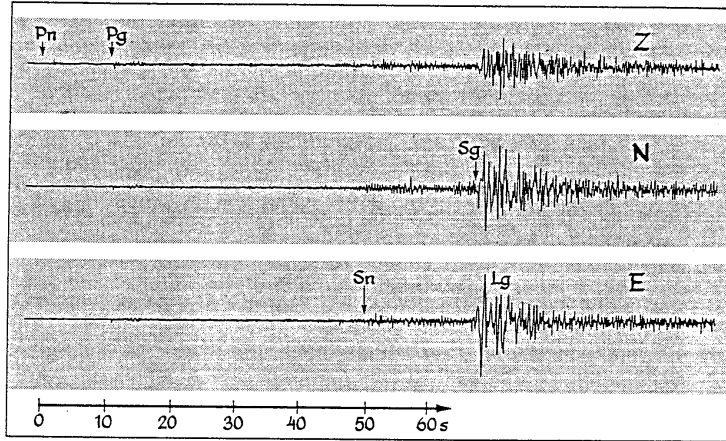


Fig. 12. Vertical (Z) and horizontal (N, E) component seismograms from a moderate size regional earthquake. The event occurred off coast of southwestern Sweden on June 15, 1985 at focal depth of 15 km (magnitude $M_L = 4.6$). The traces are analog displays of broad-band digital recording (see Chapter 6) made at Uppsala at an epicentral distance of 490 km. (Traces computer plotted by W.Y. Kim).

depth to the bottom. The depth region of low velocity in the ocean, called SOFAR (sound fixing and ranging), provides extremely favourable conditions for long-distance propagation of a special type of high-frequency seismic wave.

Island and coastal seismographic stations frequently record these waves termed *T* waves (tertiary waves) arriving after *P* and *S* and characterized by propagation within the oceans as ordinary sound waves. Seismic waves emitted by earthquakes near the sea bottom or by submarine volcanic eruptions are refracted through the sea floor and propagate as sound (longitudinal) waves through the ocean. The propagation of *T* waves, generally by the SOFAR channel (Bullen and Bolt, 1985) or by multiple reflections between the sea floor and the sea surface (Båth and Shahidi, 1974), is very efficient and observations at distances as large as about 80° have been reported (see Plate 49). First observation of *T* waves was made by D. Linehan in 1940.

T waves are best recorded by ocean-bottom seismometers (OBS) and by coastal and island stations (see Plate 14). However, instruments deployed further on land sometimes also record clear *T* waves after a water-land

conversion of sound waves into P , S or surface waves propagating over the land portion of the total transmission path. If this is the case, the labeling is TPg , TSg and TRg , reflecting the fact that the path of propagation over the land is within the crust. An example of recorded TSg phase is given in Fig. 13. T waves are short-period waves, with periods usually less than 1 s, recorded exclusively by short-period seismographs. On records, they often exhibit rather monochromatic oscillations with a gradual increase and decrease of amplitudes of total duration up to several minutes (Fig. 13). Some workers (Báth and Shahidi, 1974) report inverse dispersion observed in T wave trains. When compared e.g. with P waves, there is no sharp onset in the T wave group which obviously creates difficulties when reading the T arrival times or when identifying phases within the T wave group. In general, there is great variety in the appearance of T phases due to the dependence upon the bottom topography in the vicinity of generation, oceanic stratification and water-land conversion and transmission (Báth and Shahidi, 1974).

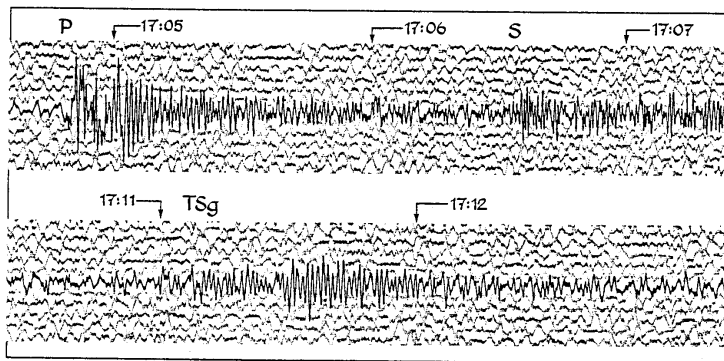


Fig. 13. Short-period vertical-component record from a shallow ($h = 33$ km) earthquake in Norwegian Sea made at Umeå, northern Sweden. This earthquake occurred on November 21, 1967 ($m = 5.4$) at a distance of 10° from Umeå. The seismogram shows clear P and S onsets, separated by 107 s. Approximately 6 min after P , an onset labeled TSg is identified on the record. It corresponds to a wave propagating through the water as a sound wave and, subsequent to a water-land conversion and refraction, as Sg over the land path. In this particular case, the land path is about $1/3$ of the total travel length. The TSg wave shows oscillations with periods around 1 s and gradually increasing and decreasing amplitudes. The whole TSg wave train lasts for about 2 min.

During the last 10 years, or so, observed T phases have proved very useful in discriminating between underground nuclear explosions, detonated beneath oceanic islands, and tectonic earthquakes (Adams, 1979). For this type of explosion, the energy is injected directly into the SOFAR channel and

recorded T phase amplitudes often exceed those of associated P wave by a factor of up to 30.

As follows from the above description, for epicentral distances less than about 10° , the wave propagation is rather complicated. The seismogram appearance varies from place to place due to regional variations in crustal structure and consequently, for this distance range, it is difficult to list generally valid clues for record interpretation. Nevertheless, some of the following principles may guide the analyst to read correctly seismograms of local and regional earthquakes.

- 1) Predominant periods of recorded crustal phases such as P_g , P^* , P_n , S_g , S^* , S_n , etc are normally less than one second and hence best recorded by short-period instruments. R_g periods are usually not longer than several seconds.
- 2) It has often been observed that S_g has the largest amplitude (for cases when large short-period R_g is missing), best seen on horizontal-component records.
- 3) For epicentral distances less than about 200 km (depending upon the crustal structure and focal depth), the first arriving phase is P_g . For larger distances, P_n arrives first.
- 4) Near-surface events from distances less than about 600 km often generate short-period R_g with clear dispersion, best seen on vertical channels.
- 5) Local and regional earthquakes of low or moderate magnitude are characterized by short total record duration, usually not longer than several minutes.
- 6) Island and coastal seismographic stations frequently record various kinds of T phases.

It is not always possible for analysts to identify correctly crustal phases from the records of a single station, although this may be easier if several stations of a network are read together. If there is doubt about correct interpretation, a phase should simply be identified as P or S .

4.2.2 Body waves; recording distances 10 - 103°

Seismologically speaking, the mantle differs from the overlying crust also in the fact that, in the first approximation, it may be considered as a laterally homogeneous, i.e. as a spherically symmetric body. Seismic wave velocities indeed increase with depth, however, the regional (lateral) irregularities, typical for the crust, are almost absent (less distinct) in the mantle. Some workers consider the distance range between 10 and 103° as ideal to record not only the direct P and S waves, but also the whole family of reflected and converted waves. Travel paths of these waves are dominated by the

mantle and corresponding seismograms are relatively simple.

To explain various features of waves traveling through the mantle, let us consider the Earth's cross section, a surface focus event and travel paths of the more important body waves depicted in Fig. 14. Note that for the distance range of $10-103^\circ$ studied here, we have to introduce the spherical shape of the Earth. A flat Earth model, used in the case of crustal waves, is no longer appropriate. As mentioned above, seismic rays in the true Earth are not straight but bent upwards due to the velocity increase with depth. This means that waves traveling to more distant stations penetrate the earth to greater depth than those traveling to near stations. Because of greater depth, the velocity of propagation is larger, i.e. P and S waves reach the more distant stations more quickly than might be expected. In other words, there is a non-linear relation between the distance and travel time for P as well as for S waves (see Chapter 5).

At distances around 10° , P_n and S_n become difficult to identify in the records, except in some shield areas and other regions with relatively uniform structures. Instead, teleseismic P and S phases become visible on seismograms. P is usually stronger on the vertical component, while S is more clearly seen on horizontal components. S often exhibits wave trains with longer periods when compared with corresponding P . Large-amplitude S waves are often observed at distances of up to about 100° .

Body waves that lie entirely in the mantle and undergo no reflection between the focus and the recording station are labeled with a simple symbol P or S . Rays corresponding to travel paths of these direct waves (P or S), also called elementary waves or main waves, are displayed in Fig. 14. They depict paths of least travel time from the focus of the earthquake to the recording site. Direct waves, when reflected one or more times from the underside of the free surface, give rise to single or multiply reflected P or S . For example, the direct P reflected from the free surface back into the mantle once or twice, is called PP or PPP , respectively. In the same way, we have also SS , SSS etc. Each letter, P or S , in the symbol defines one leg of the propagation path. Considering also the conversion from P to S , and vice versa, on reflection, we may observe the wave denoted PS which travels as P from the focus to the reflection point at the free surface and from that point to the recording station as S . PS and SP appear only at distances larger than 40° . For a wave leaving the focus as P and twice reflected/converted from the free surface, we have four possible cases, namely PPP , PPS , PSP and PSS . Some of these waves are sketched in Fig. 14. Obviously, we could continue with three and more reflections/conversions and form the corresponding wave symbols. However, from experience we know that it is quite seldom that three and more reflections from the Earth's free surface are clearly visible on actual seismograms. For distances larger than about 40° , the

free-surface reflected phases become very distinct. At distances around 100° and larger, PP and SS often belong to the largest recorded body waves.

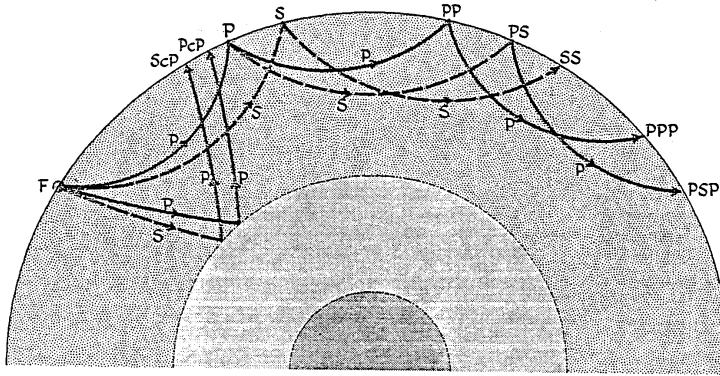


Fig. 14. Examples of propagation paths of direct and reflected waves in the Earth's mantle. Solid and dashed rays are used to distinguish between P and S waves, respectively. Waves are generated by the surface focus, F , of the earthquake which radiates both P and S waves. Different shadings show the mantle, outer core and inner core. For notation see the text.

A symbol c is used to indicate a single upward reflection, i.e. a reflection back into the mantle from the outer core-mantle boundary. For instance, ScP (Fig. 14) corresponds to an S wave which travels down from the focus, strikes the boundary, is reflected and converted into the P type wave and finally is recorded at the Earth's surface as ScP . A straightforward extension provides PcP , ScS and PcS . Because these phases emerge steeply, ScP is usually stronger on vertical components than PcS . Large reflected core phases are usually recorded at shorter epicentral distances, say at 40° or less. At distances around 39° , ScP and PcS (surface foci) are often contaminated with the arrival of direct S and the phase separation is difficult. When the ray path of PcP grazes the outer core boundary, the combination of direct P and PcP is called P diffracted. This case is discussed in more detail below. Core reflected waves together with $PmKP$ (see Section 4.2.3 for notation), recorded from earthquakes at a wide range of distances and focal depths are used to study the properties of the core-mantle boundary.

Waves ascending from the focus to the free surface, where they are reflected back into the mantle, are commonly called **depth phases** and are denoted by a lower case prefix: p for longitudinal and s for transverse waves. We can easily list the four possibilities of reflections near the epicenter,

with
the
re-
pre-
ses-
ph-
for
the
ca-
de-
de-
ar-
be-
str

Fig
F.

SS
fro
Pc
dic
at
ma

which are pP , sP , pS and sS (Fig. 15). The first case, for example, denotes the wave that traveled upward from the focus as P (short leg) and had been reflected back off the free surface again as P (long leg). Depth phases, primarily pP , are the most important phases routinely used in focal-depth estimations. It is quite obvious that the deeper the focus, the later is the pP phase in relation to P . Hence, accurately measured arrival-time differences pP - P are reliable indicators of the depth of the focus. In the case of a deeper focus, it is sometimes possible to recognize several different reflections from the free surface. Such waves are then labeled pPP , pPS , pSP and pSS in the case of waves with their short leg as P . Logically, sPP , sPS , sSP and sSS denote corresponding waves with short leg as S (Fig. 15). Interpretation of depth phases must be done with utmost care since, for example, pP from a deep earthquake can easily be erroneously interpreted as P when the first arrival (P) is weak. Depending on focal orientation and other factors, sP may be stronger than pP and may be mistaken for it. Depth phases are sometimes stronger than the main P wave, and may be the first readable phase.

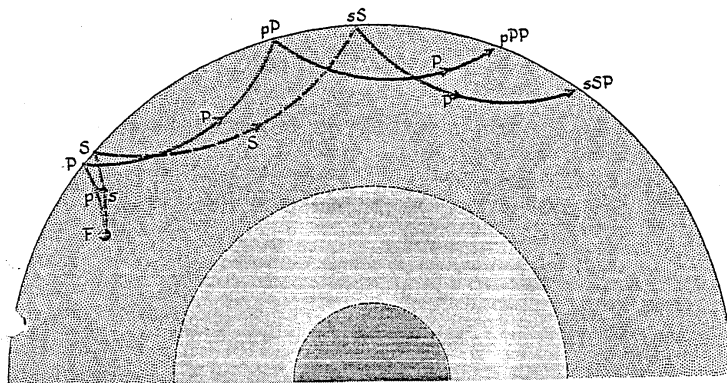


Fig. 15. Examples of propagation paths of depth phases and their notation. Waves begin at the deep focus, F , of the earthquake. Conventions as for Fig. 14.

The lower case symbol d (or its value in kilometers) inserted between PP , SS , etc has been introduced by B.A. Bolt to indicate seismic waves reflected from secondary discontinuities in the upper mantle. For example, symbols $P400P$ or $P650P$ (Fig. 16) specify P waves reflected at the underside of a discontinuity at a depth of 400 or 650 km, respectively. These phases arrive at the recording station ahead of the expected (calculated) arrival time for the main PP phase and are frequently interpreted as reflections from upper

mantle discontinuities (i.e. as *PdP*). However, when the arrival time cannot be explained in terms of known discontinuities as *PdP*, we call these onsets early *PP* or precursors to *PP*.

4.2.3 Body waves; recording distances 103° and larger

It was noticed in the early days of observational seismology that amplitudes of direct *P* waves decay dramatically at distances larger than 100° . The short-period *P* waves reappear consistently on records first at distances of about 140° and larger. Correspondingly, the distance range $103^\circ < \Delta < 140^\circ$ is called the shadow zone. Within this zone, there is no penetration of direct *P* waves due to the wave diffraction around the Earth's core (Fig. 16). The last direct *P* wave reaches the Earth's surface at an epicentral distance of about 103° where the shadow zone produced by the Earth's mantle commences. *P* waves traveling beyond this distance creep around (are diffracted) the core-mantle boundary and lose a large part of their energy there, so that only weak, diffracted *P* phases are observed in this distance range. Similar to dispersion (see Section 4.1), diffraction also depends on the wave period (or frequency). The longer waves are diffracted more into the shadow zone than shorter waves. The diffracted *P* waves are labeled *Pc* (or *Pdif*, *Pdiff*). Seismological centers like the National Earthquake Information Center (NEIC) in Golden, Colorado, or ISC in England use *Pdif*. On seismograms, *Pc* waves usually show small amplitudes, emergent or gradual onsets and the energy shifts to longer periods. Long-period *Pc* are sometimes observed out to distances of 160° or more. *S* waves are affected at the core-mantle boundary in a similar way; the symbol *Sc* (or *Sdif*, *Sdiff*) is used for diffracted *S* waves. The shadow zone for *S* waves on the side of the Earth opposite the earthquake, extends over all epicentral distances from about 103° to -103° (257°).

Direct *P* and *S* waves and corresponding reflections are easily distinguishable from the recorded surface waves. The former usually occupy the period interval from, say, 1 to 5 s, while the latter show large amplitudes (surface or shallow shocks) and periods in the interval from about 10 to 100 s. The period of *S* waves increases with distance and, in cases of multiple reflection may reach even several tens of seconds.

As mentioned above, the limiting ray path which is tangential to the core in the real Earth is that corresponding to an epicentral distance of about 103° . *P* and *S* waves recorded at distances greater than 103° graze or strike the surface of the core, the wave pattern becomes rather complicated and amplitudes decay dramatically. Seismic waves which leave the source with a steeper descent than the grazing waves, strike the core-mantle boundary and are subsequently divided into reflected and refracted waves. The former are

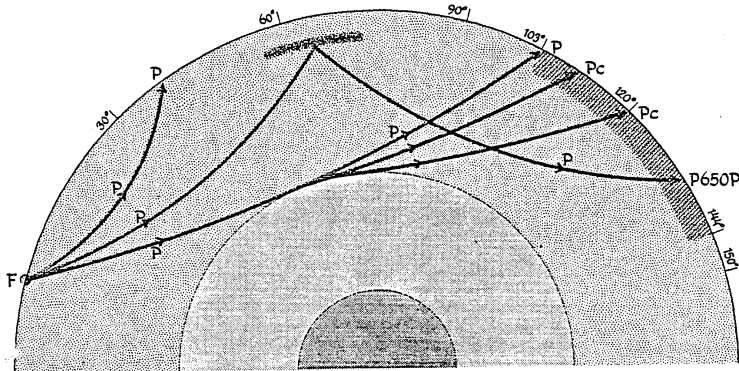


Fig. 16. Examples of propagation paths of direct P waves, P waves diffracted around the core-mantle boundary and P waves reflected downwards at a discontinuity at 650 km depth. The discontinuity and the shadow zone ($103\text{--}144^\circ$) are shaded. Conventions as for Fig. 14.

reflected back into the mantle as PcP , PcS , ScP or ScS , while the latter, called core phases, are refracted downward and enter the core. The refraction is rather sharp because of the sudden significant drop of P velocity beneath the core-mantle boundary (see Fig. 5).

A P wave penetrating the outer core is denoted by K (from German *Kernwellen* for core waves). After traveling through the outer core and following another partitioning (reflection or refraction) at the outer core boundary it emerges at the Earth's surface. Thus, we can form the four symbols for waves which have traveled through the outer core: PKP , PKS , SKS and SKP . For example, the symbol PKS corresponds to a wave that starts in the mantle as a P wave, is refracted into the outer core as a P wave and is finally, after mode conversion, refracted back in the mantle as S . The phase SKP is stronger on vertical components than PKS . These phases have a caustic near 130° and at this distance are often the only phase recorded on short-period instruments. Some of the seismic rays traversing the core are illustrated in Fig. 17. It has to be emphasized that the symbol K always represents a P wave since S waves do not enter the outer core. The notation PKP is sometimes abbreviated as P' .

For initial ray paths which are only slightly steeper than the ray grazing the core surface, corresponding PKP waves emerge at the Earth's surface at distances beyond 180° (see Fig. 17). As the rays (surface-focus event) enter

the mantle more and more steeply, the core refractions become less and less abrupt and the rays emerge at the Earth's surface at shorter and shorter epicentral distances. This decreasing of distance stops at about 144° . Further steepening of the initial ray paths results now in an increase of the distance of emergence up to 165° or so. The phenomenon may be viewed in terms of two *PKP* travel-time branches denoted *PKP1* and *PKP2* for the first and the second arrival, respectively. Exactly at 144° , the waves from the two branches coincide, the waves reinforce one another which gives rise to an energy concentration near that distance. The point of largest energy concentration is called a caustic point or simply caustic. It has to be stressed that neither *PKP1* nor *PKP2* enter the inner core, i.e. both these wave types have their deepest point of penetration in the outer core.

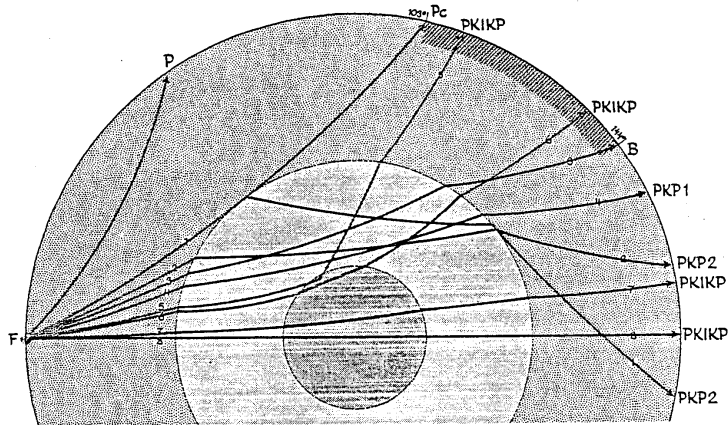


Fig. 17. Examples of propagation paths of *P* waves traveling through the Earth's core. The shadow zone between 103° and 144° is shaded and *B* denotes the caustic point. Rays are numbered in the order of increasing steepness of the initial descent. For details see the text. Conventions as for Fig. 14.

As we further steepen the initial ray path, we reach the family of rays that enter the inner core (Fig. 17). These rays progress in a normal way, i.e. the steeper the initial ray path, the greater the distance of emergence from about 110° until at last there is a ray that passes through the Earth's center and reaches the Earth's surface at the antipode of the focus. *P* waves that traverse the inner core are denoted by *I*, giving rise to phases *PKIPK*, *PKIKS*, *SKIKS* and *SKIKP*, although these are often still simply referred to as

PKP, *PKS* etc. Phases with an *S* leg in the inner core would include the letter *J*, such as *PKJKP*, but these have never been unambiguously identified on seismograms. For obvious reasons, both the symbols, *I* and *J*, have to be accompanied on both sides by *K*. Rays corresponding to seismic waves reflected at the outside and inside of the inner core are called *PKiKP* and *PKIIKP*, respectively (Fig. 18).

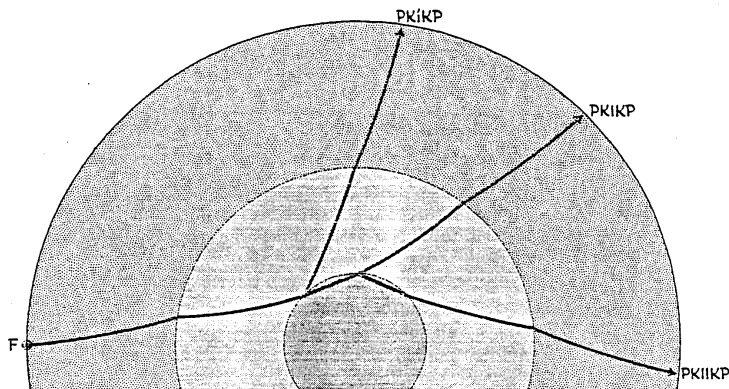


Fig. 18. Propagation paths of *P* waves traversing the Earth's interior from the focus *F* and reflecting at the outside (*PKiKP*) or inside (*PKIIKP*) of the inner core. *PKiKP* is a *P* wave refracted into the outer core and through the inner core. Conventions as for Fig. 14.

If the studied event is weak, then usually no *Pc* is observed in the entire distance interval $\Delta > 103^\circ$ and the first arrival seen on the record will be that of *PKP*. At epicentral distances $105\text{-}120^\circ$, *PKiKP* usually provides the first onset discernible on the seismogram.

In the region of the caustic, i.e. around 144° , the wave train of recorded core phases becomes particularly complicated. It is first at distances beyond the caustic point where observed onsets may be separated into individual *PKP* branches. The energy distribution changes with the increasing distance. *PKP1* is the dominant branch just beyond the caustic, up to about 153° . In records of weaker events ($144\text{-}153^\circ$), *PKP1* is often the first visible onset since *PKiKP*, theoretically preceding *PKP1*, is too weak to be observed. As the distance increases, *PKP1* becomes weaker and vanishes from records at distances of about 160° and larger. For distances beyond, say, 157° , *PKP2* usually dominates the seismogram. Some workers prefer the nomenclature

adopted from travel-time charts with branches denoted AB , BC and DF (Jeffreys and Bullen, 1967). Arrivals associated with these branches are then labeled PKP_{AB} , PKP_{BC} and PKP_{DF} and correspond to PKP_2 , PKP_1 and $PKiKP$ arrivals, respectively. The CD branch (PKP_{CD}) is related to $PKiKP$ arrivals which are due to seismic waves reflected at the outside of the inner core.

$PKiKP$ in the distance range from about 125° to the caustic is often preceded by early arrivals or precursors which can arrive many seconds ahead of the main phase. These are best explained by scattering phenomena at or near the core-mantle boundary.

In a similar way as above, we may form new symbols for the whole family of waves propagating through the core. For example, $PKKP$ is a P wave which has been reflected from the inside of the core-mantle boundary. $PKKP$ is often very pronounced on records made at distances between 60 and 80° . The striking onset may easily be misinterpreted as a first P arrival of another event. P waves trapped inside the Earth's liquid core and with multiple K legs are called $PmKP$ where $m-1$ provides the number of reflections. Cases like $P4KP$ and $P7KP$ have been reported (Bolt, 1982).

$PKPPKP$, or for short $P'P'$, are PKP waves once reflected from the free surface back to a station in the same hemisphere as the focus. Since PKP has the caustic at 144° , one might also assume that the strongest reflection will take place at that distance, and consequently the best chance to observe $P'P'$ is around distances of $2 \times 144^\circ = 288^\circ$, or 72° if we take the shortest distance from source to station: $P'P'$ is often well recorded, arriving about 30 minutes after the P phase when most of the coda amplitudes of preceding phases have already become faint, and it may in some cases be wrongly interpreted as a new P or PKP . 72° is also equivalent to $3 \times 144^\circ = 432^\circ$ or $(360 + 72)^\circ$ so the phase $P'P'P'$ is also strong at this distance, and may be observed for strong earthquakes about another 20 minutes after $P'P'$.

In the late 1960's, first observations of forerunners to $P'P'$ were made. These were interpreted as $P'dP'$. Analogous to PdP , $P'dP'$ waves are not reflected at the opposite surface of the Earth (as is the case of $P'P'$) but at some discontinuity in the upper mantle. For example, $P'650P'$ travels from the hypocentre to the other side of the Earth, where it is reflected back to the station from a layer 650 km below the surface. $P'650P'$ passes through the core twice and on the seismogram precedes $P'P'$ by about 2 minutes. Some close precursors within about 30 s of the main $P'P'$ arrival can arise from asymmetrical reflections.

Let us now shift our attention from P to S waves. Similarly to PKP , there are SKS waves, i.e. S waves traveling from the earthquake source down

through the mantle. Incident to the outer-core boundary they undergo a mode conversion and as P (the K leg) traverse the liquid outer core. Following an inverse mode conversion, they again enter the mantle as S and emerge at the Earth's surface as SKS . Analogous phases to $PmKP$ are $SmKS$. First SKS waves are observed at distances between 60 and 70° and the range of observations extends out to distances of 180° or so. Depending upon details in the structural model, SKS exhibits a caustic point at a distance of about 80° so that the best region to study SKS waves is that between 70 and 90° . However, the phase identification has to be made with utmost care since SKS waves recorded in this distance region are often contaminated with direct S waves. At about 82° , SKS begins to arrive ahead of S . For distances shorter than about 95° , SKS is usually smaller than S , however at distances beyond 95° , SKS amplitudes are often quite large. To mistake S for SKS and vice versa will adversely affect the epicentral location. Since the epicentral distance estimate is frequently governed by the observed arrival-time difference S - P , (see Chapter 5) wrong S identification on the record will provide a wrong epicentral distance which in its turn will result in erroneous location. S and SKS are best recorded on long-period horizontal-component seismograms. However, occasionally these body waves are also observed on short-period records, although the onset time of the later of the two phases is usually very emergent due to the contamination by the coda of the earlier phase. An example of recorded S and SKS is shown in Fig. 19.

The period of SKS phases may reach several tens of seconds and is, therefore, best recorded by long-period horizontal seismographs. On the other hand, the best sensing of PKP , $PKKP$, $PKIKP$ etc. is with short-period vertical instruments.

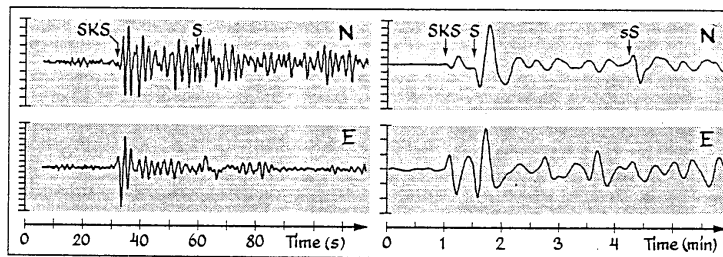


Fig. 19. Analog displays of digital short-period (left) and long-period (right) seismograms from a deep-focus earthquake in the Fiji Islands region recorded by the Chiang Mai station in Thailand, at an epicentral distance of 90° . Both horizontal components are shown. The earthquake occurred on April 29, 1987, with magnitude $m = 5.9$, at a depth of 390 km. At this epicentral distance the SKS precedes S . The short-period records reveal a clear SKS , however the S arrival, about 30 s apart, is hidden in the SKS coda. The long-period traces show both SKS and S and also the depth phase sS . After G. Choy (personal communication).

4.2.4 Body waves from intermediate-focus and deep-focus earthquakes

In the early days of observational seismology, the focal depth of recorded earthquakes was often a topic of speculation even though there were strong indications (such as surface faulting or the limited area of destruction) that many of the earthquakes must have been rather shallow events. On the other hand, early in this century several investigators (Pilgrim, 1913; Turner, 1922) found a number of events with focal depths greater than 100 km. Somewhat later, Japanese scientists (Wadati, 1927; Shida, 1937) presented evidence that Japanese earthquakes occur at practically all depths down to 500 km. They based their conclusions upon observed S - P arrival time differences, intensity distributions and different appearances of intermediate- or deep-focus earthquakes and of those that take place at shallow depth. Wadati noted very early that the seismograms of intermediate-focus and deep shocks display rather impulsive and large S phases, shorter predominant periods and less well developed codas. In this context, it is perhaps interesting to mention that during the 1920's the Japan Meteorological Agency (JMA) already operated an excellent regional network of seismographic stations (Frohlich, 1987).

Later studies confirmed conclusions from Wadati's pioneering work that intermediate and deep-focus shocks produce simpler seismograms with exceptionally well recorded impulsive body waves while surface wave amplitudes decrease as the earthquake becomes deeper. Strong depth phases, such as e.g. pP and sS , are also frequently very distinct on records from deep events. However, the duplication of principal phases by surface reflections often complicates the seismogram interpretation. Another important characteristic that accentuates the difference between shallow and deep shocks is the pattern of aftershocks. While large shallow earthquakes are usually followed by numerous aftershocks, deep events (which may be multiple shocks) virtually never show well developed aftershock series.

As an example, Fig. 20 displays several records made at teleseismic distances from the Sea of Okhotsk earthquake which occurred at a depth of 580 km. Note the rather impulsive appearance of P , PcP , pP and especially S and ScS (E-W component, short-period trace) which are all easily identified on the seismogram. Practically no surface waves were recorded from this event.

Strong intermediate-focus and deep earthquakes occur in several different seismically active regions. Among these are: island arcs such as Tonga-Kermadec Islands, the Marianas, New Hebrides Islands or the Aegean arc; continental margins with deep ocean trenches like Central America and western South America; mountain chains e.g. Himalayas (Hindu Kush) or Carpathians. About one fifth of all reported earthquakes take place at a focal depth exceeding 70 km. Among the deepest known earthquakes are three in

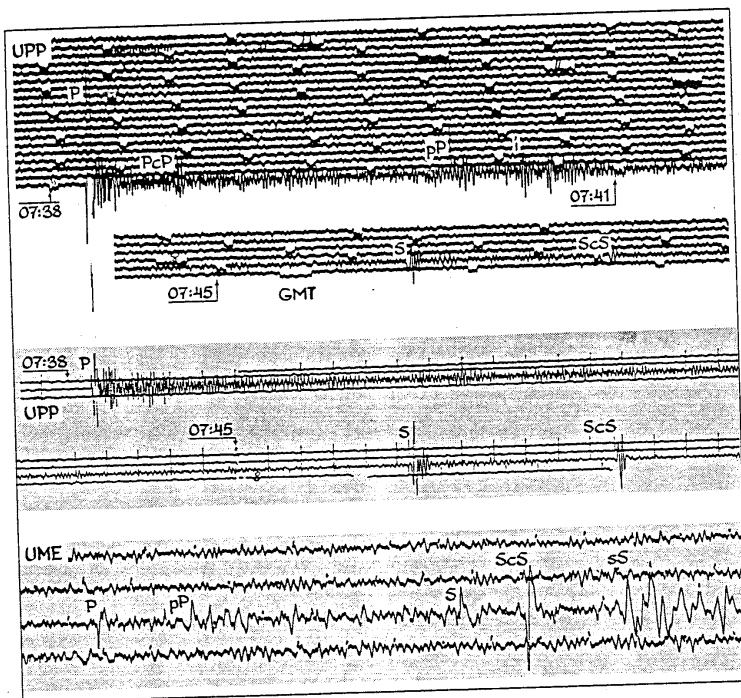


Fig. 20. Seismograms from a moderate size (magnitude $m = 5.8$), deep-focus earthquake recorded at Swedish stations Umeå (UME) and Uppsala (UPP) at epicentral distances of 60 and 64°, respectively. The event occurred in the Sea of Okhotsk on February 1, 1984 at a focal depth of 580 km. The uppermost two traces show the short-period Benioff (see Chapter 6) vertical-component record made at UPP. The middle two traces exhibit the short-period S-13 (see Chapter 6) E-W component seismogram also made at UPP. The bottom trace presents the long-period vertical-component record made at UME. Note the rather impulsive character of recorded phases, in particular that of S and ScS, clearly visible in all three records. Virtually no surface waves have been recorded from this event.

the Flores Sea area, on August 25, 1933, June 29, 1934 and June 30, 1943. Their depths are given by Gutenberg and Richter (1938) as 720 km, although other agencies have placed them rather shallower. ISC records contain four recent events in the Fiji-Tonga area with depths greater than 750 km: January 15, 1981 (765 ± 17 km), November 21, 1982 (769 ± 31 km), October 25, 1972 (806 ± 84 km) and May 7, 1971 (848 ± 26 km). These events are all small and not widely recorded, and their depths, particularly those of the

deepest two, cannot be regarded as well established. Occasionally, deep-focus earthquakes occur in rather unexpected geographical areas. For instance, up to 1954, it was generally accepted that the geographical extent of deep quakes is limited to the Circum-Pacific belt. However, on March 29, 1954, an isolated major earthquake occurred in southern Spain at a depth of 630 km. A smaller earthquake occurred at the same focus on January 30, 1973.

Even though several alternative hypotheses to explain deep earthquakes have been launched in the past (e.g. contraction of the Earth due to cooling), today, nearly all seismologists agree that deep and intermediate-focus events are associated with the subducting lithosphere which fits nicely with the idea of plate tectonics. It is of course, still possible that individual shocks, e.g. that of March 29, 1954, may not be related to subduction. Notwithstanding the unifying frame of plate tectonics, it is likely that deep and shallow events are generated by fundamentally different modes of rock failures. For example, it is possible that deep shocks are not associated with dislocations along quasiplanar fault surfaces. Some researchers now ascribe deep quakes to phase transitions taking place in the upper mantle or in other words to sudden voluminous changes (densification) due to the collapse of olivine (a major mineral in the Earth's mantle) molecules from the low-pressure form into a more dense form. However, the relation between phase transitions, generation of deep earthquakes and the style of mechanical failure associated with these quakes is still poorly understood and debated. Other plausible models explaining the mechanism of earthquakes at great depth, such as dehydration of minerals or an abrupt build up of the frictional heat, have also been proposed (see e.g. Frohlich, 1989).

On the whole, the most distinctive features of a large intermediate-focus and deep earthquake recorded at teleseismic distances pertinent to seismogram interpretation are the seismogram simplicity, small amplitudes or even absence of surface waves and an impulsive shape of body waves. With some elementary experience, all these characteristics may often be revealed as the eye scans the seismogram. In a more retrospective-type interpretation, the absence of aftershocks will support the classification of the shock as a deep or intermediate-focus event.

4.2.5 Surface waves

It can be shown that the amplitude decrease for body waves (P and S) is inversely proportional to the propagated distance while for surface waves the decrease in amplitude is inversely proportional only to the square root of the distance traveled. Hence, with exception of very short epicentral distances, surface waves carry by far the largest amount of wave energy radiated by shallow and some intermediate-focus earthquakes. In Section 4.1, we showed

that interaction of body waves along velocity discontinuities generates various types of surface waves and presented some of their essential properties. In the following lines we complement the previous discussion with more details pertinent to interpretation of recorded surface waves.

In 1885, Lord Rayleigh proved theoretically that a special type of surface wave (now called Rayleigh wave and labeled *LR*) can propagate along, i.e. beneath, the Earth's free surface. Contrary to other types of surface waves, propagation of *LR* waves is not limited to layered media; they can also be transmitted through a homogeneous half-space (semi-infinite medium). As discussed earlier (see Section 4.1), the particle motion of Rayleigh waves follows a retrograde elliptical orbit in the vertical plane containing the direction of propagation. At the Earth's surface, the amplitudes in the vertical and horizontal directions are related roughly as 3:2. Hence, Rayleigh waves are usually best seen on vertical-component seismograms. Amplitudes of *LR* waves decrease rapidly (exponentially) with increasing depth. For example, at a depth equal to one wavelength, the vertical and horizontal amplitudes fall to 0.11 and 0.19 of their free-surface values, respectively. The velocity of Rayleigh waves in a homogeneous medium, c_R , lies between 0.87 and 0.96 times the *S*-wave velocity, v_s , of the half-space. For many rock materials the Poisson ratio is approximately 0.25 which leads to a relation $c_R = 0.92v_s$.

In 1911, A.E.H. Love solved the theoretical problem of wave propagation through a thin superficial layer superimposed on a homogeneous half-space. Assuming that the *S*-wave velocity in the layer is lower than that in the material below, another type of surface wave (called Love wave and designated *LQ*) can be transmitted through the layer without any significant penetration of energy into the lower medium. Love waves may, therefore, also be considered as channel waves, in this particular case transverse waves, trapped in the superficial layer. In contrast to Rayleigh waves, Love waves show no vertical motion since particles excited by propagating *LQ* waves are polarized in the horizontal plane perpendicular to the direction of propagation. Consequently, traces of *LQ* waves should be looked for on the horizontal-component seismograms. Love waves propagate faster than Rayleigh waves with velocities limited by *S*-wave velocities in the layer and the half-space. The mean velocity of propagation is 4.43 and 3.97 km/s for *LQ* and *LR*, respectively (Bullen and Bolt, 1985).

The analyst has essentially two clues to distinguish *LQ* waves from *LR* waves. Firstly, the different particle motion. While Rayleigh waves usually show the largest amplitudes on vertical-component records, Love waves are best displayed on horizontal-component seismograms. Secondly, the different propagation velocities. Both *LQ* and *LR* propagate slower than *P* or *S*, but since *LQ* propagates faster than *LR*, they are recorded ahead of *LR* waves.

Surface waves traveling through layered media often show appreciable normal dispersion which as time goes on, continually changes the shape of both LQ and LR . Due to the dispersion, the original appearance of the wave train becomes disturbed on the seismogram by long period waves advancing toward the beginning of the wave train as it travels through the medium. This rather special behaviour, leads to the concept of phase velocity, c , and group velocity, U . The former is the velocity with which a wave of single frequency (monochromatic signal) propagates. The latter is the velocity of travel of the wave train energy, i.e. the velocity of the wave train envelope. Plots of wave velocity as a function of period (frequency) are called dispersion curves. Figure 21 displays empirical average group velocity dispersion curves for fundamental mode Love and Rayleigh waves. Observe that the shape of curves in Fig. 21 depends strongly upon the character of the propagation path. In the period range from about 20 to 60 s, continental travel paths exhibit dispersion curves for LR waves with group velocity gradually increasing from 2 to almost 4 km/s. For LQ waves, the group velocity starts at about 2.5 km/s and reaches values close to 4.5 km/s at periods of several hundreds of seconds. As follows from the figure, dispersion curves associated with oceanic travel paths show a rather abrupt change in the short-period range. At periods around 15 s, the velocity of LR increases sharply from about 1.5 to more than 3 km/s. For LQ wave, a sudden velocity rise from about 3 to 4 km/s is seen at periods around 7 s.

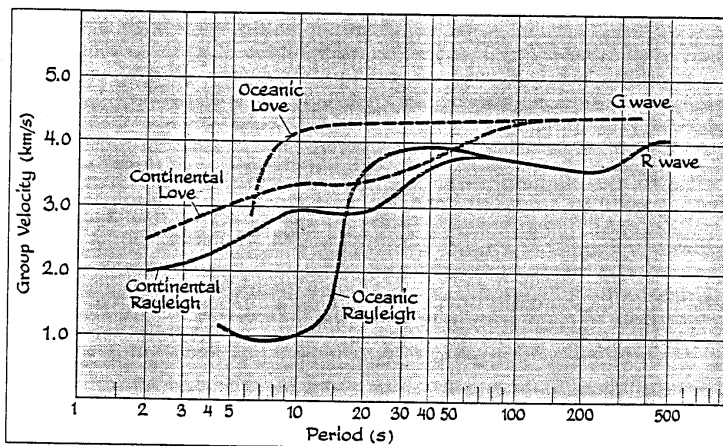


Fig. 21. Dispersion curves for group velocity for fundamental Love and Rayleigh waves that have traveled along oceanic and continental paths (based on the diagram of Bullen and Bolt, 1985).

An experienced analyst will distinguish between recorded surface waves that have traveled along pure oceanic or continental paths. Dispersion characteristics of oceanic routes give rise to long wave trains with rather slow and sometimes hardly visible period change over relatively long (5-10 minutes) record segments. Several typical seismograms are displayed in Plates 34 and 50. In contrast, continental paths generate a characteristic fast period decrease with time, which is often easily recognized by inspecting several minutes of the records (see e.g. Fig. 7 and Plates 22 and 39). As indicated above, the exact shape of dispersion curves depends upon the traversed structure. This means that available empirical dispersion curves for LQ or LR waves provide the researcher with remarkably effective probes for studying the structure of the traversed medium (so called inverse problem).

As can be seen in Fig. 21, dispersion curves show a rather complicated pattern with several local minima and maxima. Surface waves traveling with these minima or maxima group velocities are called Airy phases. On seismograms, an Airy phase is characterized by a constant-frequency compact wave train, often with a remarkable amplitude buildup of dispersed surface waves traveling by fundamental-mode propagation.

At short epicentral distances, it is difficult to identify LQ and LR waves because they are often contaminated by large-amplitude S waves. On the other hand, at large distances, the identification is rather simple since LQ and LR waves dominate the record (shallow events) and are significantly delayed with respect to S waves. On seismograms, surface waves may be spread over several hours.

Figure 21 displays another interesting feature which should be discussed in more detail. Observe that the dispersion curves for LR waves (both the oceanic and continental paths) show a local minimum for periods around 200 s. In the period range from approximately 50 to 200 s, the group velocity is monotonically decreasing with increasing period. Physically this means that in this period range, long-period Rayleigh waves follow the laws of inverse dispersion. Observations of this interesting phenomenon are rather scarce, however one example is displayed in Plate 30.

Periods of the largest (maximum amplitude) recorded surface waves show a clear positive correlation with epicentral distance. For example, for distances 10, 50 and 100°, the expected minimum periods, T_{min} , of the largest continental Rayleigh waves are of the order of 7, 13 and 16 s, respectively (Willmore, 1979). For oceanic passages, the periods can be somewhat longer. Also the time occurrence of the beginning of the maximum movement, T_{Rmax} (Rayleigh wave), with respect to the first onset of P waves, T_p , is obviously distance dependent. Table 1 gives the time differences $T_{Rmax} - T_p$ for various epicentral distances Δ (after M. Bath, 1947, abbreviated). Hence, the position

of the maximum amplitude in the *LR* wave train, with respect to the *P* arrival, and its period offer the interpreter important information on the epicentral distance of the earthquake.

TABLE 1
Travel-time differences, $T_{Rmax} - T_p$, and minimum periods, T_{min} , for largest Rayleigh waves observed at various epicentral distances Δ (from B ath, 1947 and Willmore, 1979).

Δ	$T_{Rmax} - T_p$	T_{min}	Δ	$T_{Rmax} - T_p$	T_{min}	Δ	$T_{Rmax} - T_p$	T_{min}
10°	6.2 min	7 s	60°	35.0 min	14 s	110°	63.7 min	
15	9.1	8	65	37.8		115	66.6	
20	12.0	9	70	40.7		120	69.5	
25	14.8		75	43.6		125	72.3	
30	17.7	10	80	46.5	16	130	75.2	
35	20.6		85	49.3		135	78.1	
40	23.5	12	90	52.2		140	81.0	18 s
45	26.3		95	55.1		145	83.8	
50	29.2		100	58.0		150	86.7	
55	32.1		105	60.8		160	92.5	

As mentioned earlier, surface-wave amplitudes are large only close to the Earth's free surface and decrease, broadly speaking, rather rapidly with increasing depth. Consequently, a shallow-focus earthquake will usually generate large dominating surface waves, often exceeding the amplitudes of recorded body waves, while a deep-focus earthquake of the same magnitude will generate abnormally small (insignificant) surface waves. This feature obviously provides the interpreter with a viable tool to discriminate, at first glance, between shallow events and deep-focus earthquakes.

With the advent of long-period instruments, comparatively long-period surface waves, so called mantle waves, have been observed from large distant shocks. These waves can be of either Love- or Rayleigh-wave type with approximate periods of somewhat less than one minute to several minutes. The speed of the *LQ* type mantle waves is often nearly constant at 4.4 km/s (see Fig. 21) and the wave has an impulsive shape on the seismogram. The *LR* type mantle waves travel with a velocity between 3.6 and 4.1 km/s. Since the wavelength of mantle waves varies from several hundreds to more than thousand kilometers, a large part of the Earth's mantle is affected by these waves. An interesting feature of mantle waves is their repeated appearance on records, which is due to their multiple travel around the Earth. The *LQ* type mantle wave was given the label *G* (after B. Gutenberg) and the *LR* type mantle wave, the label *R*. The older nomenclature sometimes uses *W* instead for *R* (from German *Wiederkehrwellen*, meaning repeated waves). *G* waves that propagate the

direct and anticerter routes are labeled $G1$ and $G2$, respectively. Waves which have in addition traveled once around the Earth are denoted $G3$ and $G4$, and so on. Accordingly, we have $R1$, $R2$, $R3$, $R4$ etc. On many occasions, observations of up to $G8$ and $R8$ have been made. As an exceptional case we may mention records of the 1960 Chile earthquake, $M=8.3$. Seismograms made at Uppsala, Sweden, reveal mantle waves $G20$ and $R20$ which have traveled a total distance equal to that from the Earth to the Moon (Båth, 1979a).

Travel times for $h=0$																		
Δ	P_g		P^*		P_n		S_g		S^*		S_n		$S_g - P_g$		$P_m P$		R_g	
km	m	s	m	s	m	s	m	s	m	s	m	s	m	s	m	s	m	s
0	0						0						0					0
10	1.6						2.8						1.2					3.3
20	3.2						5.6						2.4					6.6
30	4.8						8.4						3.6					9.9
40	6.4						11.2						4.8	13.7				13.2
50	8.0						14.0						6.0	14.2				16.6
60	9.6						16.8						7.2	15.1				19.9
70	11.3						19.6						8.3	16.1				23.2
80	12.9						22.3						9.4	17.2				26.5
90	14.5						25.1						10.6	18.3				29.8
100	16.1						27.9						11.8	19.5				33.1
110	17.7	18.7	20.8				30.7			36.8			13.0	20.8				36.4
120	19.3	20.2	22.1	33.5			33.5			39.0			14.2	22.1				39.7
130	20.9	21.7	23.3	36.3			36.3			41.2			15.4	23.4				43.0
140	22.5	23.2	24.6	39.1			39.1			43.4			16.6	24.8				46.4
150	24.1	24.7	25.9	41.9			41.9			45.6			17.8	26.1				49.7
160	25.7	26.2	27.2	44.7	45.9		44.7	45.9	47.7	47.7			19.0	27.5				53.0
170	27.3	27.7	28.5	47.5	48.6		47.5	48.6	49.9	49.9			20.2	28.9				56.3
180	28.9	29.2	29.7	50.3	51.4		50.3	51.4	52.1	52.1			21.4	30.3				59.6
190	30.6	30.8	31.0	53.1	54.1		53.1	54.1	54.3	54.3			22.5	31.8	1 02.9			
200	32.2	32.3	32.3	55.9	56.8		55.9	56.8	56.5	56.5			23.7	33.2	1 06.2			
210	33.8	33.8	33.6	58.7	59.5		58.7	59.5	58.7	58.7			24.9		1 09.5			
220	35.4	35.3	34.8	1 01.4	1 02.2		1 01.4	1 02.2	1 00.9	1 00.9			26.0		1 12.8			
230	37.0	36.8	36.1	1 04.2	1 04.9		1 04.2	1 04.9	1 03.1	1 03.1			27.2		1 16.2			
240	38.6	38.3	37.4	1 07.0	1 07.6		1 07.0	1 07.6	1 05.3	1 05.3			28.4		1 19.5			
250	40.2	39.8	38.7	1 09.8	1 10.3		1 09.8	1 10.3	1 07.5	1 07.5			29.6		1 22.8			

Fig. 25. Sample section ($0 \leq \Delta \leq 250$ km) of travel-time tables for near events with surface focus in Sweden. Times of travel are listed for P_g , P^* , P_n , S_g , S^* , S_n , $P_m P$, R_g and for the difference $S_g - P_g$. (After Båth, 1979b).

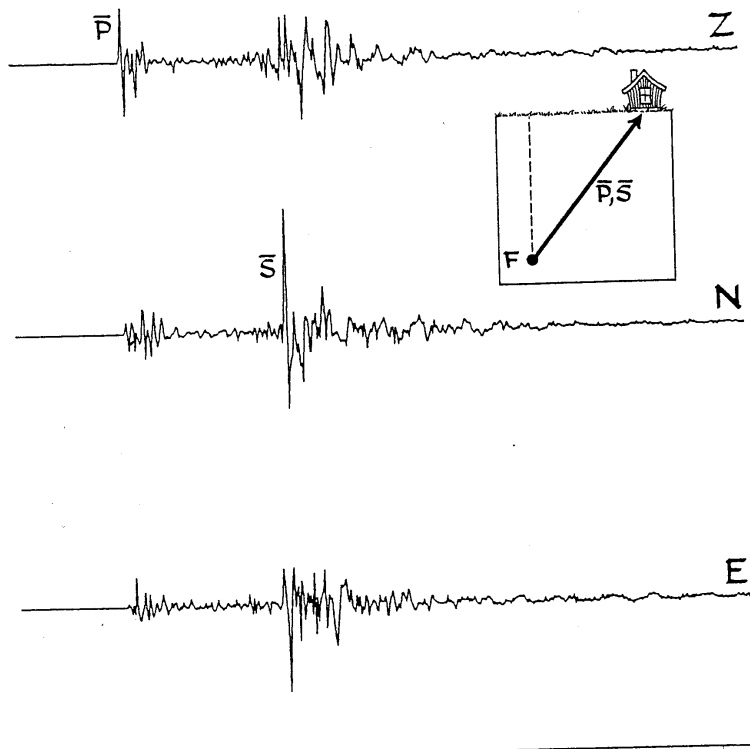


Plate 1. Direct \bar{P} and \bar{S} waves from a local microearthquake, $M_L=1.8$, recorded at Matsushiro, Japan, on July 11, 1986. The epicentral distance is 5.4 km and the focal depth 6.9 km. All three components recorded by a short-period seismograph are displayed. Due to the short epicentral distance, the waves travel close to vertical (see the inset) which in its turn results in large \bar{P} amplitudes on the vertical component and significantly smaller amplitudes on both horizontal components. Obviously, for \bar{S} , the relation is the reverse. The short epicentral distance does not permit the other crustal phases to develop. There are 2 s between successive time marks at the bottom of the plate.

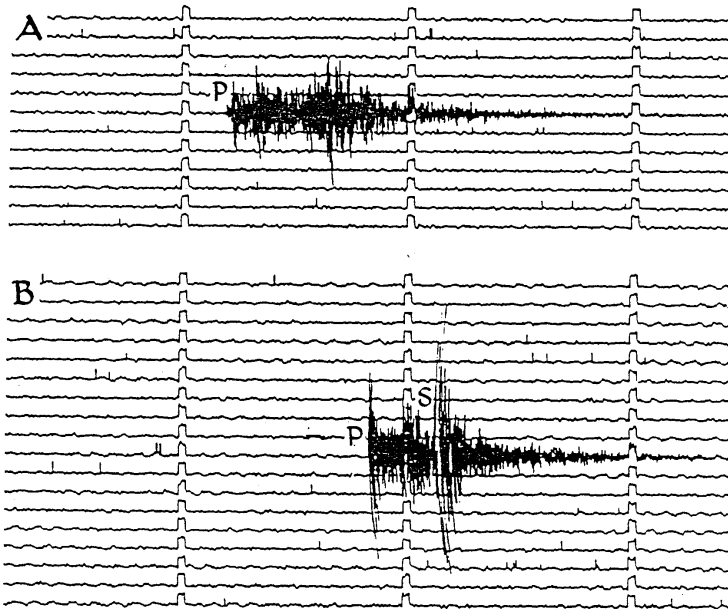


Plate 8. Short-period vertical-component seismograms of a shallow (A) and intermediate-focus (B) earthquake in the Fiordland region of New Zealand made at Clyde, New Zealand. Source parameters of the two events are the following:

Event	Date	M_L	Epicentral coordinates		Focal depth	Epicentral distance
A	Mar 23, 1985	3.7	45.16°S	166.46°E	12 km	225 km
B	Mar 19, 1985	4.0	45.09°S	167.50°E	106 km	144 km

In spite of comparable magnitude and hypocentral distances, the two records look differently. As is generally the case, *P* and *S* phases are more pulse like and better defined for the deeper event B. The seismogram of this event also shows less complexity between the *P* and *S* phases when compared with that from the shallow earthquake A.

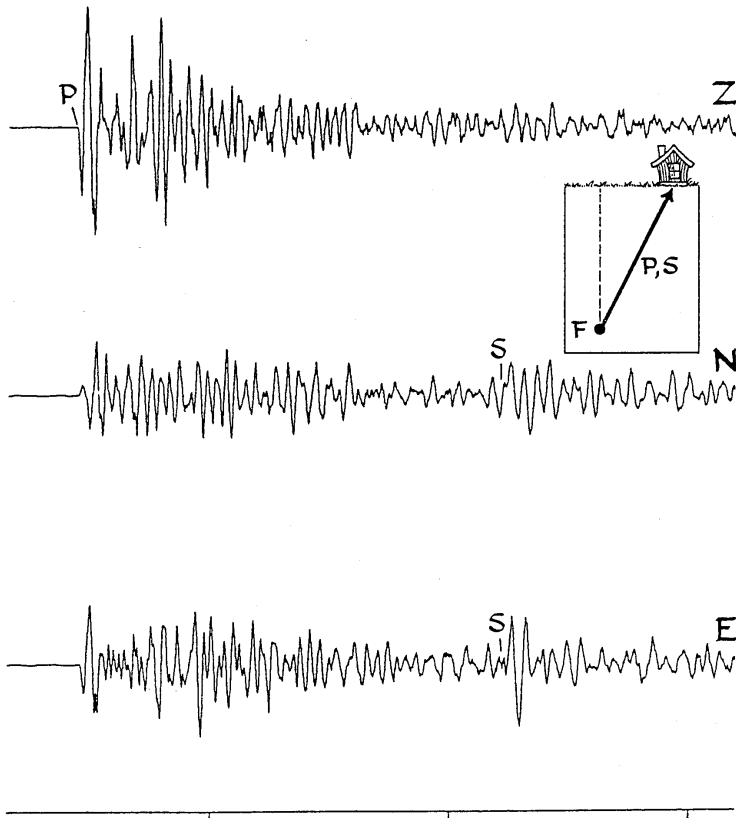


Plate 9. Short-period seismograms from a deep-focus earthquake on November 16, 1985, west of Noto peninsula, Japan, made at the Matsushiro station at an epicentral distance of 157 km. Since the focal depth of this event is 308 km, the direct waves are incoming almost vertically (see the inset). For an event of this focal depth, one expects rather simple impulsive *P* and *S* waves on the seismograms. The *P* arrival is quite distinct on all three components while the *S* onset is best seen on the E-W component. There is 20 s between successive time marks at the bottom of the plate.

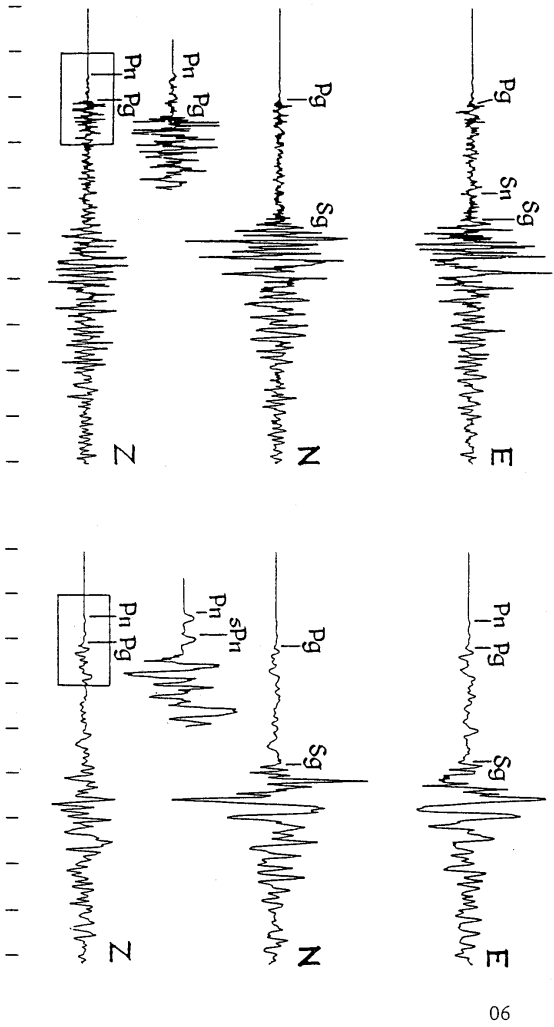


Plate 10. Velocity (left) and displacement seismograms (right) of the Swedish Jura, southern ERG, earthquake of September 3, 1978 ($M_s=5.9$). A three-component broad-band recording system at GRT, Bayern, FRG, at an epicentral distance of 220 km, has been used. All four essential crustal phases, i.e. P_n , P_g , S_n and S_g can be identified on the records, even though the S_n onset is somewhat ambiguous. S_g is best seen on the horizontal channels. The enlarged segment of the initial portion of the vertical-component displacement record (framed) shows a clear "one-sided" onset between P_n and P_g , arriving 2.6 s after P_n . By making use of synthetic (computed) seismograms, this phase has been interpreted (Kind, 1979) as sP_n (see Fig. 11). The successful revelation of the sP_n phase made it possible to determine the focal depth of the event to be about 6 km. As follows from the displayed records the velocity seismograms enhance the high frequencies and thus are useful in precise readings of the onset (arrival) times. The displacement seismograms, on the other hand, emphasize the low frequencies and are suitable for determination of dynamic source parameters, for displaying the low-frequency surface waves, etc. There is 10 s between successive time marks at the bottom of the plate.

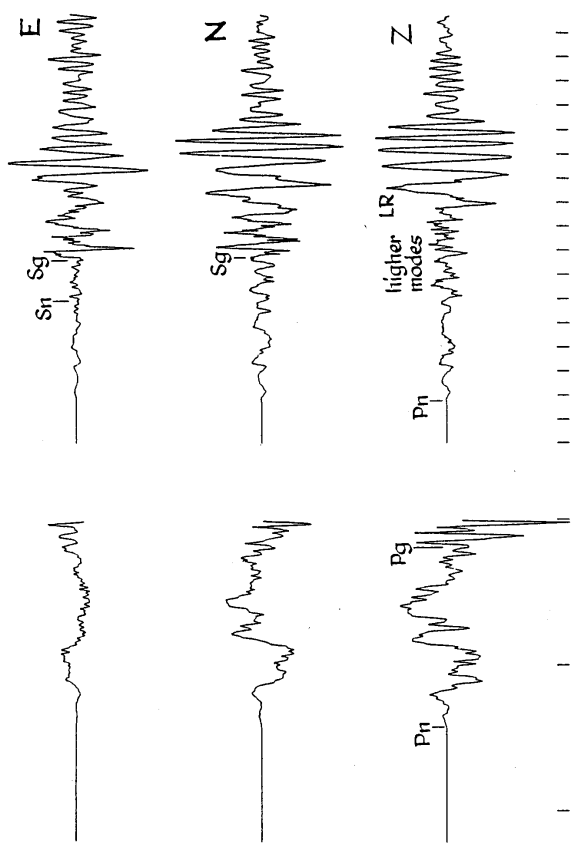


Plate 12. The disastrous Friuli, northern Italy, earthquake of September 15, 1976 ($m=5.4$), recorded by a three-component broad-band system at GRF, Bayem, FRG, at an epicentral distance of 400 km. Segments of velocity seismograms (left) and complete displacement seismograms (right) are displayed. Three clear onsets corresponding to P_n , P_g (vertical-component, velocity record) and S_g (horizontal-components, displacement records) are visible on the exhibited records. Observe the dominant, fundamental mode, LR wave with a distinct dispersion, in the period interval from about 15 to 5 s, best developed on the vertical-component channel. The short-period oscillations preceding LR belong to the higher mode Rayleigh waves. The dominant surface wave is a strong indication of a shallow event. Researchers still disagree on the more precise focal depth of this shock. Reported estimates vary from 5 km to more deeper parts of the crust. There is 10 s between successive time marks at the bottom of the plate (note, there are different time scales for the velocity and displacement traces).

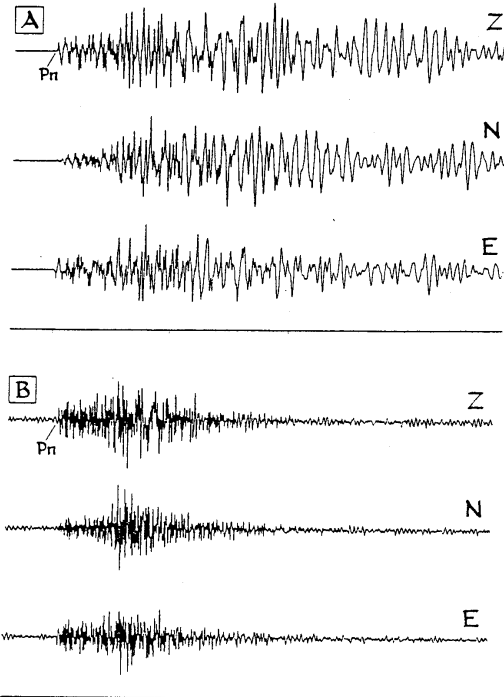


Plate 13. Short-period three-component records from two earthquakes (A and B) east of Honshu, Japan, demonstrating the influence of the source mechanism. Source parameters of the two shocks which both took place in the subduction zone at a depth of 35 km are the following:

Event	Date	M_L	Epicentral coordinates		Focal depth	Epicentral distance
A	June 8, 1986	5.4	36.53°N	142.96°E	35 km	426 km
B	April 20, 1985	4.9	37.41°N	142.77°E	35 km	417 km

The recording site is in both cases the Matsushiro station, Japan. The first onset, probably P_n , is clearly seen on records from both earthquakes, but otherwise the two cases are quite different. Observe that the top three traces (event A) are dominated by relatively low frequencies while the three bottom traces (event B) consist of waves with rather high frequencies. Due to the proximity of the two hypocenters the effect of different travel paths can be disregarded and the striking variation in the frequency content is then ascribed to different source mechanisms. Arrivals of S_n and S_g are expected 45-55 s behind P_n . There are 2 minutes between successive time marks.

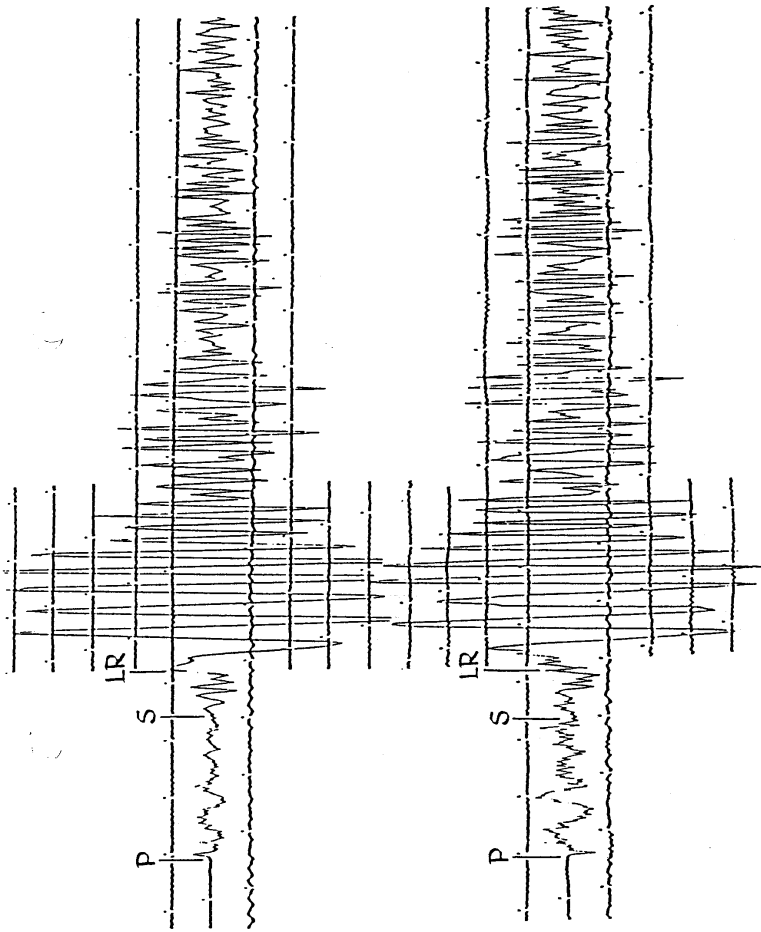


FIG. 23. Long-period records of the September 19, 1979 earthquake in Umbria, Italy ($M_s=5.9$, $h=16$ km), made at Tolosa, Spain at an epicentral distance of 13.2° . Vertical and E-W components are shown and are displayed. Distinct P and S onsets are seen on the seismograms. The large amplitudes of the LR wave train exhibit very clear dispersion. Higher modes are not visible, most likely due to a mixed continental and oceanic travel path and to complicated crustal structure.

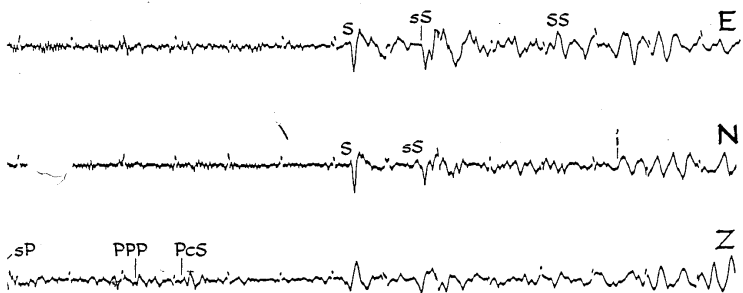
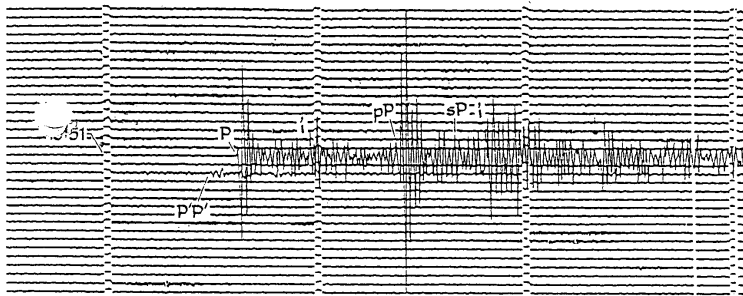


Plate 43. Short-period (uppermost trace) and long-period (lower three traces) seismograms from an earthquake in the Afghanistan-USSR border region ($m=5.9$, $M=209$ km) on September 12, 1983 made at Toledo, Spain, at a distance of 37.5°. This is an interesting example of a deep-focus, medium-size event. First characteristics to be noted are the absence of surface waves and large amplitudes of P on the short-period record. It is also interesting that pP is larger than P , most likely due to the orientation of the source. A number of body-wave arrivals are displayed on the records. The arrival 24 s after P can be explained as a reflection PpP in the upper mantle. The onset following sP has not been identified. Note $P'P'$ two traces below P (about 30 min later). On long-period records, P phases appear as sharp pulses with a rather short or non-existent coda. Very clear S and sS are exhibited on all three components.

Topic	Earthquake location
compiled by	Jens Havskov, University of Bergen, Institute of Solid Earth Physics, Allégaten 41, N-5007 Bergen, Fax: +47 55 589669, E-mail: jens@ifjf.uib.no Peter Bormann, GeoForschungszentrum Potsdam, Telegrafenberg, D- 14473 Potsdam, Germany; Fax: +49 331 288 1204; E-mail: course@gfz-potsdam.de Johannes Schweitzer, NORSAR, P.O.Box 53, N-2027 Kjeller, Fax: +47 63818719, E-mail: johannes.schweitzer@norsar.no
Version	May, 2002

1 Introduction

The exact location of a source, radiating seismic energy, is one of most important tasks in practical seismology and most seismologists have been from time to time involved in this task. The intention with this document is to describe the most common location methods without going into the mathematical details, which have been described in numerous textbooks and scientific, but to give some practical advice on earthquake location.

The earthquake location is defined by the earthquake hypocenter (x_0, y_0, z_0) and the origin time t_0 . The hypocenter is the physical location, usually given in longitude (x_0), latitude (y_0), and depth below the surface (z_0 [km]). For simplicity, the hypocenter will be labeled x_0, y_0, z_0 with the understanding that it can be either measured in geographical or Cartesian coordinates, i.e., in [deg] or [km], respectively. The origin time is the start time of the earthquake rupture. The epicenter is the projection of the earthquake location on the Earth's surface (x_0, y_0) . When the earthquake is large, the physical dimension can be several hundred kilometers and the hypocenter can in principle be located anywhere on the rupture surface. Since the hypocenter and origin time are determined by arrival times of seismic phases initiated by the first rupture, the computed location will correspond to the point where the rupture initiated and the origin time to the time of the initial rupture. This is also true using any P- or S-phases since the rupture velocity is smaller than the S-wave velocity so that P- or S-wave energy emitted from the end of a long rupture will always arrive later than energy radiated from the beginning of the rupture. Standard earthquake catalogs (such as from the International Seismological Center, ISC) report location based primarily on arrival times of high frequency P-waves. This location can be quite different from the centroid time and location obtained by moment tensor inversion of long period waves. The centroid location represents the average time and location for the entire energy radiation of the event.

2 Single station location

In general, epicenters are determined using many arrival times from different seismic stations and phases. However, it is also possible to locate an earthquake using a single 3-component station. Since the P-waves are vertically and radially polarized, the vector of P-wave motion can be used to calculate the backazimuth to the epicenter (see Figure 1). The radial component of P will be recorded on the 2 horizontal seismometers **N**(orth) and **S**(outh) and the ratio of the amplitudes A_E/A_N on the horizontal components can be used to calculate the backazimuth of arrival **AZI**:

$$AZI = \arctan A_E/A_N \quad (1)$$

There is then an ambiguity of 180° since the first polarity can be up or down so the polarity must also be used in order to get the correct backazimuth. If the first motion on vertical component of the P is upward, (which corresponds by definition to a compressional first motion (FM) arriving at the station related to an outward directed motion at the source) then the radial component of P is directed away from the hypocenter. The opposite is true if the P-polarity is negative (see also Figure 1 in Exercise EX 11.2).

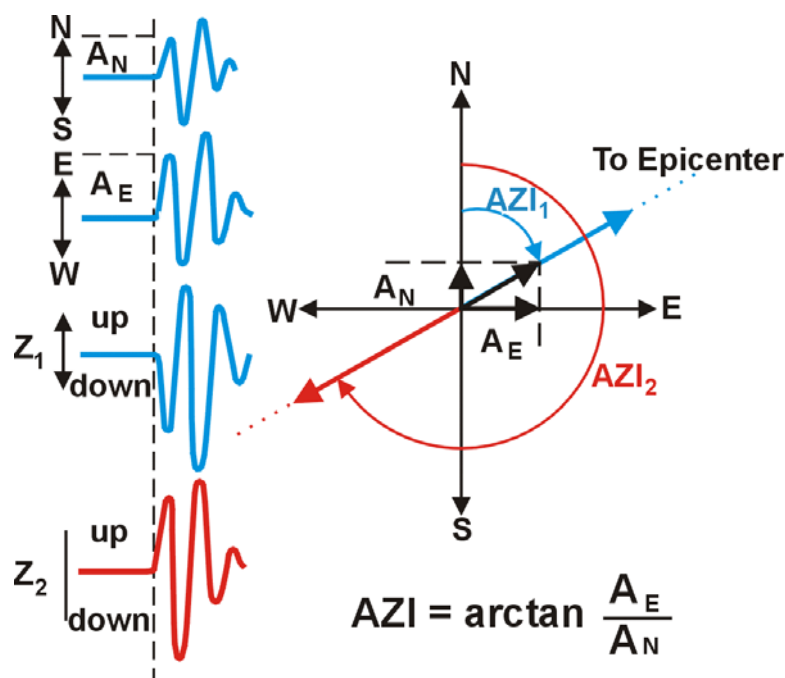


Figure 1 Example of P-wave first motions in 3-component records (left) from which the backazimuth **AZI** and incidence angle i can be derived according to Eqs. (1) and (2) (middle).

The amplitude A_Z of the Z-component can, together with the amplitude $A_R = \sqrt{(A_E^2 + A_N^2)}$ on the radial components, also be used to calculate the *apparent angle of incidence* $i_{app} = \arctan A_R / A_Z$ of a P-wave. However, according already to Wiechert (1907) the true incidence angle i_{true} of a P-wave is

$$i_{\text{true}} = \arcsin \left(\frac{v_p}{v_s} \times \sin 0.5i_{\text{app}} \right), \quad (2)$$

with the difference accounting for the amplitude distortion due to the reflection at the free surface. Knowing the incidence angle i and the local seismic velocity v_c below the observing station, we can calculate the apparent velocity v_{app} of this seismic phase with

$$v_{\text{app}} = \frac{v_c}{\sin i} \quad (3)$$

With high frequency data it might be difficult to manually read the amplitudes of the first break or sometimes the first P-swings are emergent. Since the amplitude ratio between the components should remain constant not only for the first swing of the P-phase but also for the following oscillations of the same phase, we can, with digital data, use the predicted coherence method (Roberts et al., 1989) to automatically calculate backazimuth as well as the angle of incidence. Since this is much more reliable and faster than using the manually readings of the first amplitudes, calculation of backazimuth from 3-component records of single stations has again become a routine practice (e.g., Saari, 1991). In case of seismic arrays, apparent velocity and backazimuth can be directly measured by observing the propagation of the seismic wavefront with array methods (see Chapter 9). As we shall see later, backazimuth observations are useful in restricting epicenter locations and in associating observations to a seismic event. Knowing the incidence angle and implicitly the ray parameter of an onset helps to identify the seismic phase and to calculate the epicentral distance.

With a single station we have now the direction to the seismic source. The distance can be obtained from the difference in arrival time of two phases, usually P and S. If we assume a constant velocity, and origin time t_0 , the P- and S-arrival times can then be written as

$$t_p = t_0 + D/v_p \quad t_s = t_0 + D/v_s \quad (4)$$

where t_p and t_s are the P- and S-arrival times respectively, v_p and v_s are the P- and S-velocities respectively and D is the epicentral distance (near) for surface sources and the hypocentral distance for deeper sources. By eliminating t_0 from Eq. (4), the distance can be calculated as

$$D = (t_s - t_p) \frac{v_p \cdot v_s}{v_p - v_s} \quad (5)$$

with D in km and $t_s - t_p$ in seconds. But Eq. (5) is applicable only for the travel-time difference between Sg and Pg, i.e., the direct crustal phases of S and P, respectively. They are first onsets of the P- and S-wave groups of local events only for distances up to about 100 – 250 km, depending on crustal thickness and source depth within the crust. Beyond these distances the Pn and Sn, either head waves critically refracted at the Mohorovičić discontinuity or waves diving as body waves in the uppermost part of the upper mantle become the first onsets (see Fig. 7). The “cross-over” distance x_{co} between Pn and Pg (or Pb) can be approximately calculated for a (near) surface focus from the relationship

$$x_{\text{co}} = 2 z_m \left\{ (v_m - \bar{v}_p) (v_m + \bar{v}_p) \right\}^{-1/2}, \quad (6)$$

with \bar{v}_p – average crustal P-velocity, v_m – sub-Moho P-velocity, and z_m – crustal thickness. Inserting the rough average values of $v_c = 6$ km/s and $v_m = 8$ km/s we get, as a “rule of thumb”, $x_{co} \approx 5 z_m$. At smaller distances we can be rather sure that the observed first arrival is Pg. Note, however, that this “rule of thumb” is valid for surface focus only. As demonstrated with Fig. 2.40 in Chapter 2, the crossover distance is only about half as large for near Moho earthquakes and also the dip of the Moho and the direction of observation (up- or downdip) does play a role. However, in continental (intraplate) environment, lower crustal earthquakes are rare. Mostly they occur in the upper crust.

Examples for calculating the epicentral distance D and the origin time OT of near seismic events by means of a set of local travel-time curves for Pn, Pg, Sn, Sg and Lg are given in exercise EX 11.1. In the absence of local travel-time curves for the area under consideration one can use Eq. (5) for deriving a “**rule of thumb**” for approximate distance determinations from travel-time differences Sg-Pg. For an ideal Poisson solid $v_s = v_p/\sqrt{3}$. This is a good approximation for the average conditions in the Earth crust: With this follows from Eq. (5) : $D = (t_{Sg} - t_{Pg}) \times 8.0$ for “normal, medium age” crustal conditions with $\bar{v}_p = 5.9$ km/s, and $D = (t_{Sg} - t_{Pg}) \times 9.0$ for old Precambrian continental shields with rather large $\bar{v}_p = 6.6$ km/s. However, if known, the locally correct v_p/v_s ratio should be used to improve this “rule of thumb”. If the distance is calculated from the travel-time difference between Sn and Pn another good rule of thumb is $D = (t_{Sn} - t_{Pn}) \times 10$. It may be applicable up to about 1000 km distance.

For distances between about $20^\circ < \Delta < 100^\circ$ the relationship $\Delta^\circ = \{(t_s - t_p)_{\min} - 2\} \times 10$ still yields reasonably good results with errors $< 3^\circ$, however, beyond $D = 10^\circ$ the use of readily available global travel-time tables such as IASP91 (Kennett and Engdahl, 1991; Kennett, 1991), SP6 (Morelli and Dziewonski, 1993), or AK135 (Kennett et al., 1995) is strongly recommended for calculating the distance.

With both backazimuth and distance, the epicenter can be obtained by measuring off the distance along the backazimuth of approach. Finally, knowing the distance, we can calculate the P-travel time and thereby get the origin time using the P-arrival time (see Exercise EX 11.2: Manual localization of teleseismic events by means of 3-component records).

3 Multiple station location

3.1 Manual location

When at least 3 stations are available, a simple manual location can be made from drawing circles (the circle method) with the center at the station locations and the radii equal to the epicentral distances calculated from the S-P times (Figure 2).

These circles will rarely cross in one point which indicates errors in the observations and/or that we have wrongly assumed a surface focus. In fact, $t_s - t_p$ is the travel-time difference for the hypocentral distance d which is for earthquakes with $z > 0$ km generally larger than the epicentral distance Δ (or D). Therefore, the circles drawn around the stations with radius d will normally not be crossing in a single point at the epicenter but rather “overshoot”. One should therefore fix the epicenter either in the “center of gravity” of the overshoot area (black area in Figure 2) or draw “chords”, i.e., straight lines passing through the crossing point

between two neighboring circles. These chord lines intersect in the epicenter (see Figure 1 in Exercise EX 11.1). Still other methods exist (e.g., Båth, 1979) to deal with this depth problem (e.g., the hyperbola method which uses P-wave first arrivals only and assumes a constant P-wave velocity), however since they are rarely used, they will not be discussed here.

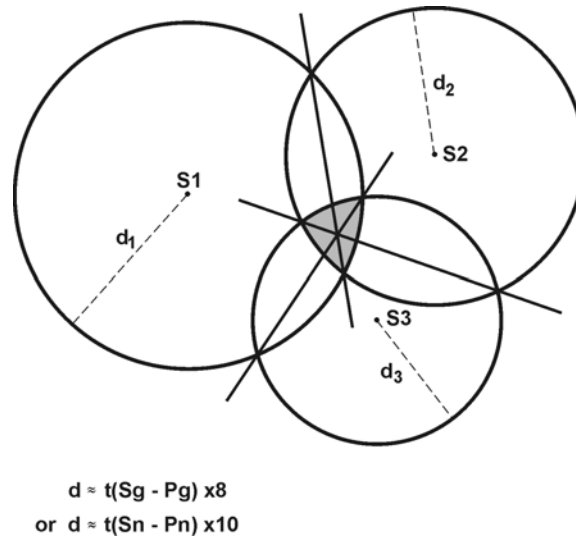


Figure 2 Location by the “circle and chord” method. The stations are located in S1, S2 and S3. The epicenter is found within the shaded area where the circles overlap. The best estimate is the crossing of the chords, which connect the crossing points of the different pairs of circles.

With several stations available from a local earthquake, the origin time can be determined by a very simple technique called a Wadati diagram (Wadati, 1933). Using Eq. (7) and eliminating Δ , the S-P travel-time difference can be calculated as

$$t_s - t_p = (v_p/v_s - 1) \times (t_p - t_0) \quad (7)$$

The S-P times are plotted against the absolute P-time. Since $t_s - t_p$ goes to zero at the hypocenter, a straight line fit on the Wadati diagram (Figure 3) gives the origin time at the intercept with the P-arrival axis and from the slope of the curve, we get v_p/v_s . Note that it is thus possible to get a determination of both the origin time and a mean v_p/v_s ratio without any prior knowledge of the crustal structure, the only assumption is that v_p/v_s is constant and that the P- and S-phases are of the same type like Pg and Sg or Pn and Sn. Such an independent determination of these parameters can be very useful when using other methods of earthquake location.

The Wadati diagram can also be very useful in making independent checks of the observed arrival times. Any points not fitting the linear relationship might be badly identified, either by not being of the same phase type or by misreading.

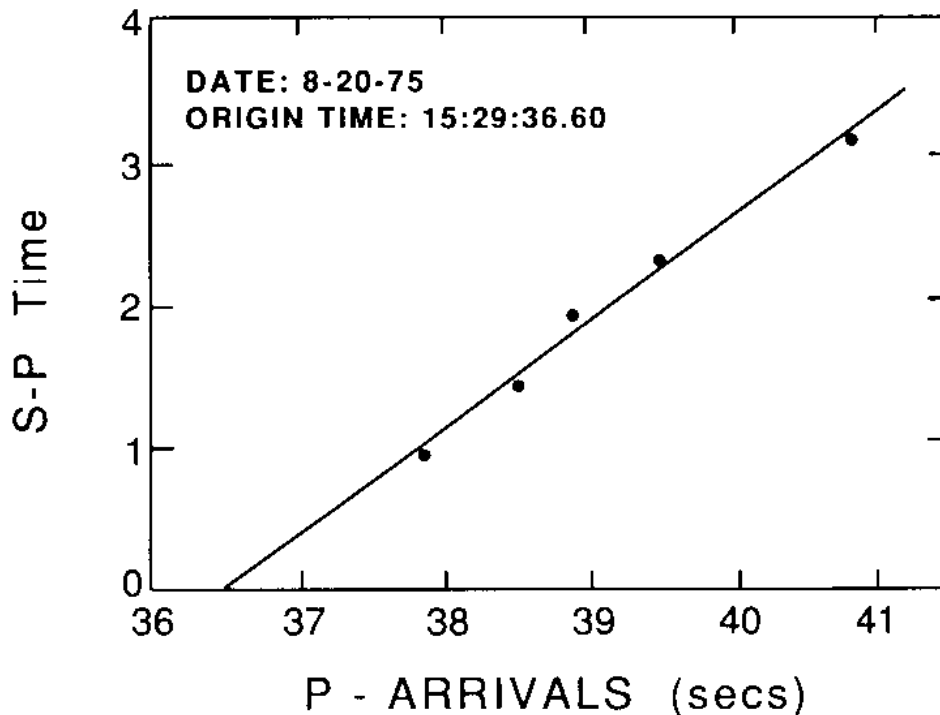


Figure 3 An example of a Wadati diagram. The intercept on the x-axis gives the origin time. The slope of the line is 0.72 so the v_p/v_s ratio is 1.72. Note that the points do not exactly fit the line, indicating model and/or data reading errors (from Lay and Wallace, 1995).

3.2 Computer location

Manual location methods provide insight into the location problems, however in practice we use computer methods. In the following, the most common ways of calculating hypocenter and origin time by computer will be discussed.

The calculated arrival time t_i^c at station i can be written as

$$t_i^c = T(x_i, y_i, z_i, x_0, y_0, z_0) + t_0 \quad (8)$$

where T is the travel time as a function of the location of the station (x_i, y_i, z_i) and the hypocenter. This equation has 4 unknowns, so in principle 4 arrival time observations from at least 3 stations are needed in order to determine the hypocenter and origin time. If we have n observations, there will be n equations of the above type and the system is over determined and has to be solved in such a way that the misfit or residual r_i at each station is minimized. r_i is defined as the difference between the observed and calculated travel times

$$r_i = t_i^o - t_i^c. \quad (9)$$

In principle, the problem seems quite simple. However, since the travel-time function T is a nonlinear function of the model parameters, it is not possible to solve Eq. (8) with any analytical methods. So even though T can be quite simple calculated, particularly when using

a 1D Earth model or pre-calculated travel-time tables, the non-linearity of T greatly complicates the task of inverting for the best hypocentral parameters. The non-linearity is evident even in a simple 2D epicenter determination where the travel time t_i from the point (x, y) to a station (x_i, y_i) can be calculated as

$$t_i = \frac{\sqrt{(x - x_i)^2 + (y - y_i)^2}}{v}, \quad (10)$$

where v is the velocity. It is obvious that t_i does not scale linearly with either x and y so it is not possible to use any set of linear equations to solve the problem and standard linear methods cannot be used. This means that given a set of arrival times, there is no simple way of finding the best solution. In the following, some of the methods of solving this problem will be discussed.

3.2.1 Grid search

Since it is so simple to calculate the travel times of all seismic phases to any point in the model, given enough computer power, a very simple method is to perform a grid search over all possible locations and origin times and compute the arrival time at each station (e.g., Sambridge and Kennett, 1986). The hypocentral location and origin time would then be the point with the best agreement between the observed and calculated times. This means that some measure of best agreement is needed, particularly if many observations are used. The most common approach is least squares which is to find the minimum of the sum of the squared residuals e from the n observations:

$$e = \sum_{i=1}^n (r_i)^2 \quad (11)$$

The root mean squared residual RMS , is defined as $\sqrt{e/n}$. RMS is given in almost all location programs and commonly used a guide to location precision. If the residuals are of similar size, the RMS gives the approximate average residual. As will be seen later, RMS only gives an indication of the fit of the data, and a low RMS does not automatically mean an accurate hypocenter determination. Generally, the precision of the computational solution, which is based on various model assumptions, should not be mistaken as real accuracy of the location and origin time. This point will be discussed later under section 7.

The average squared residual e/n is called the variance of the data. Formally, n should here be the number of degrees of freedom ndf , which is the number of observations minus the number of parameters in fit (here 4). Since n usually is large, it can be considered equal to the number of degrees of freedom. This also means that \mathbf{RMS}^2 is approximately the same as the variance. The least squares approach is the most common measure of misfit since it leads to simple forms of the equations in the minimization problems (see later). It also works quite well if the residuals are caused by uncorrelated Gaussian noise. However in real problems this is often not the case. A particularly nasty problem is the existence of outliers, i.e., individual large residuals. A residual of 4 will contribute 16 times more to the misfit e , than a residual of 1. Using the sum of the absolute residuals as a norm for the misfit can partly solve this problem:

$$e1 = \sum_{i=1}^n |r_i|. \quad (12)$$

This is called the L1 norm and is considered more robust when there are large outliers in the data. It is not much used in standard location programs since the absolute sign creates complications in the equations. This is of course not the case for grid search. Therefore, most location programs will have some scheme for weighting out or truncating large residuals (see later), which can partly solve the problem.

Once the misfits (e.g., *RMS*) have been calculated at all grid points, one could assign the point with the lowest *RMS* as the ‘solution’. For well-behaved data, this would obviously be the case, but with real data, there might be several points, even far apart, with similar *RMS* and the next step is therefore to estimate the probable uncertainties of the solution. The simplest way to get an indication of the uncertainty, is to contour the *RMS* as a function of *x* and *y* (2D case) in the vicinity of the point with the lowest *RMS* (Figure 4).

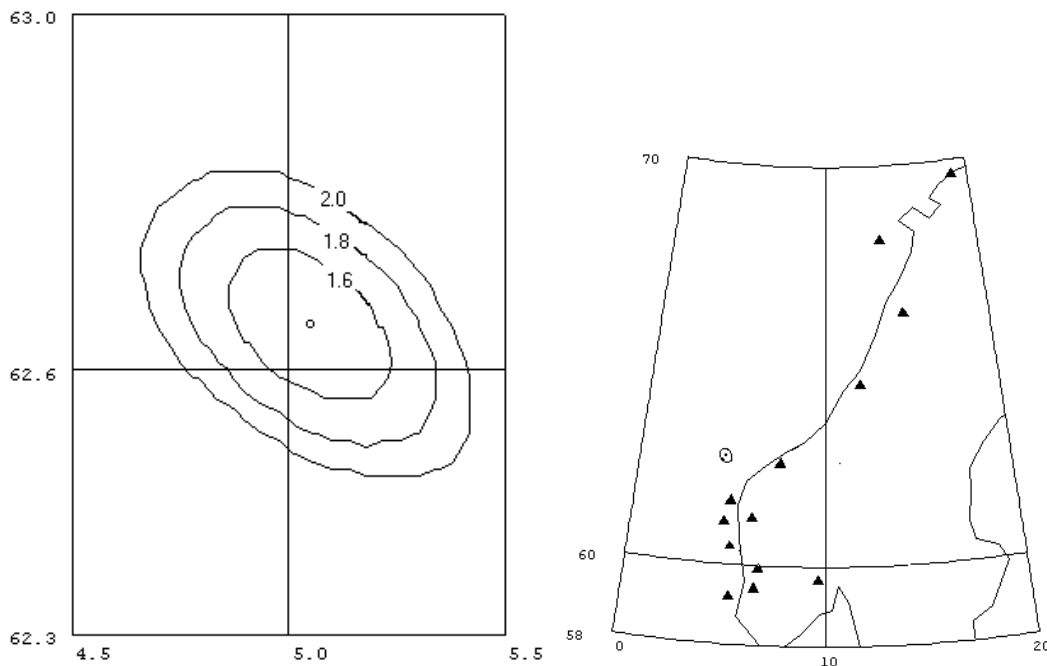


Figure 4 Left: *RMS* contours (in seconds) from a grid search location of an earthquake off western Norway (left). The grid size is 2 km. The circle in the middle indicates the point with the lowest *RMS* (1.4 s). Right: The location of the earthquake and the stations used. Note the elongated geometry of the station distribution. Its effect on the error distribution will be discussed under 4.1. The *RMS* ellipse from the figure on the left is shown as a small ellipse in the figure at right. Latitudes are degrees North and longitudes degrees East.

Clearly, if *RMS* is growing rapidly when moving away from the minimum, a better solution has been obtained than if *RMS* grows slowly. If *RMS* is contoured in the whole search area, other minima of similar size might be found indicating not only large errors but also a serious ambiguity in the solution. Also note in Fig. 4 that networks with irregular aperture have reduced distance control in the direction or their smallest aperture but good azimuth control in the direction of their largest aperture.

An important point in all grid-search routines is the method how the possible model space is searched through. In particular for events observed at teleseismic distances the model space can be very large. Sambridge and Kennett (2001) published a fast neighbourhood algorithm to use for global grid search.

3.2.2 Location by iterative methods

Despite increasing computer power, earthquake locations are mainly done by other methods than grid search. These methods are based on linearizing the problem. The first step is to make a guess of hypocenter and origin time (x_0, y_0, z_0, t_0) . In its simplest form, e.g., in case of events near or within a station network, this can be done by using a location near the station with the first arrival time and using that arrival time as t_0 . Other methods also exist (see below). In order to linearize the problem, it is now assumed that the true hypocenter is close enough to the guessed value so that travel-time residuals at the trial hypocenter are a linear function of the correction we have to make in hypocentral distance.

The calculated arrival times at station i , t_i^c from the trial location are, as given in Eq. (8), $t_i^c = T(x_0, y_0, z_0, x_i, y_i, z_i) + t_0$ and the travel-time residuals r_i are $r_i = t_i^o - t_i^c$. We now assume that these residuals are due to the error in the trial solution and the corrections needed to make them zero are Δx , Δy , Δz , and Δt . If the corrections are small, we can calculate the corresponding corrections in travel times by approximating the travel time function by a Taylor series and only using the first term. The residual can now be written:

$$r_i = (\partial T / \partial x_i) * \Delta x + (\partial T / \partial y_i) * \Delta y + (\partial T / \partial z_i) * \Delta z + \Delta t \quad (13)$$

In matrix form we can write this as

$$\mathbf{r} = \mathbf{G} * \mathbf{X}, \quad (14)$$

where \mathbf{r} is the residual vector, \mathbf{G} the matrix of partial derivatives (with 1 in the last column corresponding to the source time correction term) and \mathbf{X} is the unknown correction vector in location and origin time.

This is a set of linear equations with 4 unknowns (corrections to hypocenter and origin time), and there is one equation for each observed phase time. Normally there would be many more equations than unknowns (e.g., 4 stations with 3 phases each would give 12 equations). The best solution to Eq. (13) or Eq. (14) is usually obtained with standard least squares techniques. The original trial solution is then corrected with the results of Eq. (13) or Eq. (14) and this new solution can then be used as trial solution for a next iteration. This iteration process can be continued until a predefined breakpoint is reached. Breakpoint conditions can be either a minimum residuum r , a last iteration gives smaller hypocentral parameter changes than a predefined limit, or just the total number of iterations. This inversion method was first invented and applied by Geiger (1910) and is called the Geiger method of earthquake location. The iterative process usually converges rapidly unless the data are badly configured or the initial guess is very far away from the mathematically best solution (see later). However, it also happens that the solution converges to a local minimum and this would be hard to detect in the output unless the residuals are very bad. A test with a grid search program could tell if the minimum is local or tests could be made with several start locations.

So far we have only dealt with observations in terms of arrival times. Many 3-component stations and arrays now routinely report backazimuth of arrival ϕ . It is then possible to locate events with only one station and P- and S-times (see Fig. 1). However, the depth must be fixed. If one or several backazimuth observations are available, they can be used together with the arrival time observations in the inversion and the additional equations for the backazimuth residual are

$$r_i^\phi = (\partial\phi/\partial x_i) * \Delta x + (\partial\phi/\partial y_i) * \Delta y \quad (15)$$

Equations of this type are then added to the Eq. (13) or Eq. (14). The Δx and Δy in Eq. (15) are the same as for Eq. (13), however the residuals are now in degrees. In order to make an overall *RMS*, the degrees must be ‘converted to seconds’ in terms of scaling. For example, in the location program Hypocenter (Lienert and Havskov, 1995), a 10 deg backazimuth residual was optionally made equivalent to 1 s travel time residual. Using e.g., 20 deg as equivalent to 1 s would lower the weight of the backazimuth observations. Schweitzer (2001) used in the location program HYPOSAT a different approach. In this program the measured (or assumed) observation errors of the input parameters are used to weight individually the different lines of the equation system (13) or (14) before inverting it. Thereby, more uncertain observations will contribute much less to the solution than well-constrained ones and all equations become non-dimensional.

Arrays (see Chapter 9) or single stations (see Eq. (3)) cannot only measure the backazimuth of a seismic phase but also its ray parameter (or apparent velocity). Consequently, the equation system (13) or (14) to be solved for locating an event, can also be extended by utilizing such observed ray parameters p (or apparent velocities) as defining data. In this case we have can write

$$r_i^p = (\partial p/\partial x_i) * \Delta x + (\partial p/\partial y_i) * \Delta y + (\partial p/\partial z_i) * \Delta z \quad (16)$$

Eq. (16) is independent from the source time and the partial derivatives are often very small. However, in some cases, in particular if an event is observed with only one seismic array, the observed ray parameter will give additional constrain for the event location.

Eqs. (13) and (14) are written without discussing whether working with a flat Earth or a spherical Earth. However, the principle is exactly the same and using a flat-Earth transformation (e.g., Müller, 1977) any radially symmetric Earth model can be transformed in a flat model. The travel times and partial derivatives are often calculated by interpolating in tables and in principle it is possible to use any Earth model including 2D and 3D models to calculate theoretical travel times. In practice, 1D models are mostly used, since 2D and 3D models are normally not well enough known and the travel-time computations are much more time consuming. For local seismology, it is a common practice to specify a 1D crustal model and calculate arrival times for each ray while for global models; an interpolation in travel-time tables such as IASPEI91 is the most common. However, as Kennett and Engdahl (1991) pointed out, the preferred and much more precise method for obtaining travel times from the IASP91 model or other 1D global Earth models (see Data Sheet DS 2.1) is to apply the tau-p method developed by Buland and Chapman (1983). To calculate own travel-time tables for local or global Earth models, the computer program LAUFZE can be downloaded from <ftp://ftp.norsar.no/pub/outgoing/johannes/lauf/>. It allows calculating travel times for many different seismic phases and an arbitrary horizontally layered model with any combination of layers with constant velocities, gradients, or first-order discontinuities.

3.2.3 Example of location in a homogeneous model

The simplest case for earthquake location is a homogeneous medium. The travel times can be calculated as

$$T_i = \frac{\sqrt{(x - x_i)^2 + (y - y_i)^2 + (z - z_i)^2}}{v} + t_0, \quad (17)$$

where v is the velocity. The partial derivatives can be estimated from Eq. (17) and e.g., for x , the derivative is

$$\frac{\partial T_i}{\partial x} = \frac{(x - x_i)}{v} * \frac{1}{\sqrt{(x - x_i)^2 + (y - y_i)^2 + z^2}}. \quad (18)$$

Similar expressions can be made for y and z . Table 1 gives an example of locating an earthquake with 10 stations in a model with constant velocity (from Stein, 1991). The stations are from 11 to 50 km from the hypocenter. The earthquake has an origin time of 0 s at the point (0, 0, 10) km. The starting location is at (3, 4, 20) km at 2 s. The exact travel times were calculated using a velocity of 5 km/s and the iterations were done as indicated above. At the initial guess, the sum of the squared residuals were 92.4 s², after the first iteration it was reduced to 0.6 s² and already at the second iteration, the ‘correct’ solution was obtained. This is hardly surprising, since the data had no errors. We shall later see how this works in the presence of errors.

Table 1 Inversion of error free data. Hypocenter is the correct location, Start is the start location, and the location is shown for the two following iterations. Units for x , y and z are [km], for t_0 [s] and for the misfit e according to Eq. (11) [s²].

	Hypocenter	Start	1. Iteration	2. Iteration
X	0.0	3.0	-0.5	0.0
Y	0.0	4.0	-0.6	0.0
Z	10.0	20.0	10.1	10.0
t_0	0.0	2.0	0.2	0.0
e		94.2	0.6	0.0
RMS		3.1	0.25	0.0

3.2.4 Advanced methods

The problem of locating seismic events has recently experienced a lot of attention and new procedures have been developed such as the double-difference earthquake location algorithm (Waldhauser and Ellsworth, 2000), a novel global differential evolution algorithm (Ružek and Kvasnička (2001), a probabilistic approach to earthquake location in 3D and layered models by Lomax et al. (2000) as well as advanced grid search procedures to be applied in highly heterogeneous media (Lomax et al., 2001). Recent advances in travel-time calculations for three-dimensional structures complements this method (e.g., Thurber and Kissling, 2000). Several of these and more most recent developments are summarized in a monograph edited

by Thurber and Rabinowitz (2000), including also advances in global seismic event location (Thurber and Engdahl, 2000) and in a special volume about event location in context with the special requirements for monitoring the CTBT (Ringdal and Kennett, 2001). An example how much the accuracy of location within earthquake clusters can be improved by applying the above mentioned double-difference earthquake location algorithm is given in Figure 5.

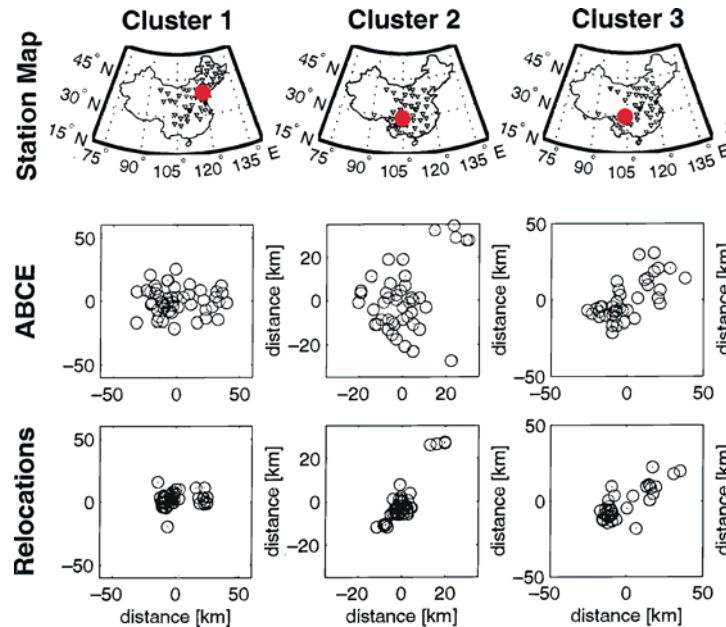


Figure 5 Examples of improving the ABCE locations for earthquake clusters (red dots) from regional networks of seismic stations (triangles) in China by relocating the events with the double-difference location algorithm (courtesy of Paul G. Richards).

4 Location errors

4.1 Error quantification and statistics

Since earthquakes are located with arrival times that contain observational errors and the travel times are calculated assuming we know the model, all hypocenters will have errors. Contouring the grid search *RMS* (Figure 4) gives an indication of the uncertainty of the epicenter. Likewise it would be possible to make 3D contours to get an indication of the 3D uncertainty. The question is now how to quantify this measure. The *RMS* of the final solution is very often used as a criterion for ‘goodness of fit’. Although it can be an indication, *RMS* depends on the number of stations and does not in itself give any indication of errors and *RMS* is not reported by e.g., PDE and ISC.

From Figure 4 it is seen that the contours of equal *RMS* are not circles. We can calculate contours within which there is a 67 % probability (or any other desired probability) of finding the epicenter (see below). We call this the error ellipse. This is the way hypocenter errors normally are represented. It is therefore not sufficient to give one number for the hypocenter error since it varies spatially. Standard catalogs from PDE and ISC give the errors in latitude, longitude and depth, however, that can also be very misleading unless the error ellipse has the minor and major axis NS or EW. In the example in Figure 4, this is not the case. Thus the only proper way to report error is to give the full specification of the error ellipsoid.

Before going into a slightly more formal discussion of errors, let us try to get a feeling what elements affect the shape and size of the epicentral error ellipse. If we have no arrival time errors, there are no epicenter errors so the magnitude of the error (size of error ellipse) must be related to the arrival time uncertainties. If we assume that all arrival time reading errors are equal, only the size and not the shape of the error ellipse can be affected. So what would we expect to give the shape of the error ellipse? Figure 4 is an example of an elongated network with the epicenter off to one side. It is clear that in the NE direction, there is a good control of the epicenter since S-P times control the distances in this direction due to the elongation of the network. In the NW direction, the control is poor because of the small aperture of the network in this direction. We would therefore expect an error ellipse with the major axis NW as observed. Another way of understanding why the error is larger in NW than in NE direction is to look at Eq. (12). The partial derivatives $\partial T/\partial x$ will be much smaller than $\partial T/\partial y$ so the Δy -terms will have larger weight than the Δx -terms in the equations (strictly speaking the partial derivatives with respect to NW and NE). Consequently, errors in arrival times will affect Δx more than Δy . Note, that if backazimuth observations were available for any of the stations far North or South of the event, this would drastically reduce the error estimate in the EW direction since $\partial\phi/\partial x$ is large while $\partial\phi/\partial y$ is nearly zero.

Another geometry of the stations would give another shape of the error ellipse. It is thus possible for any network to predict the shape and orientation of the error ellipses, and given an arrival error, also the size of the ellipse for any desired epicenter location. This could e.g., be used to predict how a change in network configuration would affect earthquake locations at a given site.

In all these discussions, it has been assumed that the errors have Gaussian distribution and that there are no systematic errors like clock error. It is also assumed that there are no errors in the theoretical travel times, backazimuths, or ray parameter calculations due to unknown structures. This is of course not true in real life, however error calculations become too difficult if we do not assume a simple error distribution and that all stations have the same arrival time error.

The previous discussion gave a qualitative description of the errors. We will now show how to calculate the actual hypocentral errors from the errors in the arrival times and the network configuration. The most common approach to earthquake location is based the least squares inversion and a Gaussian distribution of the arrival time errors in which case the statistics is well understood and we can use the Chi-Square probability density distribution to calculate errors. For a particular earthquake location, χ^2 can be calculated as:

$$\chi^2 = \frac{1}{\sigma^2} \sum_{i=1}^n r_i^2, \quad (19)$$

where σ is the assumed same standard deviation of any one of the residuals and n is the number of observations. We can now look in standard statistical tables (extract in Table 2) to find the expected value of χ^2 within a given probability. As it can be seen from the table, within 5% probability, χ^2 is approximately the number of degrees of freedom (*ndf*), which in our case is $n-4$.

Table 2 The percentage points of the χ^2 distribution for different number of degrees of freedom (*ndf*)

<i>ndf</i>	χ^2 (95%)	χ^2 (50%)	χ^2 (5%)
5	1.1	4.4	11.1
10	3.9	9.3	18.3
20	10.9	19.3	31.4
50	34.8	49.3	67.5
100	77.9	99.3	124.3

If e.g., an event is located with 24 stations (*ndf*=20), there is only a 5% chance that χ^2 will exceed 31.4. The value of χ^2 will grow as we move away from the best fitting epicenter and in the example above, the contour within which χ^2 is less than 31.4 will show the error ellipse within which there is 95 % chance of finding the epicenter. In practice, errors are mostly reported within 67 % probability.

The errors in the hypocenter and origin time can also formally be defined with the variance – covariance matrix σ_X^2 of the hypocentral parameters. This matrix is defined as

$$\sigma_X^2 = \begin{Bmatrix} \sigma_{xx}^2 & \sigma_{xy}^2 & \sigma_{xz}^2 & \sigma_{xt}^2 \\ \sigma_{yx}^2 & \sigma_{yy}^2 & \sigma_{yz}^2 & \sigma_{yt}^2 \\ \sigma_{zx}^2 & \sigma_{zy}^2 & \sigma_{zz}^2 & \sigma_{zt}^2 \\ \sigma_{tx}^2 & \sigma_{ty}^2 & \sigma_{tz}^2 & \sigma_{tt}^2 \end{Bmatrix}. \quad (20)$$

The diagonal elements are variances of the location parameters x , y , z and t_0 while the off diagonal elements give the coupling between the errors in the different hypocentral parameters. For more details, see e.g., Stein (1991). The nice property about σ_X^2 is that it is simple to calculate:

$$\sigma_X^2 = \sigma^2 * (\mathbf{G}^T \mathbf{G})^{-1}, \quad (21)$$

where σ^2 is the variance of the arrival times multiplied with the identity matrix and \mathbf{G}^T is \mathbf{G} transposed. The standard deviations of the hypocentral parameters are thus given by the square root of the diagonal elements and these are the usual errors reported. So how can we use the off diagonal elements? Since σ_X^2 is a symmetric matrix, a diagonal matrix in a coordinate system, which is rotated relatively to the reference system, can represent it. We now only have the errors in the hypocentral parameters, and the error ellipse simply have semi axes σ_{xx} , σ_{yy} , and σ_{zz} . The main interpretation of the off diagonal elements is thus that they define the orientation and shape of the error ellipse. A complete definition therefore requires 6 elements. Eqs. (20) and (21) also show, as earlier stated intuitively, that the shape and orientation of the error ellipse only depends on the geometry of the network and the crustal structure while the standard deviation of the observations is a scaling factor.

The critical variable in the error analysis is thus the arrival-time variances σ^2 . This value is usually larger than would be expected from timing and picking errors alone, however it might vary from case to case. Setting a fixed value for a given data set could result in unrealistic

error calculations. Most location programs will therefore estimate σ from the residuals of the best fitting hypocenter:

$$\sigma^2 = \frac{1}{ndf} \sum_{i=1}^n r_i^2. \quad (22)$$

Division by ndf rather than by n compensates for the improvement in fit resulting from the use of the arrival times from the data. However, this only partly works and some programs allow setting an a priori value, which is only used if the number of observations is small. For small networks this can be a critical parameter.

Recently, some studies (e.g., Di Giovambattista and Barba, 1997; Parolai et al., 2001) showed, both for regional and local seismic networks, that the error estimates ERH (in horizontal) and ERZ (in vertical direction), as given by routine location programs (e.g., in Hypoellipse) can not be considered as a conservative estimate of the true location error and might encourage investigators to unjustified tectonic conclusions (see also Figures 12 and 13).

4.2 Example of error calculation

We can use the previous error free example (Table 1) and add some errors (from Stein, 1991). We add Gaussian errors with a mean of zero and a standard deviation of 0.1 s to the arrival times. Now the data are inconsistent and cannot fit exactly. As it can be seen from the results in Table 3, the inversion now requires 3 iterations (2 before) before the locations do not change anymore. The final location is not exactly the location used to generate the arrival times and the deviation from the correct solution is 0.2, 0.4, and 2.2 km for x , y , and z respectively and 0.2 s for origin time. This gives an indication of the location errors.

Table 3 Inversion of arrival times with a 0.1 s standard error. Hypocenter is the correct location, Start is the start location, and the locations are shown after the three following iterations. e is the misfit according to Eq. (11).

	Hypocenter	Start	1. Iteration	2. Iteration	3. Iteration
x [km]	0.0	3.0	-0.2	0.2	0.2
y [km]	0.0	4.0	-0.9	-0.4	-0.4
z [km]	10.0	20.0	12.2	12.2	12.2
t_0 [s]	0.0	2.0	0.0	-0.2	-0.2
e [s ²]		93.7	0.33	0.04	0.04
RMS [s]		3.1	0.25	0.06	0.06

It is now interesting to compare to what is obtained with the formal error calculation. Table 4 gives the variance – covariance matrix. Taking the square root of the diagonal elements we get a standard deviation of x , y , z and t_0 of 0.3, 0.3 and 1.1 km and 0.1 s respectively. This is close to the ‘true’ error so the solution is quite acceptable. Also note that the *RMS* is close to the standard error.

Table 4 Variance – covariance matrix for the example in Table 3.

	x	Y	Z	t
x	0.06	0.01	0.01	0.00
y	0.01	0.08	-0.13	0.01
z	0.01	-0.13	1.16	-0.08
t	0.00	0.01	-0.08	0.0

The variance – covariance matrix shows some interesting features. As seen from the diagonal elements of the variance – covariance matrix, the error is much larger in the depth estimate than in x and y. This clearly reflects that the depth is less well constrained than the epicenter which is quite common unless there are stations very close to the epicenter and thus $|(d-\Delta)| / \Delta \gg 1$. We have for simplicity calculated the standard deviations from the diagonal terms, however since the off diagonal terms are not zero, the true errors are larger. In this example it can be shown that the semimajor and semiminor axis of the error ellipse have lengths of 0.29 and 0.24 km respectively and the semimajor axis trends N22°E so the difference from the original diagonal terms is small.

The zt term, the covariance between depth and origin time, is negative, indicating a negative trade-off between the focal depth and the origin time; an earlier source time can be compensated by a larger source depth and vice versa. This is commonly observed in practice and is more prone to happen if only first P-phase arrivals are used such that there is no strong limitation of the source depth by P-times in different distances.

Error calculation is a fine art, there are endless variations on how it is done and different location programs will usually give different results.

5 Relative location methods

5.1 Master event technique

The relative location between events within a certain region can often be made with a much greater accuracy than the absolute location of any of the events. This is the case when velocity variations outside the local region are the major cause of the travel-time residuals such that residuals measured at distant stations will be very similar for all of the local events. Usually, the events in the local area are relocated relative to one particularly well-located event, which is then called the **master event**. It should be clear that the Master Event Technique could only be used when the distance to the stations is much larger than the distance between the events.

Most location programs can be used for a master event location. For this travel-time anomalies outside the source region are assumed to cause all individual station residuals after the location of the master event. By using these station residuals as station corrections, the location of the remaining events will be made relative to the master event since all relative changes in arrival times are now entirely due to changes in location within the source region. It is obvious that only stations and phases for which observations are available for the master event can be used for the remaining events. Ideally, the same stations and phases should be used for all events.

5.2 Joint hypocenter location

In the Master Event Technique, it was assumed that true structure dependent residuals could be obtained absolutely correct from the master event, however other errors could be present in the readings for the master event. A better way is to determine the most precise station residuals using the whole data set. This is what Joint Hypocenter Determination (JHD) is about. Instead of determining one hypocenter and origin time, we will jointly determine m hypocenters and origin times, and n station corrections. This is done by adding the station residuals Δt_i^s to Eq. (13) and writing the equations for all m earthquakes (index j):

$$r_{ij} = (\partial T / \partial x_{ij}) * \Delta x + (\partial T / \partial y_{ij}) * \Delta y + (\partial T / \partial z_{ij}) * \Delta z + \Delta t_i^s + \Delta t_j. \quad (23)$$

The first who proposed the JHD method was Douglas (1967). Since the matrix G of Eq. (14) is now much larger than the 4×4 matrix for a single event location, efficient inversion schemes must be used. If we use e.g., 20 stations with 2 phases each for 10 events, there will be $20 * 10 * 2 = 400$ equations and 80 unknowns (10 hypocenters and origin times, and 20 station residuals).

The relative locations obtained by the Master Event Technique or the JHD are usually more reliable than individually estimated relative locations. However, only if we have the absolute location of one of the events (e.g., a known explosion), we will be able to convert the relative locations of a Master Event algorithm to absolute locations. While for JHD, “absolute” locations are obtained for all events if the assumed velocity model is correct. Accurate relative locations are useful to study e.g., the structure of a subduction zone or the geometry of an aftershocks area, which might indicate the orientation and geometry of the fault. Recently, Pujol (2000) gives a very detailed outline of the method and its application to data from local seismic networks. Figure 5 shows an example for increased location accuracy after applying JHD.

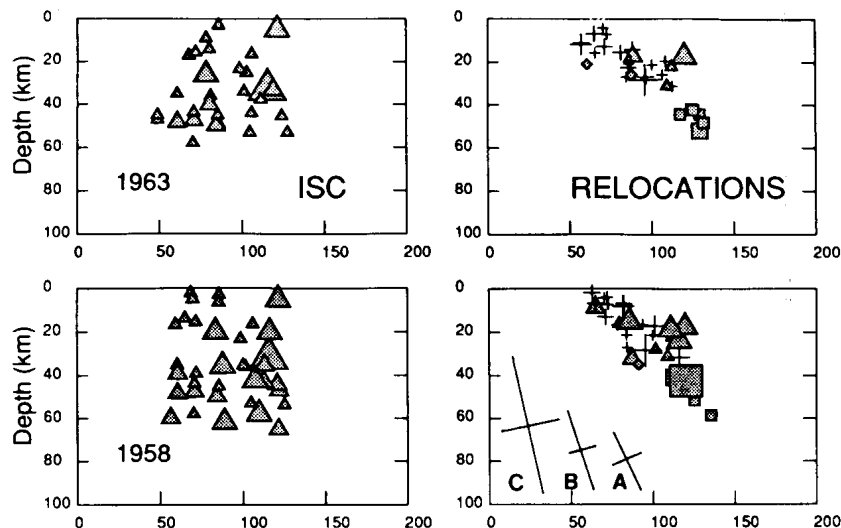


Figure 6 Comparison of earthquake locations using the normal procedure at ISC (left) and JHD relocations (right). The events are located in the Kurile subduction zone along the rupture zones of large thrust events in 1963 and 1958. The vertical cross sections shown traverse the thrust zone from left to right. Note that the JHD solutions reduce the scatter and make it possible to define a dipping plane (from Schwartz et al., 1989).

6 Practical consideration in earthquake locations

This section is intended to give some practical hints on earthquake location. The section does not refer to any particular location program, but most of the parameters discussed can be used with the Hypocenter program (Lienert and Havskov, 1995) or with HYPOSAT (Schweitzer, 2001).

6.1 Phases

The most unambiguous phase to pick is usually P and P is the main phase used in most teleseismic locations. For local earthquakes, usually S-phases are also used. Using phases with different velocities and slowness has the effect of better constraining the distances and there is then less trade-off between depth and origin time or epicenter location and origin time if the epicenter is outside the network. The focal depth is best controlled (with no trade-off between depth and origin time) when phases are included in the location procedure which have different sign of the partial derivative $\partial T/\partial z$ in Eq. (13) such as for very locally observed direct up-going Pg (positive) and Pn (negative) (see section 6.3 Hypocentral depth and Figure 9). In general, it is thus an advantage to use as many different phases as possible under the assumption that they are correctly identified. Recently Schöffel and Das (1999) gave a striking example (see Figure 7). But one very wrong phase can throw off an otherwise well constrained solution. This highlights the crucial importance of the capability of the observatory personal to recognize and report such phases already during their routine seismogram analysis.

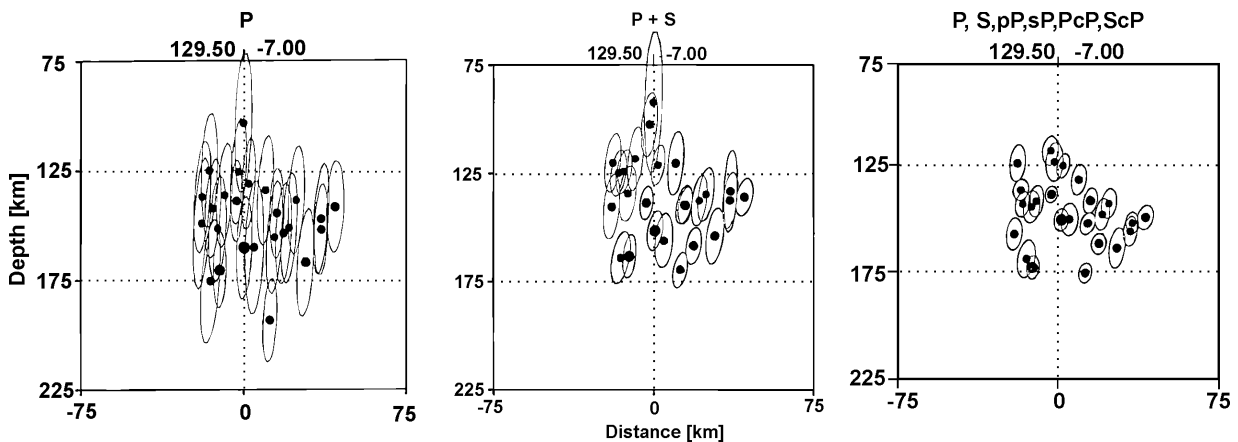


Figure 7 Examples of significant improvement of hypocenter location for teleseismic events by including secondary phases. Left: hypocenter locations using only P-phases; middle: by including S-phases; right: by including also depth phases and core reflections with different sign of $\partial T/\partial z$ (from Schöffel and Das, 1999).

Engdahl et al (1998) used the entire ISC database to relocated more than 100.000 seismic events. They used not only a new scheme to associate properly secondary phases but they also systematically searched for pwP onsets in case of subduction-zone events to get better depth estimates and they used a modern global Earth model (AK135) to avoid the known problems with the Jeffreys-Bullen tables. With all these changes the authors reached a far more consistent distribution (in particular for subduction zones) and sharper picture of global seismicity.

The majority of location programs for local earthquakes only use first arrivals (e.g., HYPO71, Lee and Lahr, 1975). This is good enough for many cases. In some distance ranges, Pn is the first arrival, and it usually has a small amplitude. This means that the corresponding Sn phase, which is then automatically used by the program, might have also a very small amplitude and is not recognized while actually the phase read is Sg or Lg instead. Since the program automatically assumes a first arrival, a wrong travel time curve is used for the observed phase, resulting in a systematic location error. This error is amplified by the fact that the S-phase, due to its low velocity, has a larger influence on the location than the P-phase. It is therefore important to use location programs where all crustal phases can be specified.

Schweitzer (2001) developed an enhanced routine to locate both local/regional and teleseismic events, called HYPOSAT. The program runs with global Earth models and user defined horizontally layered local or regional models. It provides best possible hypocenter estimates of seismic sources by using besides the usual input parameters such as arrival times of first and later onsets (complemented by backazimuth and ray parameters in case of array data or polarization analyses) also travel-time differences between the various observed phases. If S observations are also available, preliminary origin times are estimated by using the Wadati approach (see Figure 3) and a starting epicenter with a priori uncertainties by calculating the intersection of all backazimuth observations. Relocating events with real data Schweitzer could show that HYPOSAT solutions have the smallest errors when besides the absolute onset times also the travel-time differences of all available primary and secondary phase readings are taken into account. The most advanced version of HYPOSAT can be found at <ftp://ftp.norsar.no/pub/outgoing/johannes/hyposat/> and a program description is annexed in PD 11.1.

6.2 Starting location

Iterative location programs commonly start at a point near the station recording the first arrival. This is good enough for most cases, particularly when the station coverage is good and the epicenter is near or within the network. However, this can also lead to problems when using least squares techniques, which converge slowly or sometimes not at all for events outside the limits of a regional network (Buland, 1976). Another possibility is that the solution converges to a local minimum, which might be far from the correct solution. For small-elongated networks, two potential solutions may exist at equal distance from the long axis. A starting location close to the first arrival station can then bias the final solution to the corresponding side of such a network. Although this bias usually is on the correct side, any systematic error in the first-arrival station's time can have a disproportionately large effect on the final location. Thus in many cases, it is desirable to use a better start location than the nearest station. There are several possibilities:

- a) In many cases the analyst knows by experience the approximate location and can then manually give a start location. Most programs have this option.
- b) Similar phases at different stations can be used to determine the apparent velocity and backazimuth of a plane wave using linear regression on the arrival times with respect to the horizontal station coordinates. With the apparent velocity and/or S-P times, an estimate of the start location can be made. This method is particularly useful when locating events far away from the network (regionally or globally).

- c) Backazimuth information is frequently available from 3-component stations or seismic arrays and can be used as under b.
- d) If backazimuth observations are available from different stations, a starting epicenter can be determined by calculating the intersection of all backazimuth observations.
- e) S-P and the circle method can be used with pairs of stations to get an initial location.
- f) The Wadati approach can be used to determine a starting source time.

The starting depth is usually a fixed parameter and set to the most likely depth for the region. For local earthquakes usually the depth range 10-20 km is used, while for distant events, the starting depth is often set to 33 km. If depth phases like e.g., pP are available for distant events, these phases can be used to set or fix the depth (see next section).

6.3 Hypocentral depth

The hypocentral depth is the most difficult parameter to determine due to the fact that the travel-time derivative with respect to depth changes very slowly as function of depth (see Figure 8) unless the station is very close to the epicenter. In other words, the depth can be moved up and down without changing much the travel time. Figure 8 shows a shallow (ray 1) and a deeper event (ray 2). It is clear that the travel-time derivative with respect to depth is nearly zero for ray 1 and but not for ray 2. In this example, it would thus be possible to get an accurate depth estimate for the deeper event but not for the shallower one. Unfortunately, at larger distances from the source, most rays are more like ray 1 than like ray 2 and locations are therefore often made with a fixed ‘normal’ start depth. Only after a reliable epicenter is obtained the program will try to iterate for the depth. Another possibility is to locate the event with several starting depths and then using the depth that gives the best fit to the data. Although one depth will give a best fit to all data, the depth estimate might still be very uncertain and the error estimate must be checked.

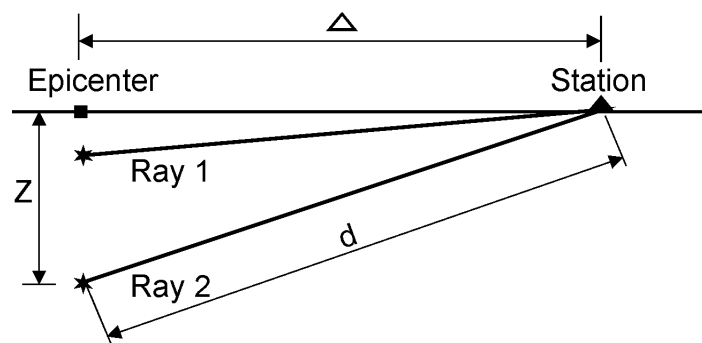


Figure 8 The depth – distance trade off in the determination of focal depth.

For teleseismic events, the best way to improve the depth determination is to include readings from the so-called depth phases (e.g., Gutenberg and Richter, 1936 and 1937; Engdahl et al., 1998) such as pP, pwP (reflection from the ocean free surface), sP, sS or similar but also reflections from the Earth’s core like PcP, ScP or ScS (see Figure 7). The travel-time differences (i.e., depth phase – direct phase) as pP-P, sP-P, sS-S, and pS-S are quite constant over large range of epicentral distances for a given depth so that the depth can be determined nearly independently of the epicenter distance. Another way of getting a reliable depth estimate for teleseismic locations is to have both near and far stations available. In particular,

event observations from local and regional stations and with PKP observations had been used together for this purpose. However, this is unfortunately for many source regions not possible.

For local events, a rule of thumb is that at least several near stations should be not further away than 2 times the depth in order to get a reliable estimate (Figure 8). This is very often not possible, particularly for regional events. At distance larger than $2 \times$ depth, the depth depending partial derivative changes very little with depth if the first arriving phase is the more or less horizontally propagating Pg. But at distances where the critically refracted (so-called head-waves) Pb or Pn arrive, there is again some sensitivity to depth due to the steeply down going rays of Pb or Pn (Figure 9) and because of the different sign of the partial derivatives of their travel times with depth, which is negative, as compared to Pg, which is positive. So, if stations are available at distances with both direct and refracted rays as first arrivals, reasonably reliable solutions might be obtained. An even better solution is when both Pg and Pn are available at the same station and the location capability could be similar to using P and pP for teleseismic events. The problem is that it might be difficult to identify correctly secondary P-phases and a wrong identification might make matters worse.

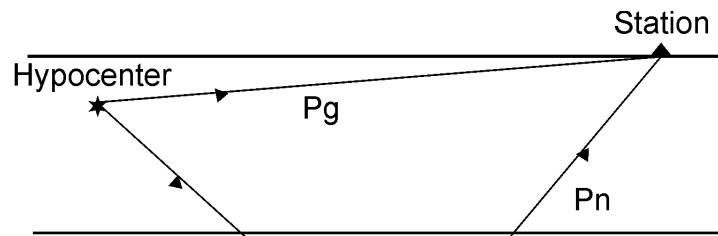


Figure 9 Example of both Pg and Pn rays in the a single layer crustal model.

The depth estimate using a layered crustal model remains problematic even with a mix of phases. Checking catalogs with local earthquakes, it will often be noted that there is a clustering of hypocenters at layer boundaries. This is caused by the discontinuities in the travel-time curves of the direct phase Pg as a function of depth at layer boundaries; see Figure 8 for an example. The Pg travel time suddenly decreases when the hypocenter crosses a boundary (here Moho) since a larger part of the ray suddenly is in a higher velocity layer, while the Pn travel time continuously decreases as the depth increases as long as the event is still within the crust. This gives rise to the discontinuities in the Pg-Pn travel-time curve. So one Pn-Pg travel-time difference is not enough to ensure a reliable depth estimate, several such phase arrivals must be available.

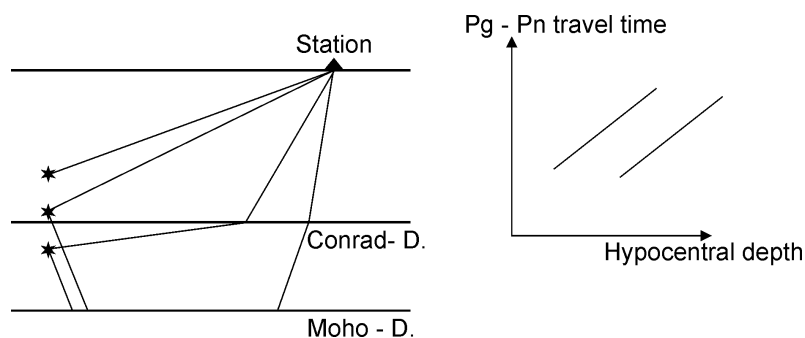


Figure 10 Ray paths of Pg and Pn phases in a two-layer crustal model (left). On the right side the travel-time curve of Pg-Pn as a function of depth is sketched.

Even when several Pg and Pn phases are available, depth estimates still remains a problems at regional distances due to the uncertainty in the crustal models. Since the depth estimates are critically dependent on the accurate calculation of Pg and Pn travel times, small uncertainties in the model can quickly throw off the depth estimate.

Many location programs give the *RMS* of the travel-time residuals in a grid around the calculated hypocenter. This, in addition to the error estimates, gives an idea about the accuracy and a local minimum might be found in this way. A more direct way of estimating the quality of the depth estimate is to calculate the *RMS* as a function of depth in order to check if a local minimum has been reached. This is particularly relevant for crustal earthquakes at shallow depth and can also be used as a complementary tool for better discriminating between quarry blasts and earthquakes.

6.4 Outliers and weighting schemes

The largest residuals have disproportionally large influence on the fit of the arrival times due to the commonly used least squares fit. Most location programs will have some kind of residual weighting scheme in which observations with large residuals are given lower or even no weight. Bisquare weighting is often used for teleseismic events (Anderson, 1982). The residual weighting works very well if the residuals are not extreme since the residual weighting can only be used after a few iterations so that the residuals are close to the final ones. Individual large residuals can often lead to completely wrong solutions, even when 90 % of the data are good, residual weighting will not help in these cases. Some programs will try to scan the data for gross errors (like minute errors) before starting the iterative procedure. If an event has large residuals, try to look for obvious outliers. A Wadati diagram can often help in spotting bad readings for local earthquakes (see Figure 3).

The arrival-time observations will by default always have different weights in the inversion. A simple case is that S-waves may have larger weights than P-waves due to their lower velocities. An extreme case is the T-wave (a guided waves in the ocean), which with its low velocity (1.5 km/s) can completely dominate the solution. Considering, that the accuracy of the picks is probably best for the P-waves, therefore it should be natural, that P-arrivals should have more importance than S-arrivals in the location. However, the default parameter setting in most location programs is to leave the original weights unless the user actively changes them. It is normally possible to give ‘a priori’ for all S-phases a lower weight and in addition, all phases can be given individual weights, including being totally weighted out.

When working with local earthquakes, the nearest stations will usually provide the most accurate information due to the clarity of the phases. In addition, uncertainty in the local model has less influence on the results at short distances than at larger distances; this is particularly true for the depth estimate. It is therefore desirable to put more weight on data from near stations than on those from distant stations and this is usually done by using a distance weighting function of

$$w_d = \frac{x_{far} - \Delta}{x_{far} - x_{near}}, \quad (24)$$

where Δ is the epicentral distance, x_{near} is the distance to which full weight is used and x_{far} is the distance where the weight is set to zero (or reduced). The constants x_{near} and x_{far} are adjusted to fit the size of the network; x_{near} should be about the diameter of the network, and x_{far} about twice x_{near} . For a dense network, x_{near} and x_{far} might be made even smaller to more accurate solutions.

6.5 Ellipticity of the Earth

Until now we only assumed that the model used for calculating distances or travel times is either for local or regional events a flat model or for teleseismic events a standard spherical model of the Earth. However, the Earth is neither a sphere nor a flat disk but an ellipsoid symmetrical to its rotation axis. It was Gutenberg and Richter (1933) who first pointed out that the difference between a sphere and an ellipsoid must be taken in account when calculating epicentral distances and consequently also the travel times of seismic phases. Therefore, they proposed the usage of geocentric coordinates instead of geographic coordinates to calculate distances and angles on the Earth. Because of the axially symmetrical figure of the Earth, the geocentric longitude is identical to the geographic longitude. To convert a geographic latitude lat_g into a geocentric latitude lat_c one can use the following formula:

$$lat_c = \arctan((1 - (6378.136 - 6356.751)/6378.136)^2 * \tan lat_g). \quad (25)$$

With this formula all station latitudes have to be converted before an event location and after the inversion, the resulting geocentric event latitude has to be converted back by applying the inverse equation

$$lat_g = \arctan(\tan lat_c / (1 - (6378.136 - 6356.751)/6378.136)^2). \quad (26)$$

With this procedure all angle calculations related to an event location are done for a sphere. The calculated distances are measured in degrees and to convert them in km, one has to use the local Earth radius R_{loc} :

$$R_{loc} = \sqrt{(6378.136 * \cos lat_c)^2 + (6356.751 * \sin lat_c)^2}. \quad (27)$$

This value has then to be applied for converting a distance D measured in degrees into a distance measured in km, or vice versa:

$$D[km] = \frac{2\pi * R_{loc}}{360} * D[deg] \quad \text{or} \quad D[deg] = \frac{360}{2\pi * R_{loc}} * D[km] \quad (28)$$

All standard Earth models are spherically symmetrical Earth with a mean radius of 6371 km. Therefore the standard tables also contain travel times calculated for a sphere. Bullen (1937, 1938, 1939) was the first, who calculated latitude depending travel-time corrections (ellipticity corrections) to be used together with travel-time tables for a spherical Earth. Later work on this topic was done by Dziewonski and Gilbert (1976) and Dornboos (1988). Kennett and Gudmundsson (1996) published the most recent set of ellipticity corrections for a large number of seismic phases.

In conclusion: to get the theoretical travel time for an event in teleseismic or regional distance, one has to calculate the geocentric epicentral distance, then one has to use travel-time tables as calculated for a spherical Earth model, and finally one has to apply the latitude (event and station!) depending ellipticity correction. Most location routines do automatically apply the described methods and formulas but it is important to check this in detail and eventually to change a location program.

6.6 Importance of the model

In this context the importance of the model assumptions underlying the location procedure have to be emphasized. Many studies showed (e.g., Kissling, 1988) that accuracy of locating hypocenters can be improved by using a well-constrained minimum 1D velocity model with station corrections is better than using a regional 1D model. However, Spallarossa et al. (2001) recently showed, that in strongly heterogeneous local areas even a 1D model with station corrections does not significantly improve the accuracy of the location parameters. High-precision location can in such case be achieved only by using a 3D model. This is particularly true for locating earthquakes in volcanic areas (see Lomax et al., 2001).

Smith and Ekström (1996) investigated the improvement of teleseismic event locations by using a recent three-dimensional Earth models. They came to the conclusion that it "... offers improvement in event locations over all three 1D models with, or without, station corrections." For the explosion events, the average mislocation distance is reduced by approximately 40 %; for the earthquakes, the improvements are smaller. Corrections for crustal thickness beneath source and receiver are found to be of similar magnitude to the mantle corrections, but use of station corrections together with the 3D mantle model provide the best locations. Also Chen and Willemann (2001) carried out a global test of seismic event locations using three-dimensional Earth models. Although achieved by using a 3D model a more tightly clustering of earthquakes in subduction zones than by using depth from the ISC Bulletin based on 1D model calculations, they concluded that the clustering was not as tightly as for depths computed by Engdahl et al. (1998) who used depth phases as well as direct phases. Thus, even using the best available global 3D models can not compensate for the non-use of depth phases and core reflections in teleseismic hypocenter location (see Figure 7).

A case example for improved location of local events is given in Figures 11 and 12. The upper panel in Figure 11 shows the initial locations for aftershocks of the Cariaco earthquake ($M_s = 6.8$) on July 9, 1997 in NE of Venezuela based an averaged 1D crustal velocity model. The mean location error (i.e., the calculated precision with respect to the assumed model) was about 900 m. On the average, the aftershocks occurred about 2 to 3 km north of the surface fault trace. A detailed tomographic study revealed lateral velocity contrasts of up to 20 % with higher velocities towards the north of the El Pilar fault. Relocating the events with the 3D velocity model the epicenters were systematically shifted southward by about 2 km and now align in their majority rather well with fault traces mapped before the earthquake as well as with newly ruptured fault traces. Also in the cross sections the data scatter was clearly reduced so that closely spaced outcropping surface faults could be traced down to a depth of more than 10 km. This results hints to the fact that in the presence of lateral velocity inhomogeneities epicenter locations are systematically displaced in the direction of higher velocities. We will look into this problem more closely in section 7.

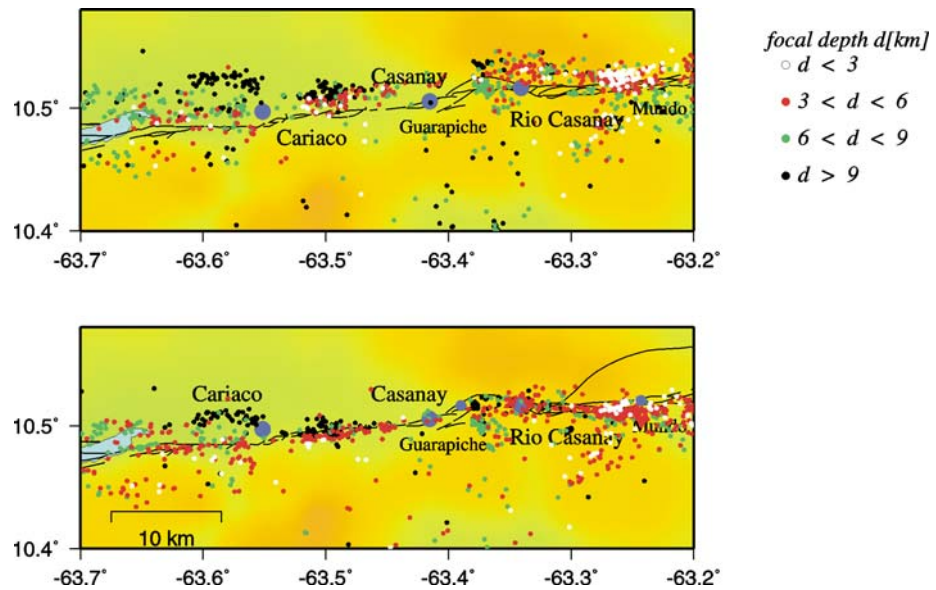


Figure 11 Epicentral distribution of aftershocks of the Cariaco earthquake ($M_s=6.8$) on July 9, 1997 in NE of Venezuela. Top: results from HYPO71 based on a one-dimensional velocity-depth distribution. Bottom: Relocation of the aftershocks on the basis of a three-dimensional model derived from a tomographic study of the aftershock region (courtesy of M. Baumbach, H. Grosse and A. Rietbrock).

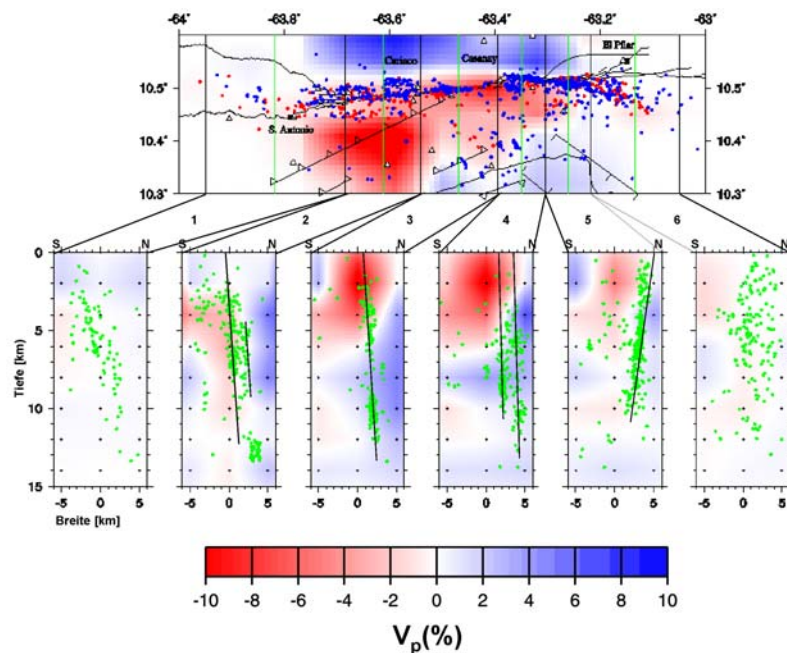


Figure 12 3-D distribution of the P-wave velocity in the focal region of the 1997 Cariaco earthquake as derived from a tomographic study. The horizontal section shows the velocity distribution in the layer between 2 km and 4 km depth. Red and blue dots mark the epicenters of the aftershocks. The red ones were chosen because of their suitability for the tomography. The six vertical cross sections show the depths distribution of the aftershocks (green dots) together with the deviations of the P-wave velocity from the average reference model. The depth range and the lateral changes of fault dip are obvious (courtesy of M. Baumbach, H. Grosse and A. Rietbrock).

7 Internal and external (real) accuracy of locations

For decades the international data centers have located earthquakes world-wide by means of the 1D Jeffreys and Bullen (1940, 1948, 1958, 1967, and 1970) travel-time tables without external control of the accuracy of such solutions by checking them independent and similarly strong events of exactly known position and origin time. Therefore, the question remained open for a long time whether these calculated location errors were real or just the minimized average errors for the best fitting solutions to the observed data based on the various model assumptions made with respect to the validity of the velocity model, the non-correlation of the various parameters to be determined and the Gaussian distribution of the model and data reading errors involved. If the latter was the case then the calculated errors were not measure of the real accuracy of the calculated location and origin time but rather a measure of the internal precision of fitting the data to the model assumptions.

In order to investigate this in more detail, Bormann (1972) looked into the travel-time errors reported by the international data centers for the German seismological observatory Moxa (MOX) for earthquakes in different regions of the world. As an example, he got for the same data set of events from the Kurile Islands the mean residual $\bar{\delta}t_p = + 0.16$ s and a standard deviation $\sigma = \pm 0.65$ s when referring the MOX onset-time readings to the locations published by the U.S. Coastal and Geodetic Survey (USCGS, World Data Center A, WDC A) and $\bar{\delta}t_p = + 0.35$ s with $\sigma = \pm 1.1$ s when referred to the locations published by the Academy of Sciences of the Soviet Union (ANUSSR, World Data Center B, WDC B) which used the same J-B travel-time model as USCGS. Thus, the travel-time (or onset-time reading) errors calculated by the data centers for seismic stations are not real errors of these stations or their readings but depend on the number and distribution of stations used by these centers in their location procedure. And these were rather different for WDC A and WDC B. While the USCGS used the data of a worldwide station network ANUSSR based its locations on the station network of the former Soviet Union and East European countries and these “looked at” events outside of Eurasia from a much narrower azimuth and distance range. But this is just equivalent to the above discussion related to Figure 4. The mean residuals calculated by these two centers for the considered region were not significantly different and not far from zero. Therefore, the question remained whether there were systematic biases in these solutions and if so, of what kind and how big they were.

From the 60's onwards testing of strong underground nuclear explosions (UNE) provided for the first time independent strong sources with precisely known coordinates and origin time which allowed to check the accuracy of calculated seismic source locations from global seismic observations. During the last years for many UNEs such information was released. However, for the LONGSHOT explosion on the Amchitka Islands, Aleutians, the source parameters were known since many years. For this event the residual of MOX was $\delta t_p = -4.6$ s! This contrasted strongly with calculated residuals for Aleutian earthquakes. From 53 analyzed earthquakes in that region, no negative residual at MOX was larger than -0.8 s! Interestingly, the USGS had calculated for LONGSHOT a location 25 km NW of the true place (which explains -1 s travel-time error at MOX) and an origin time which was 3.5 s earlier than the real one (which accounts for the remaining -3.5 s!) (Sykes, 1966). The too early source time is a meanwhile well-understood artifact of the Jeffreys-Bullen tables, which generally give too long P-phase travel times. According to Fedotov and Slavina (1968) epicenters calculated by the WDC B from events in the Aleutians are generally displaced towards NW with respect to those of the WDC A. Consequently, with the same systematic tendency of shift, they deviated still more from the true locations of events in that area.

To get the best geographic coverage for each seismic event, the ISC waits with its event location about two years to collect as much as possible seismogram readings from all worldwide distributed seismological observatories.

What is the reason for this systematic mislocation, which usually remains unrecognized unless one locates strong independently controlled sources of exactly known source parameters and origin time? Figure 13 shows some hypothetical earthquakes at different depth on a vertically dipping fault. It separates two half-spaces with different wave propagation velocity $v_2 > v_1$. This is a realistic model for parts of the San Andreas Fault. The lateral velocity difference across the fault may be as large as 5 to 7 %. S1 and S2 may be two stations at the same hypocentral distances from the events. But because of $v_2 > v_1$ the onset time t_2 at S2 is earlier (travel-time shorter) than for t_1 at S1. Running now the location procedure with the common residual minimization on the assumption of a laterally homogeneous velocity model will result in hypocentral distances $d_2(h) < d_1(h)$. Since the difference increases with depth, the hypocenters are not only offset from the real fault but seem to mark even a slightly inclined fault, which is not the case.

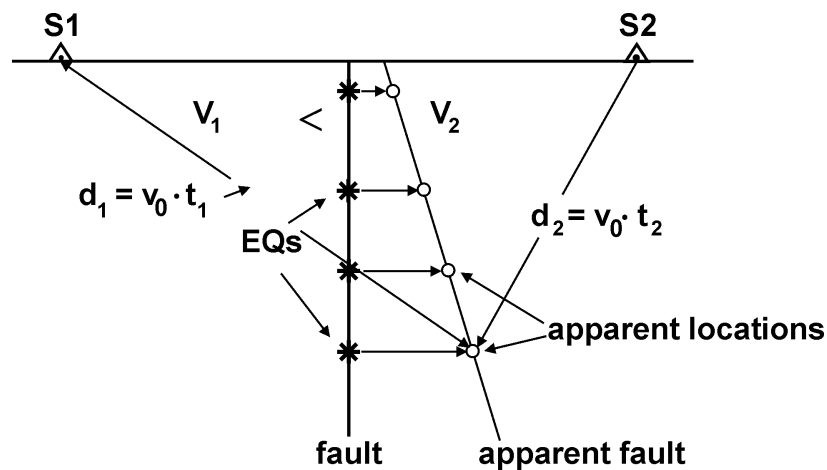


Figure 13 Illustration of the systematic mislocation of earthquakes along a fault with strong lateral velocity contrast. v_0 is the assumed model velocity with $v_2 > v_0 > v_1$.

From this hypothetical example we learn that localizations based on 1D velocity models in the presence of 2D or 3D velocity inhomogeneities will be systematically shifted in the direction of increasing velocities (or velocity gradients), the more so the less the station distribution controls the event from all azimuths. Precisely this was the cause for the larger systematic mislocation of WDC B as compared to WDC A. While the latter localizes events using data from a global network, the former used solely data from the former Soviet and East European territory, i.e., stations which view the Aleutian Islands only from a narrow azimuth range. The direction of systematic mislocation of both centers to the NW agrees with the NW directed subduction of the Pacific plate underneath the Aleutians. According to Jacob (1972) this cold lithospheric plate has 7 to 10% higher P-wave velocities than the surrounding mantle. A recent study by Lienert (1997) addresses also this problem of assessing the reliability of earthquake locations by using known nuclear tests.

Acknowledgements

Part of text follows a similar description in Shearer (1999). Figures and ideas have also been taken from Stein (1991), Lay and Wallace (1995), Schöffel and Das (1999). Special thanks go to M. Baumbach, H. Grosser and A. Rietbrock for making Figures 11 and 12 available and to R. E. Engdahl for critical proof reading and valuable suggestions which helped to improve the text and to complement the references.

References

- Anderson, K. R. (1982). Robust earthquake location using M-estimates, *Phys. Earth. Plan. Inter* **30**, 119-130.
- Bormann, P. (1972). A study of travel-time residuals with respect to the location of teleseismic events from body-wave records at Moxa station. *Gerlands Beiträge zur Geophysik* **81**, 117-124.
- Buland, R. (1976). The mechanics of locating earthquakes, *Bull. Seism. Soc. Am.* **66**, 173-187.
- Buland, R. and Chapman, C. H. (1983). The computation of seismic travel times. *Bull. Seism. Soc. Am.*, **73**, 1271-1303.
- Bullen, K.E. (1937, 1938, 1939). The ellipticity correction to travel-times of P and S earthquake waves. *Montl. Not. R. Astr. Soc., Geophys. Suppl.* **4**, 143-157, 158-164, 317-331, 332-337, 469-471.
- Båth, M. (1979). *Introduction to seismology*, 428 pp., Birkhäuser Verlag. Basel.
- Chen, Q.F. and Willemann, R. J. (2001). Global test of seismic event locations using three dimensional Earth models. *Bull. Seis. Soc. Am.* **91**, 1704-1716.
- Di Giovambattista, R. and Barba, S. (1997). An estimate of hypocenter location accuracy in a large network, possible implication for tectonic studies in Italy. *Geophys. J. Int.* **129**, 124-132.
- Dornboos, D.J. (1988). Asphericity and ellipticity corrections. In: Dornboos, D.J. (ed.). *Seismological Algorithms*. Academic Press, New York 1988, 17 + 469 pp.
- Douglas, A. (1967). Joint hypocenter determination. *Nature* **215**, 47-48.
- Dziewosnki, A.M. and Gilbert, F. (1976). The effect of small, aspherical perturbations on travel times and a re-examination of the corrections for ellipticity. *Geophys. J. R. Astr. Soc.* **44**, 7-17.
- Engdahl, E.R., van der Hilst, R. and Buland, R. (1998), Global teleseismic earthquake relocation with improved travel times and procedures for depth determination, *Bull. Seism. Soc. Am.* **88**, 722-743.
- Fedotov, S.A. and Slavina, L.B. (1968). Estimate of the velocity of longitudinal waves in the upper mantle under the northwestern part of the Pacific Ocean and Kamchatka (in Russian). *Izv. Akad. Nauk SSSR, Fizika Zemli* **2**, 8-31.
- Geiger, L. (1910). Herdbestimmung bei Erdbeben aus den Ankunftszeiten. *Nachrichten von der Königlichen Gesellschaft der Wissenschaften zu Göttingen, Mathematisch-Physikalische Klasse*, 331-349. (1912 translated to English by F.W.L. Peebles and A.H. Corey: Probability method for the determination of earthquake epicenters from the arrival time only. *Bulletin St. Louis University* **8**, 60-71).
- Gomberg, J. S., Shedlock, K. M., and Roecker, W. W. (1990). The effect of S-wave arrivals times on the accuracy of hypocenter estimation. *Bull. Seism. Soc. Am.*, **80**, 6, 1605-1628.
- Gutenberg, B. and Richter, C.F. (1933). Advantages of using geocentric latitude in calculating distances. *Gerlands Beiträge zur Geophysik* **40**, 380-389.

- Gutenberg, B. and C.F. Richter (1936). Materials for the study of deep-focus earthquakes. Bull. Seism. Soc. Am. **26**, 341 – 390 (edition in French: Données relatives a l'étude des tremblements de terre a foyer profond. Publications du Bureau Central Séismologique International, Série A, Travaux Scientifiques **15**, 1 - 70, 1937).
- Gutenberg, B. and C.F. Richter (1937). Materials for the study of deep-focus earthquakes (second paper). Bull. Seism. Soc. Am. **27**, 157 – 184 (partly edited in French: Données relatives a l'étude des tremblements de terre a foyer profond. Publications du Bureau Central Séismologique International, Série A, Travaux Scientifiques **15**, 1 - 70, 1937).
- Jacob, K.H. (1972). Global tectonic implications of anomalous seismic P travel-times from the nuclear explosion Longshot. J. Geophys. Res. **77**, 14.
- Jeffreys, H. and Bullen, K.E. (1940, 1948, 1958, 1967, and 1970). Seismological Tables, British Association for the Advancement of Science, Gray Milne Trust, London, 50 pp.
- Kissling, E. (1988). Geotomography with local earthquake data. Rev. Geophys. **26**, 659-698.
- Kennett, B.L.N. (1991). IASPEI 1991 Seismological Tables. Australian National University, Research School of Earth Sciences, 167 pp.
- Kennett, B.L.N., and Engdahl, E.R. (1991), Travel times for global earthquake location and phase identification, Geophys. J. Int. **105**, 429-466.
- Kennett, B.L.N., Engdahl, E.R., and Buland, R. (1995), Constraints on seismic velocities in the Earth from traveltimes, Geophys. J. Int. **122**, 108-124.
- Kennett, B.L.N. and Gudmundsson, O. (1996). Ellipticity corrections for seismic phases, Geophys. J. Int. **127**, 40-48.
- Lay, T. and Wallace, T.C. (1995). Modern global seismology, 521 pp., Academic Press.
- Lee, W.H.K. and Lahr, J.C. (1975). HYPO71 (revised): A computer program for determining local earthquakes hypocentral parameters, magnitude, and first motion pattern. U.S. Geological Survey Open-File Report **75-311**, 100 pp.
- Lienert, B.R. and Havskov, J. (1995). A computer program for locating earthquakes both locally and globally. Seismological Research Letters **66**, 26-36.
- Lienert, B.R. (1997). Assessment of earthquake location accuracy and confidence region estimate using known nuclear tests. Bull. Seismol. Soc. Am. **87**, 1150-1157.
- Lomax, A., Virieux, J., Volant, Ph. and Gerge-Thierry, C. (2000). Probabilistic earthquake location in 3D and layered models. In: Thurber, C. H. and Rabinovitz, N. (Eds.)(2000). Advances in seismic event location. Kluwer Academic Publishers, 101-134.
- Lomax, A., Zollo, A., Capuano, P. and Virieux, J. (2001). Precise, absolute earthquake locations under Somma-Vesuvius volcano using a new three-dimensional velocity model. Geophys. J. Int. **146**, 313-331.
- McLaren, J. P., and Frohlich, C. (1985). Model calculations of regional network locations for earthquakes in subduction zones. Bull. Seism. Soc. Am., **75**, 2, 397-413.
- Morelli, A., and Dziewonski, A.M. (1993), Body-wave traveltimes and a spherically symmetric P- and S-wave velocity model, Geophys. J. Int. **112**, 178-194.
- Müller, G. (1977). Earth flattening approximation for body waves derived from geometric ray geometry - improvements, corrections and range of applicability, J. Geophys. **42**, 429-436.
- Parolai, S., Trojani, L., Monachesi, G., Frapiccini, M., Cattaneo, M. and Augliera, P. (2001). Hypocenter location accuracy and seismicity distribution in the Central Apennines (Italy). Journal of Seismology **5**, 243-261.
- Pujol, J. (2000). Joint event location – the JHD technique and applications to data from local networks. In: Thurber Rabinovitz(2000), 163-204.
- Ringdal, F. and Kennett, B.L.N (Eds.) (2001). Special issue: Monitoring the Comprehensive Nuclear-Test-Ban Treaty: Source location. Pure appl. Geophys., **158**, Number 1/2, 1-419.

- Roberts, R.G., Christofferson, A. and Cassedy, F. (1989). Real time event detection, phase identification and source location using single station 3 component seismic data and a small PC. *Geophysical Journal* **97**, 471-480.
- Ružek, B. and Kvasnička, M. (2001). Differential evolution algorithm in earthquake hypocenter location. *Pure appl. geophys.* **158**, 667-693.
- Saari, J. (1991). Automated phase picker and source location algorithm for local distances using a single three-component seismic station. *Tectonophysics* **189**, 307-315.
- Sambridge, M.S. and Kennett, B.L.N. (1986). A novel method of hypocentre location. *Geophys. J. R. astr. Soc.*, **87**, 679-697.
- Sambridge, M.S. and Kennett, B.L.N. (2001). Seismic event location: nonlinear inversion using a neighbourhood algorithm. *Pure appl. Geophys.*, **158**, 241-257.
- Schöffel, H.-J. and Das, S. (1999). Fine details of the Wadati-Benioff zone under Indonesia and its geodynamic implications. *J. Geophys. Res.* **104**, 13101-13114.
- Shearer, P. M. (1999). *Introduction to seismology*, 260 pp., Cambridge University Press.
- Stein, S. (1991). *Introduction to seismology, earthquakes and Earth structure*. Lecture notes, Department of Geological sciences, Northwestern University, USA.
- Schwartz, S. Y., Dewey, J.W., and Lay, T. (1989). Influence of fault plane heterogeneity on the seismic behavior in southern Kurile Islands arc. *J. Geophys. Res.* **94**, 5637-5649.
- Schweitzer, J. (2001). HYPOSAT – An enhanced routine to locate seismic events. *Pure and Applied Geophysics* **158**, 277-289.
- Smith, G. P. and Ekström, G. (1996). Improving teleseismic event locations using a three-dimensional Earth model. *Bull. Seism. Soc. Am.*, **86**, 3, 788-796.
- Spallarossa, D., Ferretti, G., Augliera, P., Bindi, D. and Cattaneo, M. (2001). Reliability of earthquake location procedures in heterogeneous areas: synthetic tests in the South Western Alps, Italy. *Phys. Earth Planet. Int.* **123**, 247-266.
- Sykes, L.R. (1966). The seismicity and the deep structure of island arcs. *J. Geophys. Res.* **27**, 2981-3006.
- Thurber, C. H. and Rabinovitz, N. (Eds.) (2000). *Advances in seismic event location*. Kluwer Academic Publishers, 266 pp.
- Thurber, C. H. and Engdahl, E.R. (2000). Advances in global seismic event location. In: Thurber and Rabinovitz (2000), 3-22.
- Thurber, C. H. and Kissling, E. (2000). Advances in travel-time calculations for three-dimensional structures. In: Thurber and Rabinovitz (2000), 71-100.
- Uhrhammer, R. A. (1980). Analysis of small seismographic station networks. *Bull. Seism. Soc. Am.*, **70**, 4, 1369-1379.
- Wadati, K. (1933). On the travel time of earthquake waves. Part. II, *Geophys. Mag. (Tokyo)* **7**, 101-111.
- Waldhauser, F. and Ellsworth, W.L. (2000). A double-difference earthquake location algorithm: method and application to the Northern Hayward fault, California. *Bull. Seism. Soc. Am.* **90**, 13553-1368.
- Wiechert, E. (1907). Über Erdbebenwellen. Theoretisches über die Ausbreitung der Erdbebenwellen. *Nachrichten von der Königlichen Gesellschaft der Wissenschaften zu Göttingen, Mathematisch-physikalische Klasse*, 413-529.

3.4 Determination of fault-plane solutions

3.4.1 Introduction

The direction (polarity) and amplitude of motion of a seismic wave arriving at a distant station depends both on the wave type considered and the position of the station relative to the motion in the earthquake source. This is illustrated by Figs. 3.21a and b.

Fig. 3.21a represents a linear displacement of a point source **S** while Fig. 9b depicts a right lateral (dextral) shear dislocation along a fault plane **F**. Shear dislocations are the most common model to explain earthquake fault ruptures. Note that in the discussion below we consider the source to be a point source with dimension much smaller than the distance to the stations and the wave length considered. First we look into the situation depicted in Fig. 3.21a. When **S** moves towards $\Delta 1$ then this station will observe a *compressional* (+) P-wave arrival (i.e., the first motion is *away* from **S**), $\Delta 4$ will record a P-wave of opposite sign (-), a *dilatation* (i.e., first motion *towards* **S**), and station $\Delta 2$ will receive no P-wave at all. On the other hand, S-waves, which are polarized parallel to the displacement of **S** and perpendicular to the direction of wave propagation, will be recorded at $\Delta 2$ but not at $\Delta 1$ and $\Delta 4$ while station $\Delta 3$ will receive both P- and S-waves.

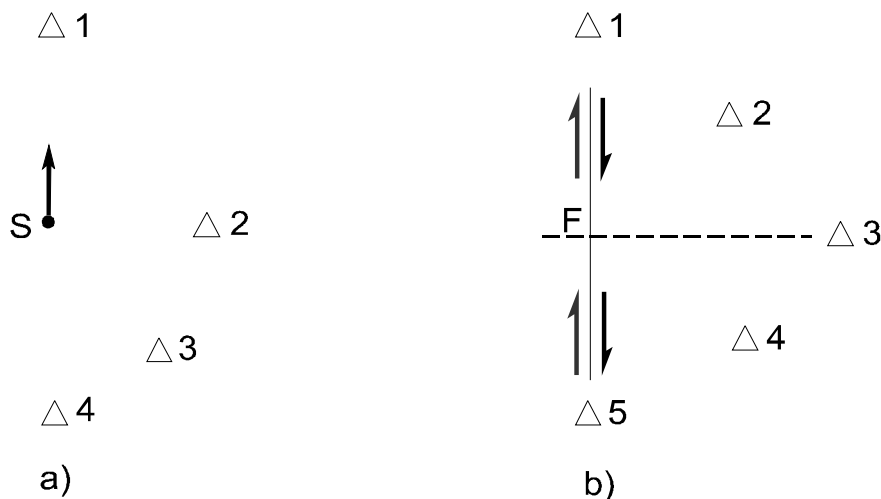


Fig. 3.21 Direction of source displacement with respect to seismic stations Δ_i for a) a single force at point **S** and b) a fault rupture **F**. Note that in the discussion below we consider the source to be a point source with an rupture dimension much smaller than the distance to the stations.

Somewhat different is the case of a fault rupture (Fig. 3.21b). At stations $\Delta 1$ and $\Delta 5$, which are positioned in the strike direction of the fault, the opposite signs of P motion on both side of the fault will cancel, i.e., no P-waves will be observed. The latter also applies for station $\Delta 3$ which is sited perpendicular to the fault. On the other hand, stations $\Delta 2$ and $\Delta 4$, which are positioned at an angle of 45° with respect to the fault, will record the P-wave motions with maximum amplitudes but opposite sign. This becomes clear also from Fig. 3.23a. It shows the different polarities and the amplitude "lobes" in the four quadrants. The length of the displacement arrows is proportional to the P-wave amplitudes observed in different directions

from the fault. Accordingly, by observing the sense of first motions of P-waves at many stations at different azimuths with respect to the source it will be possible to deduce a "fault-plane solution". But because of the symmetry of the first-motion patterns, two potential rupture planes, perpendicular to each other, can be constructed. Thus, on the basis of polarity data alone, an ambiguity will remain as to which one was the acting fault plane. This can only be decided by taking into account additional data on azimuthal amplitude and frequency or wave-form patterns, which are controlled by the Doppler effect of the moving source, and/or field data on the orientation and nature of seismotectonic faults.

In accordance with the above, the amplitude distribution of P waves for a point source with pure double-couple shear mechanism is described in a spherical co-ordinate system (θ, ϕ) (Aki and Richards, 1980; see Fig. 3.22) by

$$A_P(\theta, \phi) = \cos \phi \sin 2\theta. \quad (3.67)$$

This expression divides the focal sphere into 4 quadrants. The focal sphere for a seismic point source is a conceived sphere of arbitrarily small radius centered on the source. Within each quadrant the sign of the P-wave first motion (polarity) does not change but amplitudes are large in the center of the quadrant and small (or zero) near to (or at) the fault plane and the auxiliary plane. The nodal lines for P-waves, on which $A_P(\theta, \phi) = \cos \phi \sin 2\theta = 0$, separate

the quadrants. They coincide with the horizontal projection of the two orthogonal fault planes traces through the focal sphere. Opposite quadrants have the same polarity, neighboring quadrants different polarities. Note that *compression* is observed at stations falling in the *tension quadrant* (force directed away from the point source) while *dilatation* is observed at stations falling in the *compression quadrant* (force directed towards the point source).

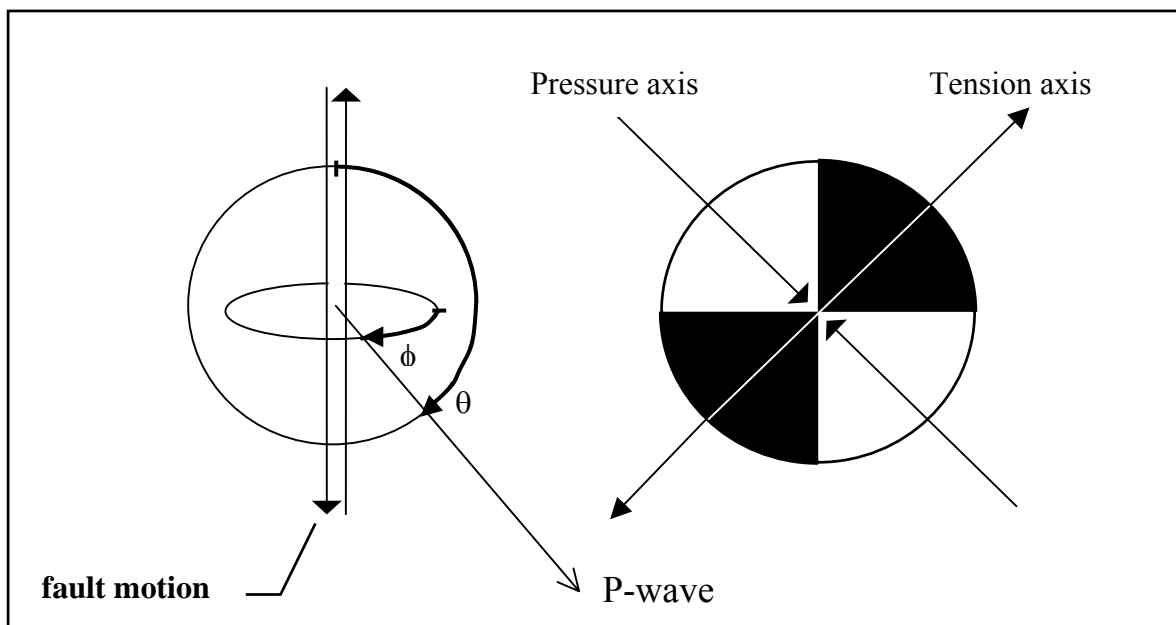


Fig. 3.22 Map view of P-wave radiation pattern for a shear fault. θ is the azimuth in the plane while ϕ is in fact three-dimensional. See also Fig. 3.23. Black areas: polarity +, white areas - .

The position of the quadrants on the focal sphere depends on the orientation of the active fault and of the slip direction in space. This is illustrated by Fig. 3.23, which shows the P-wave radiation pattern for a thrust event with some strike-slip component. Thus, the estimation of the P-wave first motion polarities and their back-projection onto the focal sphere allows us to identify the type of focal mechanism of a shear event (fault-plane solution). The only problem is, that the hypocenter and the seismic ray path from the source to the individual stations must be known. This may be difficult for a heterogeneous model with 2D or 3D-velocity structure.

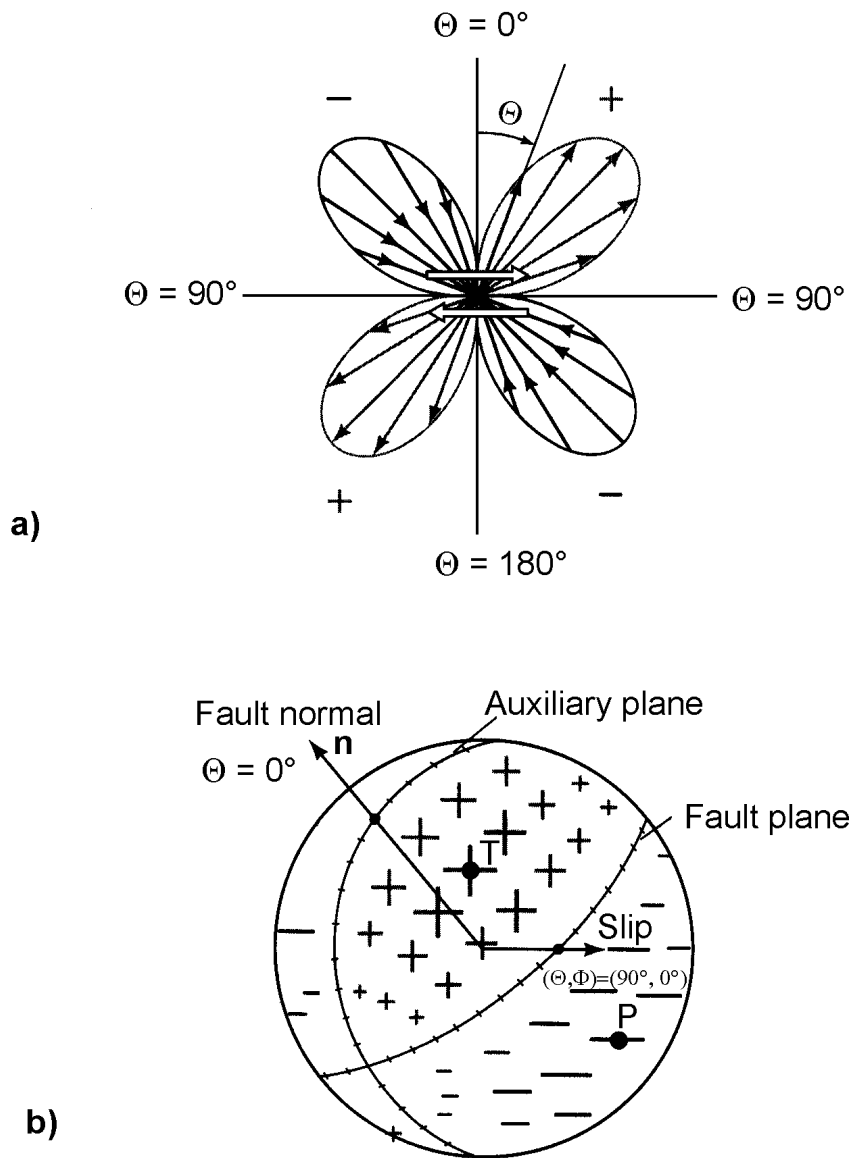


Fig. 3.23 Radiation pattern of the radial displacement component (P-wave) due to a double-couple source: a) for a plane of constant azimuth (with lobe amplitudes proportional to $\sin 2\theta$) and b) over a sphere centered on the origin. Plus and minus signs of various sizes denote amplitude variation (with θ and ϕ) of outward and inward directed motions. The fault plane and auxiliary plane are nodal lines on which $\cos\phi \sin 2\theta = 0$. The pair of arrows in a) at the center denotes the shear dislocation. Note the alternating quadrants of inward and outward directions. (Modified from Aki and Richards 1980 ; with kind permission of the authors).

Fault-plane solutions based on P-wave first motion polarities will be better constrained if additionally the different radiation pattern of S-waves displacement amplitudes is taken into account. An example is given in Fig. 3.24 for the same fault-plane solution as shown in Fig. 3.23 for P-waves.

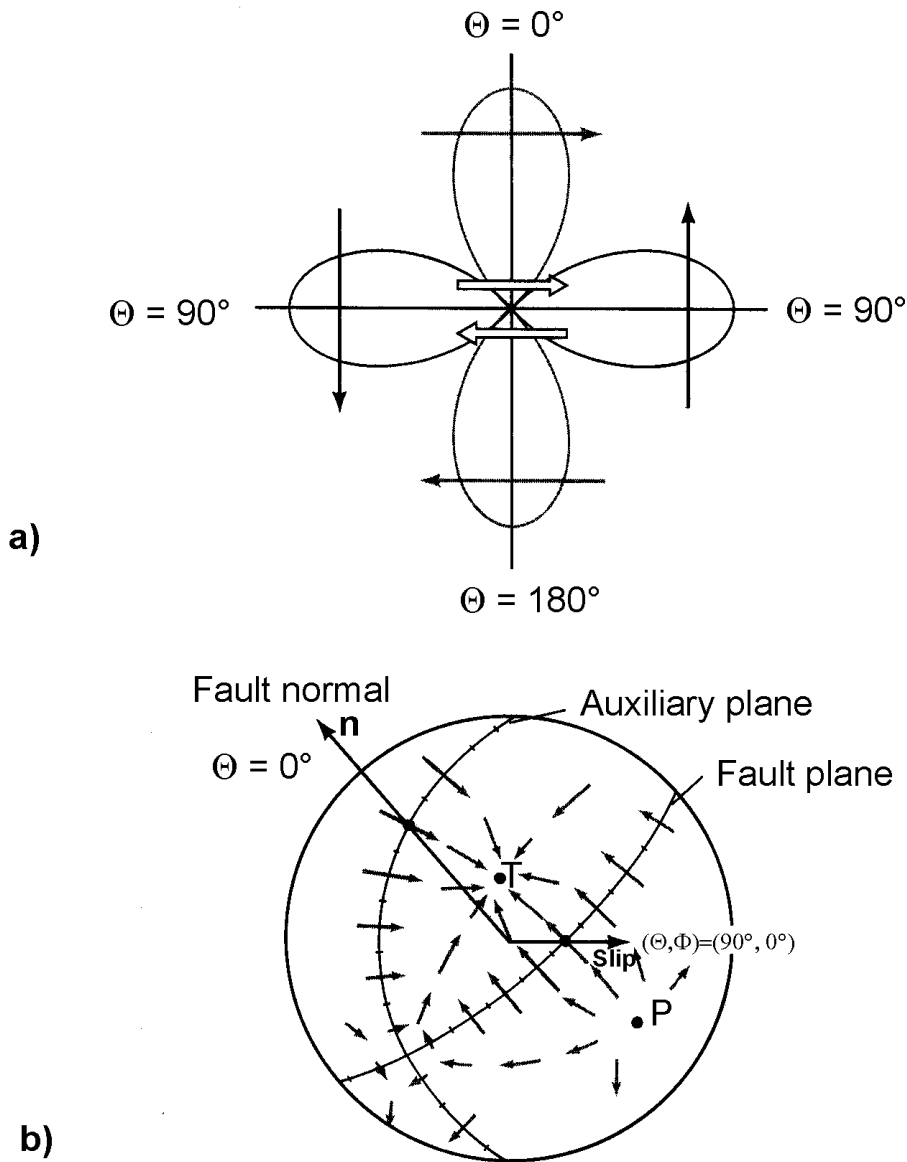


Fig. 3.24 Radiation pattern of the transverse displacement component (S-wave) due to a double-couple source. a) in the plane $\{\phi = 0, \phi = \pi\}$ and b) over a sphere centered on the origin. Arrows imposed on each lobe in a) show the direction of particle displacement associated with the lobe while the arrows with varying size and direction in the spherical surface in b) indicate the variation of the transverse motions with θ and ϕ . There are no nodal lines as in Fig. 3.23 but only nodal points where there is zero motion. Note that the nodal point for transverse motion at $(\theta, \phi) = (45^\circ, 0^\circ)$ at T is a maximum in the pattern for longitudinal motion (see Fig.3.23) while the maximum transverse motion (e.g., at $\theta = 0$) occurs on a nodal line for the longitudinal motion. The pair of arrows in a) at the center denotes the shear dislocation. (Modified from Aki and Richards 1980; with kind permission of the authors).

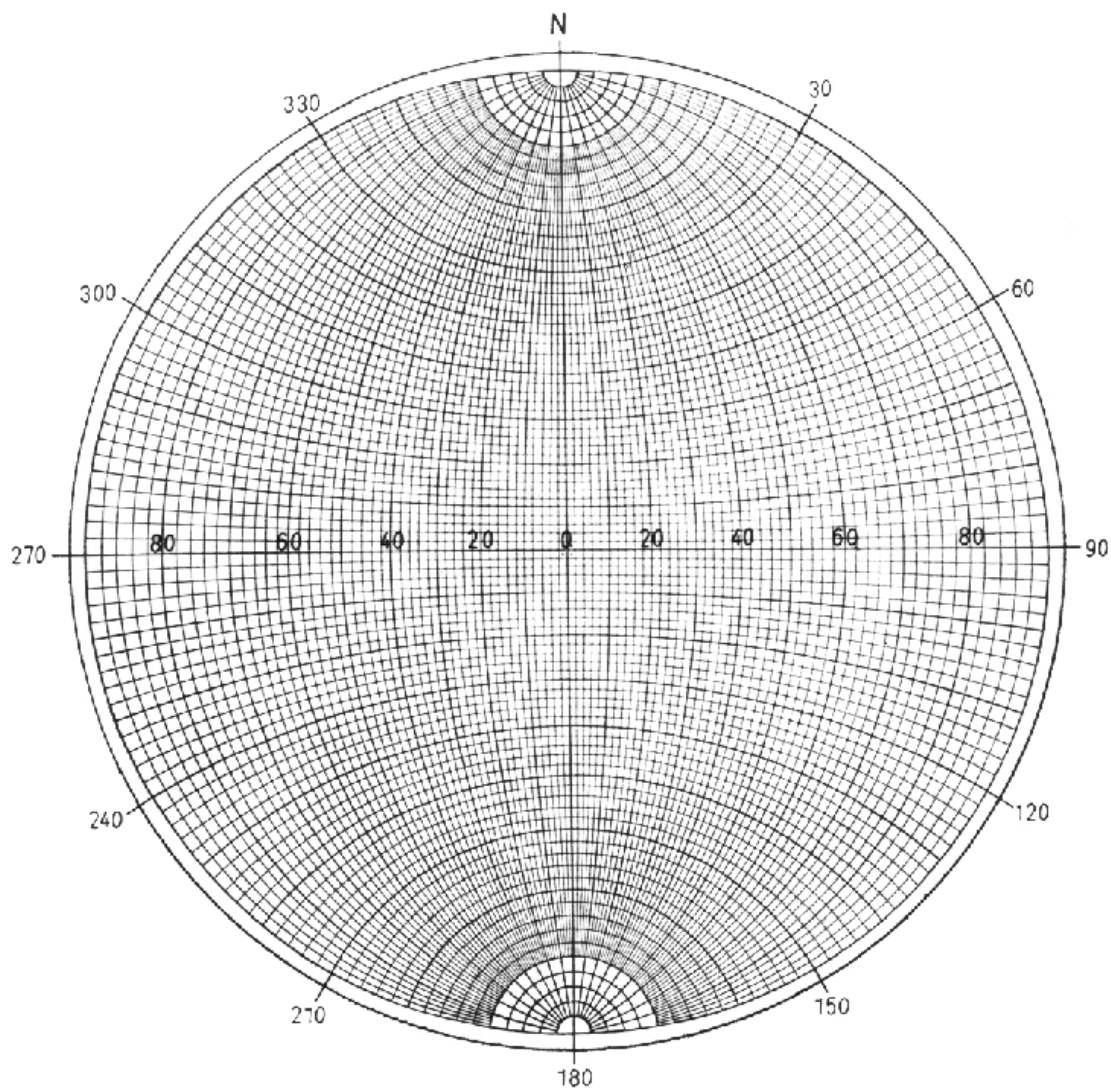
In the case of a double-couple mechanism, according to Fig. 3.22, the S-wave amplitude pattern follows the relationship (see Aki and Richards, 1980)

$$A_S = \cos 2\theta \cos \phi \theta - \cos \theta \sin \phi \phi \quad (3.68)$$

with θ and ϕ - unit vectors in θ and ϕ direction, A_S - shear-wave displacement vector.

3.4.2 Manual determination of fault-plane solutions

Manual fault-plane solutions are normally based on P-wave polarity readings only which are plotted on two kinds of projections, either the equal-angle Wulff net or the Lambert-Schmidt equal area projection (Figs. 3.25a and b; see also Aki and Richards, 1980, Vol. 1, p. 109-110). The latter provides a less cluttered plot of data with take-off angles less than 45° but in principle the procedure of constructing the fault planes is the same (see WS 3.2 and WS 3.3).



The Wulff Net

Fig. 3.25a The equal angle Wulff net.

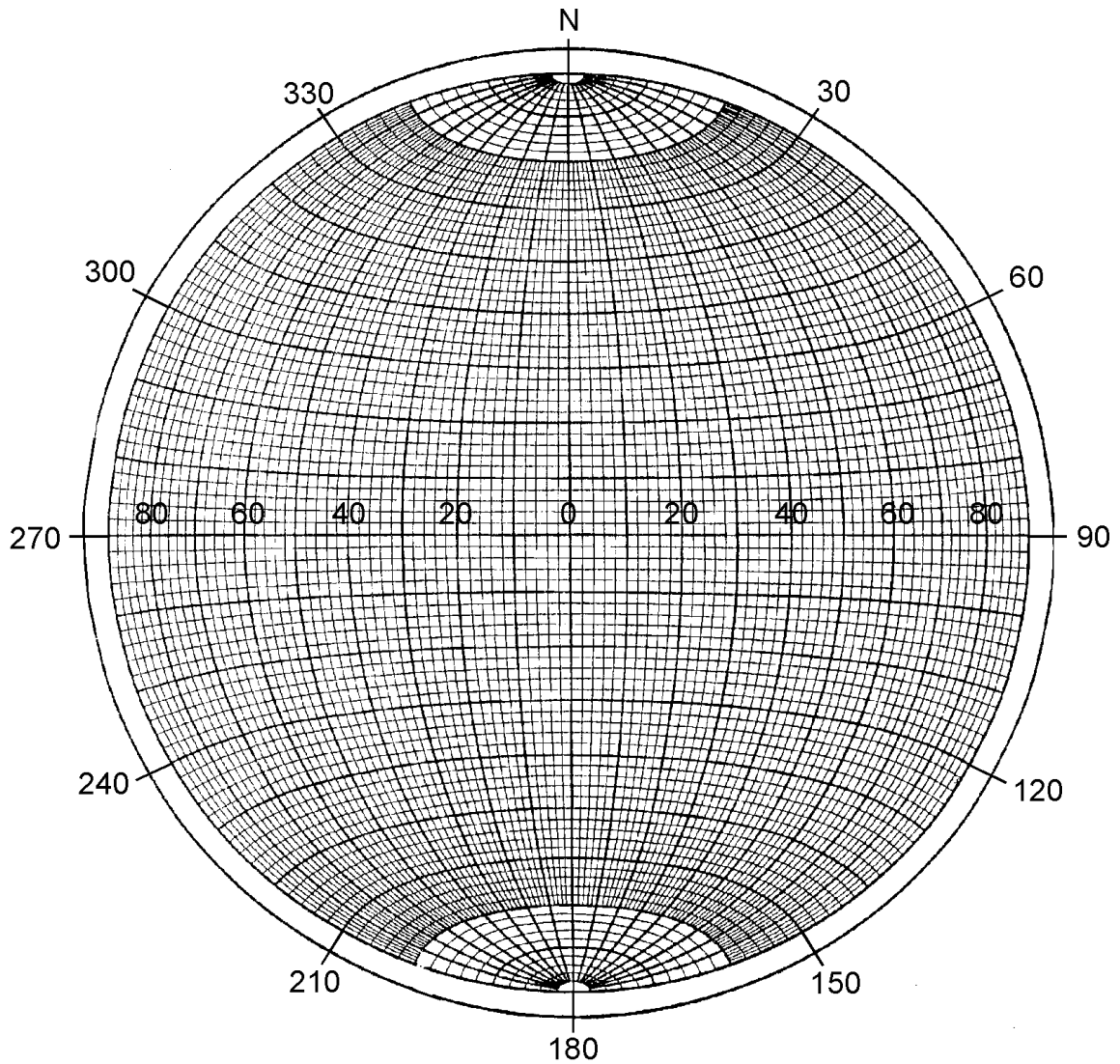


Fig. 3.25b The equal area Lambert-Schmidt net.

To obtain a fault-plane solution basically three steps are required:

- (1) Calculating the positions of the penetration points of the seismic rays through the focal sphere which are defined by the ray azimuth AZM and the take-off angle AIN of the ray from the source.
- (2) Marking these penetration points through the upper or lower hemisphere in a horizontal projection of that sphere using different symbols for compressional and dilatational first arrivals. Usually, lower hemisphere projections are used. Rays which have left the upper hemisphere have to be transformed into their equivalent lower hemisphere ray. This is possible because of spherical symmetry of the radiation pattern (see Figs. 3.26 and 3.27).
- (3) Partitioning the projection of the lower focal sphere by two perpendicular great circles which separate all (or at least most) of the + and - arrivals in different quadrants.

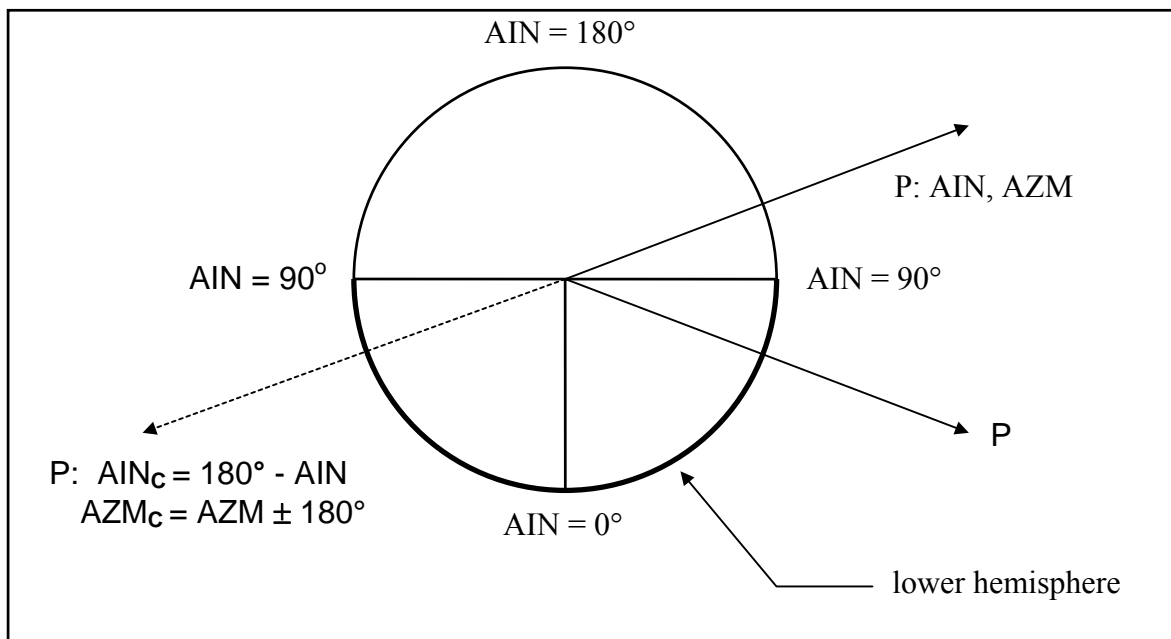


Fig. 3.26 Transformation of a ray leaving the focal sphere upwards into an equivalent downward ray with same polarity and changed incidence angle and azimuth.

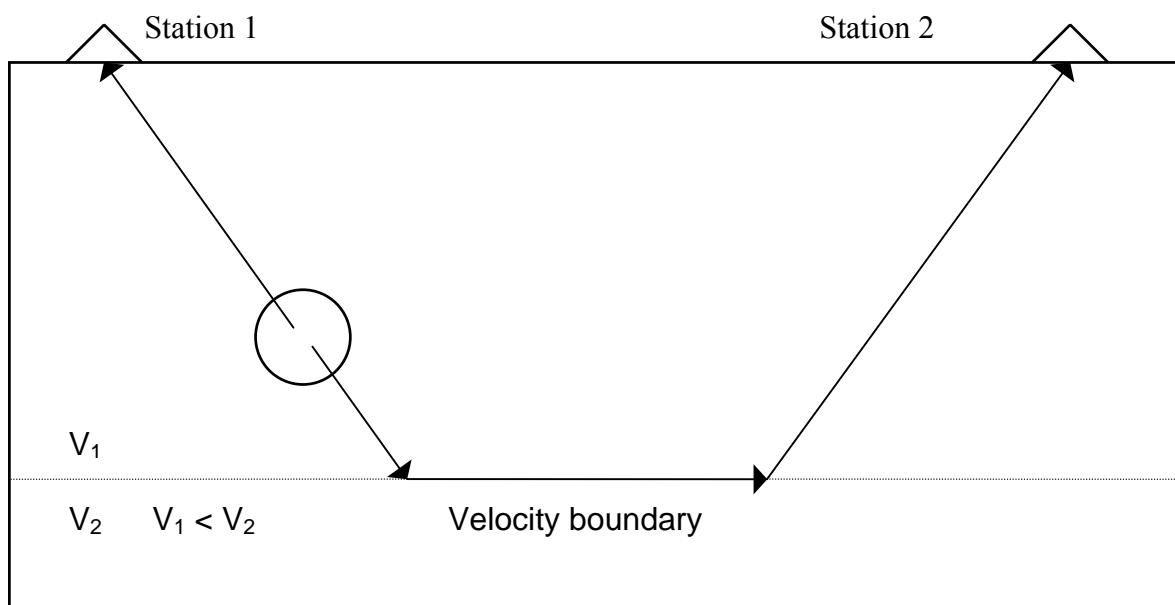


Fig. 3.27 (below): Two rays, leaving the focal sphere in opposite directions, reach - because of the symmetry of radiation pattern - the stations 1 and 2 with the same polarity. The crossing point of the up-going ray with the focal sphere can, therefore, be remapped according to the formulae given in Fig. 3.26 into a crossing point with the lower hemisphere which coincides with the ray crossing-point for station 2.

Fig. 3.28 shows the angles which describe the orientation and motion of a fault plane and Fig. 3.29 shows their determination in the net projections. The **strike angle** ϕ is measured clockwise against North ($0^\circ \leq \phi \leq 360^\circ$). To resolve the 180° ambiguity, it is assumed that when looking into the strike direction the fault dips to the right hand side (i.e., its fault-trace projection is towards the right of the net center). The **dip angle** δ describes the inclination of the hanging wall against the horizontal ($0^\circ \leq \delta \leq 90^\circ$). The **rake angle** λ describes the displacement of the hanging wall relative to the foot wall ($-180^\circ \leq \lambda \leq 180^\circ$). $\lambda = 0$ corresponds to slip in strike direction, $\lambda > 0$ means upward motion of the hanging wall (i.e., *reverse or thrust faulting component*) and $\lambda < 0$ downward motion (i.e., *normal faulting component*).

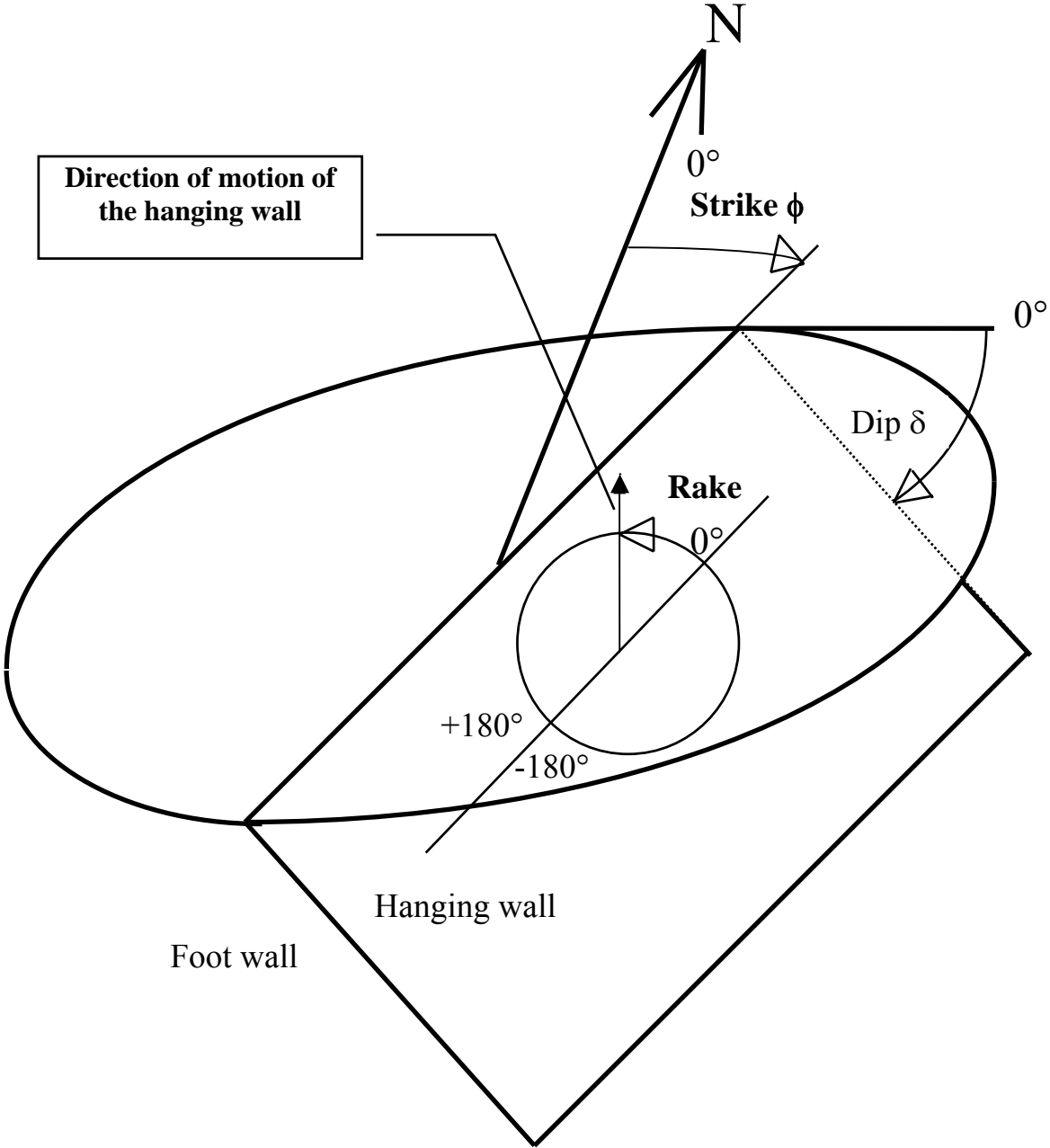


Fig. 3.28 Angles describing the orientation and motion of faults (see text).

In Fig. 3.29 P1, P2 and P3 mark the positions of the poles of the planes FP1 (fault plane), FP2 (auxiliary plane) and EP (equatorial plane) in their net projections. From Fig. 3.28 it is obvious that all three planes are perpendicular to each other (i.e., 90° apart) and intersect in the poles of the respective third plane, i.e., FP1 and FP2 in P3, FP1 and EP in P2 etc. Note that on the basis of polarity readings alone it can not be decided whether FP1 or FP2 was the active fault. Discrimination from seismological data alone is still possible by requires additional study of the *directivity effects* such as azimuthal variation of frequency (*Doppler effect*), amplitudes and/or waveforms. For sufficiently large shocks these effects can more easily be studied in low-frequency teleseismic recordings while in the local distance range high-frequency waveforms and amplitudes may be strongly influenced by resonance effects due to low-velocity near-surface layers. Seismotectonic considerations or field evidence from surface rupture in case of strong shallow earthquakes may allow us to resolve this ambiguity, too. Figs. 3.30 and 3.31 depict several basic types of earthquake faulting and their related fault-plane solutions in so-called "beach-ball" presentations of the net projections.

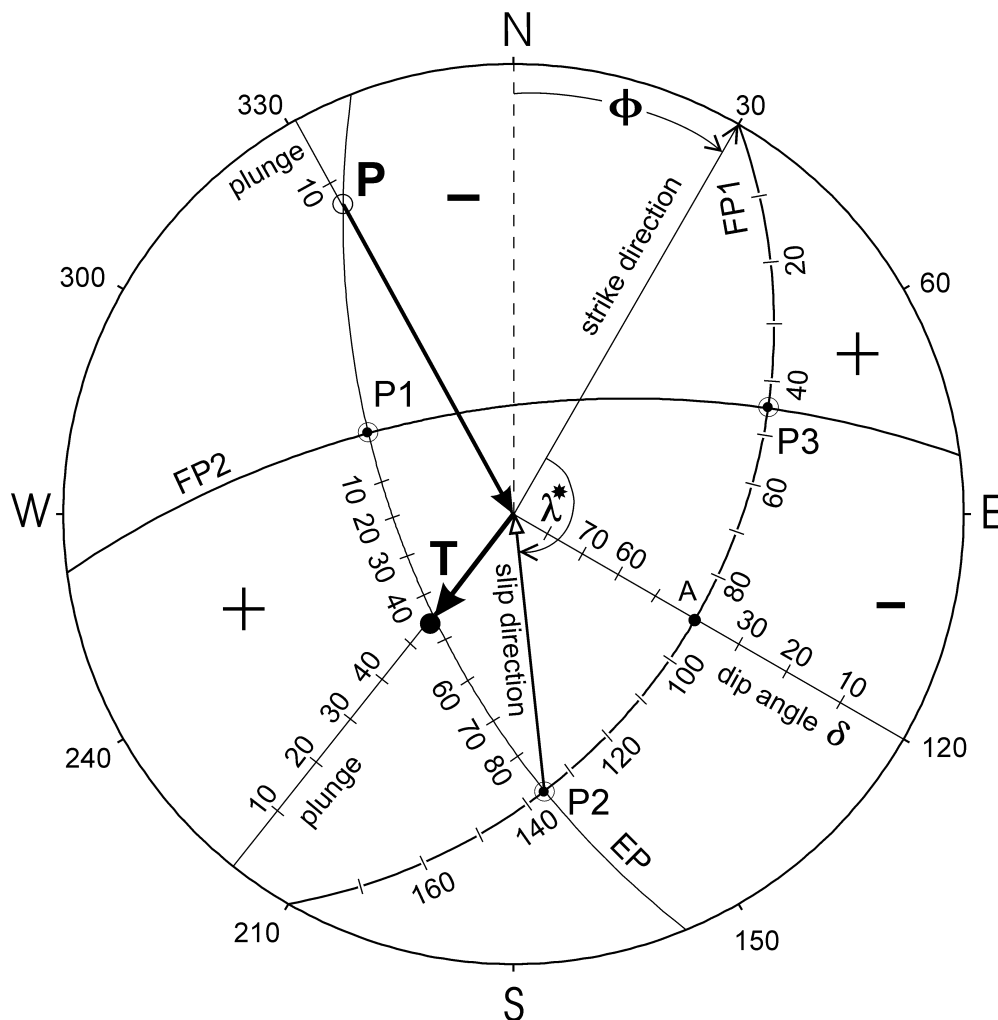
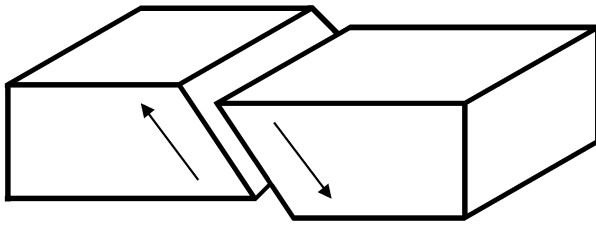
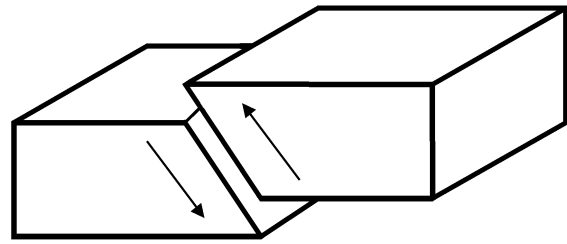


Fig. 3.29 Determination of the fault plane parameters ϕ , δ and λ in the net diagrams. The polarity distribution, slip direction and projection of FP1 shown qualitatively correspond to the faulting case depicted in Fig. 3.28. For abbreviations used see text. **Note:** $\lambda^* = 180^\circ - \lambda$ when the center of the net lies in the tension (+) quadrant (i.e., event with thrust component) or $\lambda^* = -\lambda$ when the center of the net lies in the pressure quadrant (i.e., event with normal faulting component).



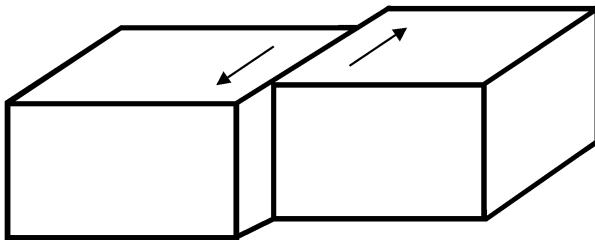
Pure normal faulting

dip $0^\circ < \delta < 90^\circ$; rake = -90°

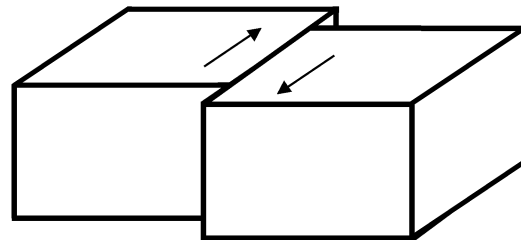


Pure thrust faulting

dip $0^\circ < \delta < 90^\circ$; rake = $+90^\circ$

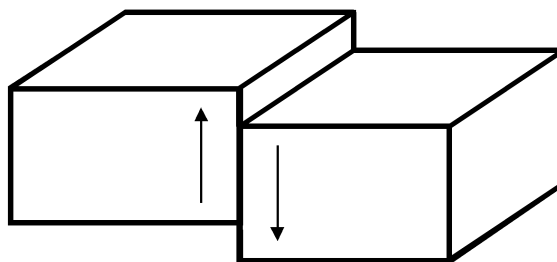


Pure strike slip
left lateral



Pure strike slip
right lateral

dip = 90° rake = 0° and 180° , respectively



Down slip

dip = 90° rake = $\pm 90^\circ$

Fig. 3.30 Basic types of earthquake faulting for some selected dip and rake angles. Note that mixed types of faulting occur when $\lambda \neq 0, 180^\circ$ or $\pm 90^\circ$, e.g., normal faulting with strike-slip component or strike-slip with thrust component. Also, dip angles may vary between $0^\circ < \delta \leq 90^\circ$. For fault plane traces and polarity distributions of these faulting types in their "beach-ball presentation" see Fig. 3.31.

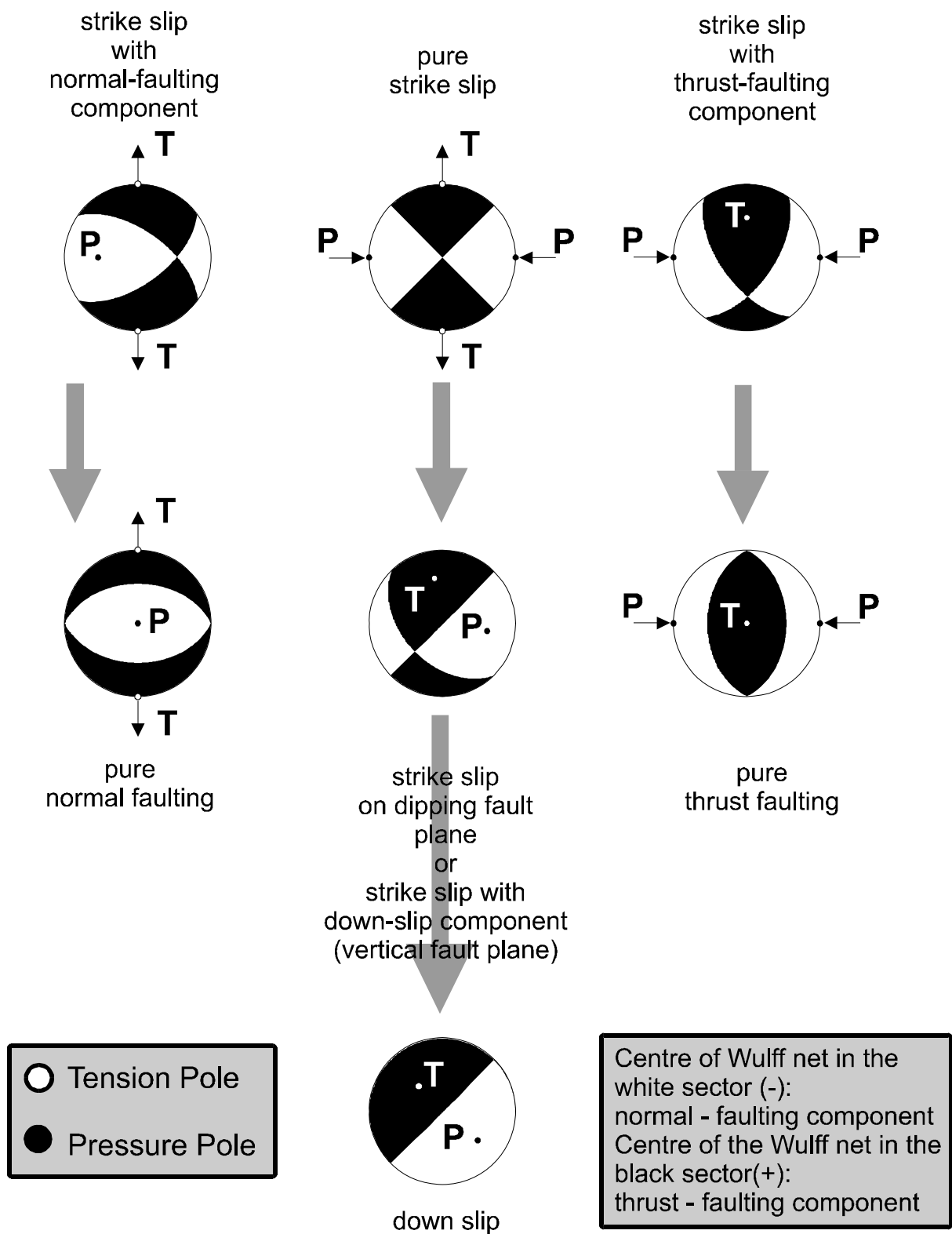


Fig. 3.31 Beach-ball presentation of the net projections of the fault plane cut-traces and of the penetration points of the T-and P-axes through the lower focal hemisphere for different faulting mechanisms. White sectors correspond to negative and black sectors to positive first-motion polarities.

3.4.3 Accuracy of fault-plane solutions

Fault planes determined by eye-fit to the polarity data may be uncertain by about $\pm 10^\circ$. This is acceptable. Even computer assisted best fits to the data will produce different acceptable solutions within about the same error range with only slightly different standard deviations (see, e.g., Fig. 1 in WS 3.3, NEIC and HRVD solutions, respectively).

In addition, one has to be aware that different fitting algorithm or error-minimization procedures may produce different results within this range of uncertainty for the same data. A poor distribution of seismograph stations (resulting in insufficient polarity data for the net diagram), erroneous polarity readings and differences in model assumptions (e.g., in the velocity models used) may result in still larger deviations between the model solution and the actual fault planes. One should also be aware that the assumed constant angular (45°) relationship between the fault plane on the one hand and the pressure and tension axis on the other hand is true in fact only in the case of a fresh rupture in a homogeneous isotropic medium. It may not be correct in the stress environment of real tectonic situations (i.e., P and $T \neq \sigma_1$ and $-\sigma_3$, respectively; see discussion in sub-section 3.1.2.4).

Topic	Determination of fault plane solutions
Authors	Michael Baumbach, and Peter Bormann, Geoforschungszentrum Potsdam, Division 2: Solid Earth Physics and Disaster Research, Telegrafenberg, D-14473 Potsdam, Germany, Fax: +49 331 288 1204; E-mail: baum@gfz-potsdam.de
Version	September 1999

1.1 Aim

The exercise aims at:

- Understanding how fault slip affects the polarities of P-waves;
- Understanding the presentation of P-wave polarities in an equal angle (Wulff net) or equal area projection (Lambert-Schmidt net) of the focal sphere;
- Constructing a fault-plane solution and the related parameters (P- and T-axes, displacement vector) for a real earthquake;
- Relating the fault-plane solution to the tectonic setting of the epicentral area.

2 Data and procedures

Before a fault-plane solution for a teleseismic event can be constructed, the following steps must be completed:

- a) Interpretation of P-wave first-motion polarities from seismograms at several stations;
- b) Calculation of epicentral distances and source-to-station azimuths for these stations;
- c) Calculation of the take-off angles for the seismic P-wave rays leaving the hypocenter towards these stations. This requires the knowledge of the focal depth and of the P-wave velocity at this depth (see EX 3.3).

For the calculations b) and c) standard Earth velocity models are used (e.g., Kennett, 1991).

In the case of local events it is necessary to determine which branch of the travel-time curve is arriving first. The events should be located, if possible, with a special layered crustal velocity model for that region. Most such programs provide both the source-station azimuths and take-off angles in their output files.

The exercise below is based on the definitions, relationships and diagrams (Figs. 3.27 – 3.33) given in the NMSOP, Chapter 3, section 3.4.2 “Manual determination of fault plane solutions.”. As an example consider the data in Table 1 that was determined following steps a)-c), by using the program HYPO71, for a locally recorded aftershock of the Erzincan earthquake in Turkey (Date: 12.04.1992, $M_l = 2.8$, latitude = 39.519° N, longitude = 39.874° E, source depth $h = 3$ km; station distance up to 50 km).

Note: The take-off angles, A_{IN} , calculated for a ray arriving at a given seismic station may vary significantly depending on the assumed velocity model in the source region. Also, for an average single layer crustal model of 30 to 40 km thickness, all P-wave first arrivals within a distance of about 120 - < 200 km are P_g and up-going. That is, they emerge only from the upper half of the focal hemisphere. Also, when using HYPO71 with the average global two-layer crust according to the velocity model IASP91 (Kenneth 1991) only upper hemisphere take-off angles would have been calculated for the first P-wave arrivals up to distances of 50

km. But in the epicentral area under consideration a significant velocity increase in the upper crust was already found at 4 km depth (increase of $v_p = 5.3$ km/s to 6.0 km/s). Accordingly, stations up to 50 km distance were reached by upper or lower focal sphere rays (see Fig. 3.29). Since only lower hemisphere projections will be used in the exercise values, for upper hemisphere rays ($AIN > 90^\circ$) must be corrected according to Fig. 3.28. **Conclusion:** AIN calculations based on strongly biased velocity models might result in inconsistent fault-plane solutions or not permit a proper separation of polarity readings into quadrants at all!

Table 1 gives the needed primary data. They were taken from the output file of the program HYPO71 with which the event was located. The first five columns of this file contain, as an example for the two stations ALI and ESK in Tab. 1, the following data:

STN	DIST	AZM	AIN	PRMK
ALI	3.7	40	130	IPD0
ESK	22.7	312	62	IPU1

with STN - station code; DIST - epicentral distance in km; AZM - azimuth towards the station clockwise in degree from north; AIN - take-off angle of the ray towards the station, measured as in Fig. 3.28, and calculated for the given structure-velocity model; PRMK - P-wave reading remarks. In the column PRMK P stands for P-wave onset, I for impulsive (sharp) or E for emergent (less clear) onset, D for clear (or - for poor) dilatational (downward) first motion, U for clear (or + for poor) compressional (upward) first motion as read at the station. The last character may range between 0 and 4 and is a measure of the quality (clarity) of the onset and thus of the weight given to the reading in the calculation procedure, e.g., 4 for zero and 0 for full weight. In case of the above two stations the values for ALI would need to be corrected to get the respective values for the equivalent lower hemisphere ray, i.e., $AINc = 180^\circ - 130^\circ = 50^\circ$ and $AZMc = 180^\circ + 40^\circ = 220^\circ$ while the values for ESK can be taken unchanged from the HYPO71 output file.

3.3 Tasks

Task 1:

If in Table 1 $AIN > 90^\circ$, then correct take-off angles and azimuths for lower hemisphere projection: $AINc = 180^\circ - AIN$, $AZMc = AZM(<180^\circ) + 180^\circ$ or $AZM(\geq 180^\circ) - 180^\circ$. In case of $AIN < 90^\circ$ the original values remain unchanged.

Task 2:

Place tracing paper or a transparency sheet over the Wulff or Lambert-Schmidt net projection (see Fig. 3.27a or b in 3.4.2). Mark on it the center and perimeter of the net as well as the N, E, S and W directions. Pin the marked sheet center with a needle to the center of the net.

Task 3:

Mark the azimuth of the station on the perimeter of the transparency and rotate the latter until the tick mark is aligned along an azimuth of 0° , 90° , 180° or 270° . Measure the take-off angle from the center of the net along this azimuth. This gives the intersection point of the particular P-wave ray with the lower hemisphere. Mark on this position the P-wave polarity with a neat + for compression or o for dilatation (U or D in Tab. 1) using *different colors* for better distinction of closely spaced polarities of different sign. **Note:** The proper distance (d) of the polarity entry from the center of the net corresponds to $d = r \times \tan(AIN / 2)$ for the Wulff net

and $d = r \times \sin(AIN / 2)$ for the Lambert-Schmidt net with r the radius of the given net. In case that rays left the source through the upper hemisphere ($AIN > 90^\circ$) $AINc$ for lower hemisphere projection has to be calculated and used!

Table 1 Original and corrected values of ray azimuth (AZM and AZMc) and take-off angles (AIN and AINc) towards stations of a temporary network which recorded the Erzincan aftershock of April 12, 1994. POL - polarity of P-wave first motions.

STA	AZM (degree)	AIN (degree)	POL	AZMc (degree)	AINc (degree)
ALI	40	130	D		
ME2	134	114	D		
KAN	197	112	D		
YAR	48	111	D		
ERD	313	103	D		
DEM	330	102	D		
GIR	301	102	U		
UNK	336	101	D		
SAN	76	62	U		
PEL	327	62	D		
GUN	290	62	U		
ESK	312	62	U		
SOT	318	62	D		
BA2	79	62	U		
MOL	297	62	U		
YUL	67	62	U		
ALT	59	62	D		
GUM	320	62	U		
GU2	320	62	D		
BAS	308	62	D		
BIN	295	62	U		
HAR	24	62	D		
KIZ	311	62	U		
AKS	284	62	D		
SUT	295	62	U		

Task 4:

By rotating the transparent sheet with the plotted data over the net try to find a great circle which separates as good as possible the expected quadrants with different first motion signs. This great circle represents the intersection trace of one of the possible fault (or nodal) planes (FP1) with the lower half of the focal sphere. **Note 1:** All N-S connecting lines on both nets are great circles! **Note 2:** Inconsistent polarities that are close to each other may be due to

uncertainty in reading relatively small P-wave amplitudes. The phenomenon occurs particularly for takeoff angles near nodal (fault) planes. Thus, clusters of inconsistent polarities may guide you in finding the best separating great circle. However, be aware that isolated inconsistent polarities might be due to false polarity switching or erroneous first motion polarity reading at the seismic station.

Task 5:

Mark point A at the middle of FP1 and find, on the great circle perpendicular to it, the pole P1 of FP1, 90° apart (see Fig. 3.31). All great circles, passing this pole are perpendicular to the FP1. Since the second possible fault plane (FP2) must be perpendicular to the FP1, it has to pass P1. Find, accordingly, FP2 which again has to separate areas of different polarity.

Task 6:

Find the pole P2 for FP2 (which is on FP1!) and delineate the equatorial plane EP. The latter is perpendicular to both FP1 and FP2, i.e., a great circle through the poles P1 and P2. The intersection point of FP1 and FP2 is the pole of the equatorial plane (P3).

Task 7:

Mark the position of the pressure and tension axes on the equatorial plane and indicate their direction towards (P) and from the center (T) of the considered net (see Fig. 3.31). Their positions on the equatorial plane lie in the center of the respective dilatational (- for P) or compressional (+ for T) quadrant, i.e., 45° away from the intersection points of the two fault planes with the equatorial plane. **Note:**

All angles in the net projections have to be measured along great circles!

Task 8:

Mark the slip vectors, connecting the intersection points of the fault planes with the equatorial plane, with the center of the considered net. If the center lies in a tension quadrant, then the slip vectors point to the net center (see Fig. 3.31). If it lies in a pressure quadrant, then the slip vector points in the opposite direction. The slip vector shows the direction of displacement of the hanging wall.

Task 9:

Determine the azimuth (strike direction ϕ) of both FP1 and FP2. It is the angle measured clockwise against North between the directional vector connecting the center of the net with the end point of the respective projected fault trace lying towards the right of the net center (i.e., with the fault plane dipping towards the right; see Fig. 3.31).

Task 10:

Determine the dip angle δ (measured from horizontal) for both FP1 and FP2 by putting their projected traces on a great circle. Measure δ as the difference angle from the outermost great circle towards the considered fault plane trace.

Task 11:

Determine the slip direction (i.e., the sense of motion along the two possible fault planes. It is obtained by drawing one vector each from the center of the net to the poles P1 and P2 of the

nodal planes (or vice versa from the poles to the center depending on the sign of the rake angle λ). The vector from (or to) the center to (or from) P1 (P2) shows the slip direction along FP2 (FP1). The rake angle λ is positive in case the center of the net lies in the tension (+) quadrant (i. e. an event with a thrust component) and negative when it lies in the pressure (-) quadrant (event with a normal faulting component). In the first case λ is $180^\circ - \lambda^*$. λ^* has to be measured on the great circle of the respective fault plane between its crossing point with the equatorial plain and the respective azimuth direction of the considered fault plane (see Fig. 3.31). In the second case $\lambda = -\lambda^*$. For a pure strike slip motion ($\delta = 90^\circ$) $\lambda = 0$ defines a left lateral strike-slip and $\lambda = 180^\circ$ defines a right-lateral strike-slip.

Task 12:

The azimuth of the pressure and the tension axes, respectively, is equal to the azimuth of the line connecting the center of the net through the P and T point with the perimeter of the net. Their plunge is the dip angle of these vectors against the horizontal (to be measured as for δ).

Task 13:

Estimate the parameters of the fault planes and of the stress axes for the Erzincan aftershock and insert your results into Table 2 below:

Table 2

	strike	dip	rake
Fault plane 1			
Fault plane 2			

	azimuth	plunge
Pressure axis		
Tension axis		

Note: The angles may range between:

- $0^\circ < \text{strike} < 360^\circ$
- $0^\circ < \text{azimuth} < 360^\circ$
- $0^\circ < \text{dip} < 90^\circ$
- $0^\circ < \text{plunge} < 90^\circ$
- $-180^\circ < \text{rake} < 180^\circ$

Task 14:

The question of which of the nodal planes was the active fault plane, and hence the other was the auxiliary plane, cannot be answered on the basis of the fault-plane solution alone. Considering the event in its seismotectonic context may give an answer. Therefore, we have marked the epicenter of the event in Figure 1 with an open star at the secondary fault F2.

- a) Decide which was the likely fault plane (FP1 or FP2)?
- b) What was the type of faulting?
- c) What was the direction of slip? and

d) Is your solution compatible with the general sense of plate motion in the area as well with the orientation of the acting fault and the orientation of stress/deformation in the area?

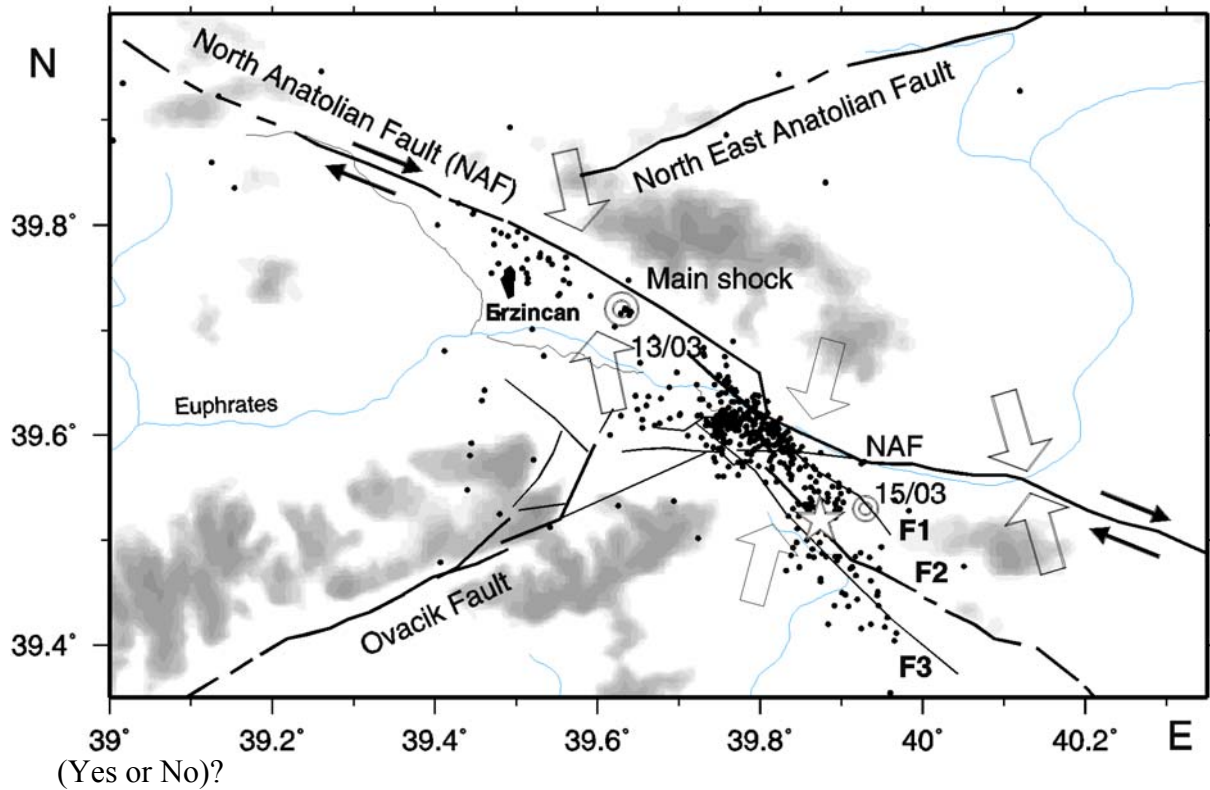


Figure 1 Epicenters of aftershocks between March 21 and June 16, 1992 of the March 13, 1992 Erzincan earthquake, Turkey. The open circles represent the main shock and its strongest aftershock on March 15, and the open star the analyzed aftershock. **F1**, **F2** and **F3** are secondary faults to the North Anatolian Fault (NAF). Black arrows - directions of relative plate motion, open arrows - direction of maximum horizontal compression as derived from centroid moment tensor solutions of stronger earthquakes (courtesy of H. Grosser).

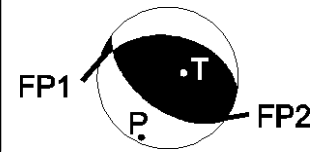
4 Solutions

In the Table 3 below the authors have given the data for their own freehand fits together with the values for the best PC fit to the data (in brackets). If your manually determined results differ by more than about 20° or even show a different type of faulting mechanism, you should critically check your data entries and/or fault-plane fits again.

Table 3

	strike	dip	rake
Fault plane 1 (FP1)	280° (278.5°)	40° (39.9°)	68° (67.4°)
Fault plane 2 (FP2)	130° (127.0°)	54° (53.7°)	108° (107.8°)

	azimuth	plunge
Pressure axis	205° (204.4°)	7° (7.1°)
Tension axis	90° (88.6°)	73° (74.0°)



The answers to the questions in Task 14 are:

- a) FP2 was more likely the active fault.
- b) The aftershock was a thrust event with a very small right-lateral strike-slip component.
- c) The slip direction is here strike - rake azimuth, i.e., for FP2 $130^\circ - 108^\circ = 12^\circ$ from north. This is close to the direction of maximum horizontal compression (15°) in the nearby area as derived from centroid moment tensor solutions of stronger events.
- d) The strike of FP2 for this event agrees with the general direction of mapped surface fault strike and is consistent with the tendency of plate motion direction in the area under study. Therefore, it is highly probable that FP2 was the acting fault.

Topic	Determination of source parameters from seismic spectra
Authors	Michael Baumbach, and Peter Bormann, Geoforschungszentrum Potsdam, Division 2: Solid Earth Physics and Disaster Research, Telegrafenberg, D-14473 Potsdam, Germany, Fax: +49 331 288 1204; E-mail: baum@gfz-potsdam.de
Version	September 1999

1 Aim

This exercise shows how to estimate the source parameters seismic moment, size of the rupture plane, source dislocation and stress drop from data in the frequency domain only and how the results depend on the underlying model assumptions. These parameters could also be estimated in the time domain. However, for estimation in the time domain the records have to be converted into true ground motion (displacement) records. This may be a problem if the bandwidth of the recording system is limited (e.g., short-period records) or if the phase response of the system is not well known. For estimation in the frequency domain only the amplitude response of the instrument is needed.

2 Data

Figure 1 shows a velocity record (vertical component) of an aftershock of the 1992 Erzincan earthquake (Turkey). Figure 2 shows the corresponding *displacement spectrum* of the P-wave. The calculated spectrum was corrected for the amplitude response of the recording system (which includes both response of the velocity seismometer and the anti-aliasing filter of the recorder). Furthermore, the P-wave spectrum was corrected for attenuation, $\exp(i\omega t/2Q_p)$. Q_p had been estimated beforehand from coda Q_c - observations in the area under study assuming that $Q_p = 2.25 Q_c$. This is a good approximation under the assumption that $v_p/v_s = 1.73$, $Q_c = Q_s$ and the pure compressional Q_κ (κ - bulk modulus) is very large ($\rightarrow \infty$). In Figure 2 also the noise spectrum, treated in the same way as the P-wave spectrum, was computed and plotted in order to select the suitable frequency range for analysis (with signal-to-noise ratio $SNR > 3$).

At low frequencies typical P- and S-wave spectra approach a constant amplitude level u_0 and at high frequencies the spectra show a decay that falls off as f^{-2} to f^{-3} . Plotted on a log-log scale the spectrum can be approximated by two straight lines. The intersection point is the corner frequency f_c . u_0 and f_c are the basic spectral data from which the source parameters will be estimated. Event and material data required for further calculations are the epicentral distance Δ , the source depth h , the rock density ρ , the P-wave velocity v_p , and the averaged radiation pattern Θ for P-waves. Respective values are given under 3.1 below. Other needed parameters can then be calculated.

Note: The apparent increase of spectral amplitudes in Figure 2 for $f > 35$ Hz is not real but due to antialiasing filtering of the record. Thus, this increase should not be considered in the following analysis.

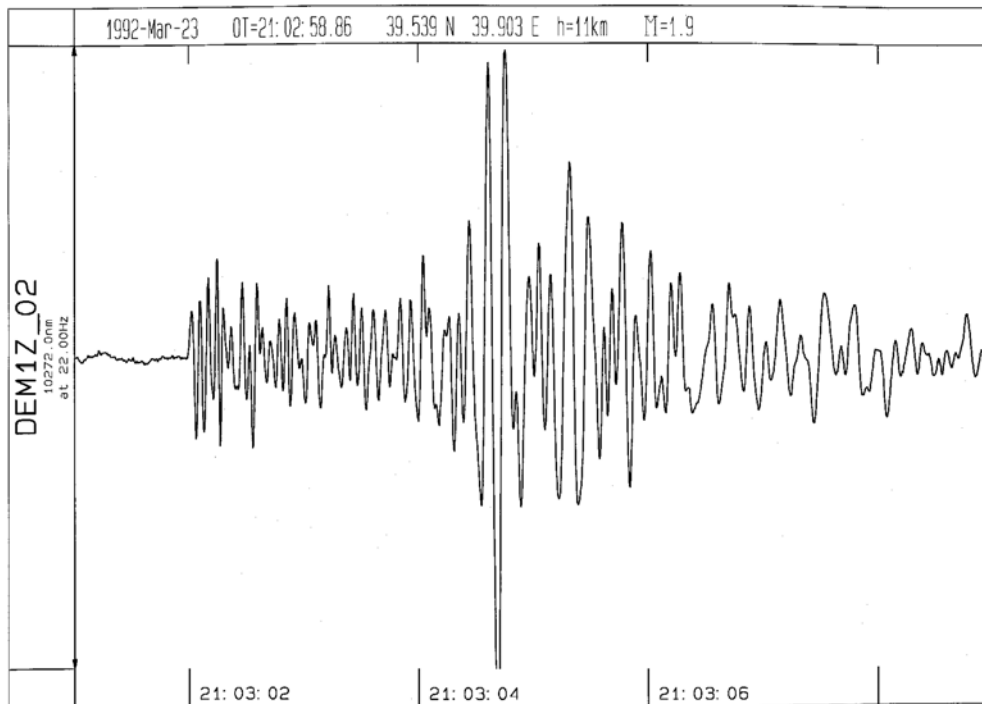


Figure 1 Record of an Erzincan aftershock (vertical component). For the indicated P-wave window the displacement spectrum shown in Figure 2 has been calculated.

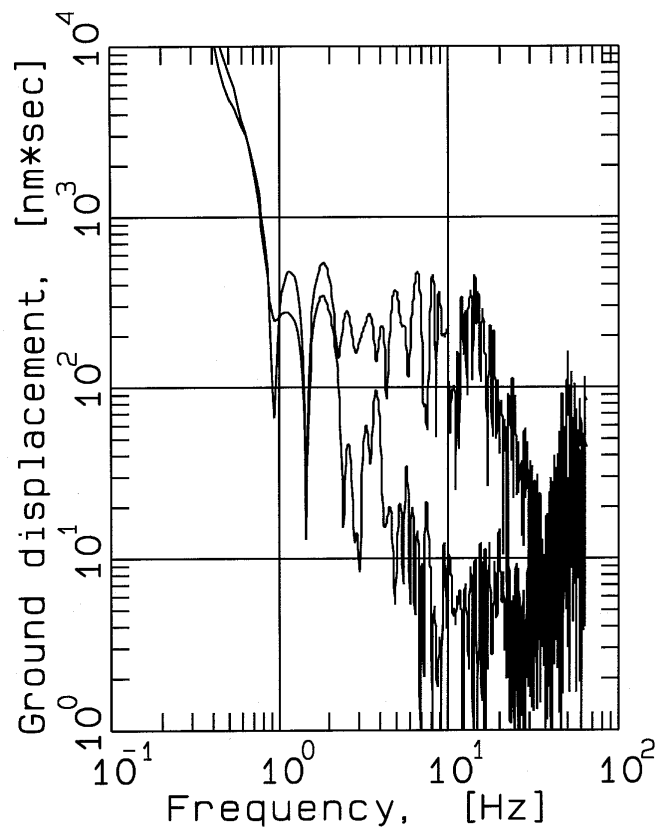


Figure 2 P-wave (upper curve) and noise spectrum (lower curve) of the record shown in Figure 1, corrected for the instrument response and attenuation.

3 Procedures

The parameters to be estimated are:

- Seismic moment $M_0 = \mu \bar{D} A$ (1)
(with μ - shear modulus; \bar{D} - average source dislocation, and A - size of the rupture plane)
- Source dislocation \bar{D}
- Source dimension (radius R and area A)
- Stress drop $\Delta\sigma$

The following relationships hold:

3.1 Seismic moment M_0

Under the assumption of a homogeneous Earth model and constant P-wave velocity v_p , the seismic moment M_0 can be determined from the relationship:

$$M_0 = 4 \pi r v_p^3 \rho u_0 / (\Theta S_a) \quad (2)$$

In the case with:

density $\rho = 2.7 \text{ g/cm}^3$

P-wave velocity $v_p = 6 \text{ km/sec}$

source depth $h = 11.3 \text{ km}$

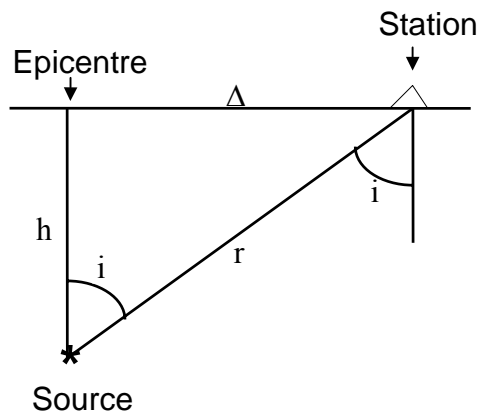
epicentral distance $\Delta = 18.0 \text{ km}$

hypocentral distance (travel path) $r = \sqrt{(h^2 + \Delta^2)}$

incidence angle $i = \arccos(h/r)$

free surface amplification S_a for P-waves

averaged radiation pattern $\Theta = 0.64$ for P-waves.



Note the differences in dimensions used! M_0 has to be expressed in the unit $\text{Nm} = \text{kg m}^2 \text{s}^{-2}$. S_a can be determined by linear interpolation between the values given in Table 1. They were computed for the above given constant values of v_p and ρ (homogeneous model) and assuming a ratio $v_p/v_s = 1.73$. i is the angle of incidence, measured from the vertical.

Table 1 Surface amplification S_a for P-waves; i is the incidence angle.

i	S_a	i	S_a	i	S_a
0	2.00	30	1.70	60	1.02
5	1.99	35	1.60	65	0.90
10	1.96	40	1.49	70	0.79
15	1.92	45	1.38	75	0.67
20	1.86	50	1.26	80	0.54
25	1.79	55	1.14	85	0.35

3.2 Size of the rupture plane

For estimating the size of the rupture plane and the source dislocation one has to adopt a kinematic (geometrical) model, describing the rupture propagation and the geometrical shape of the rupture area. In this exercise computations are made for three different circular models (see Table 2), which differ in the source time function and the crack velocity v_{cr} . v_s is the S-wave velocity, which is commonly assumed to be $v_s = v_p / \sqrt{3}$.

Table 2 Parameters of some commonly used kinematic rupture models.

1. Brune (1970)	$v_{cr} = 0.9 V_s$	$K_p = 3.36$	$K_s = 2.34$
2. Madariaga I (1976)	$v_{cr} = 0.6 V_s$	$K_p = 1.88$	$K_s = 1.32$
3. Madariaga II (1976)	$v_{cr} = 0.9 V_s$	$K_p = 2.07$	$K_s = 1.38$

The source radius R (in m) can then be computed from the relationship

$$R = v_s K_{p/s} / 2\pi f_{c_{p/s}} \quad (3)$$

with v_s – shear-wave velocity in km/s, $f_{c_{p/s}}$ - corner frequency of the P- or S-waves, respectively, in Hz and K_p and K_s being the related model constants and v_s . The differences in K_p and K_s between the various models are due to different assumptions with respect to crack velocity and the rise time of the source-time function. Only K_p has to be used in the exercise (P-wave record!). The size of the circular rupture plane is then

$$A = \pi R^2. \quad (4)$$

3.3 Average source dislocation \bar{D}

According to (1) the average source dislocation is

$$\bar{D} = M_0 / (\mu A). \quad (5)$$

Assuming $v_s = v_p/1.73$ it can be computed knowing M_0 , the source area A and the shear modulus $\mu = v_s^2 \rho$.

3.4 Stress drop

The static stress drop $\Delta\sigma$ describes the difference in shear stress on the fault plane before and after the slip. According to Keilis Borok (1959) the following relationship holds for a circular crack with a homogeneous stress drop:

$$\Delta\sigma = 7 M_0 / (16 R^3). \quad (6)$$

The stress drop is expressed in the unit of Pascal, $\text{Pa} = \text{N m}^{-2} = \text{kg m}^{-1} \text{s}^{-2} = 10^{-5} \text{ bar}$.

4 Tasks

Task 1:

Select in Figure 2 the frequency range f_1 to f_2 that can be used for analysis ($\text{SNR} > 3$):

$$f_1 = \dots\dots\dots \text{ Hz}$$

$$f_2 = \dots\dots\dots \text{ Hz}$$

Task 2:

Estimate the low-frequency level, u_0 , of the spectrum by approximating it with a horizontal line. Note in Figure 2 the logarithmic scales and that the ordinate dimension is $\text{nm s} = 10^{-9} \text{ m s}$.

$$u_0 = \dots\dots\dots \text{ m s}$$

Task 3:

Estimate the exponent, n , of the high frequency decay, f^{-n} ; mark it by an inclined straight line.

$$n = \dots\dots\dots$$

Task 4:

Estimate the corner frequency, f_{c_p} (the intersection between the two drawn straight lines).

$$f_{c_p} = \dots\dots\dots \text{ Hz}$$

Task 5:

Calculate from the given event parameters and relationships given in 3.1 and Table 1 the values for:

$$r = \dots\dots\dots \text{ km}$$

$$i = \dots\dots\dots^\circ$$

$$S_a = \dots\dots\dots$$

$$M_0 = \dots\dots\dots \text{ Nm}$$

Task 6:

Using the equations (3), (4), (5) and (6) calculate for the three circular source models given in Table 2 the parameters

- source radius R and source area A ,
- shear modulus μ and average displacement \bar{D} and
- stress drop $\Delta\sigma$.

Write the respective values in Table 3

Table 3

Model	R [m]	A [m ²]	\bar{D} [m]	$\Delta\sigma$ [MPa]
1. Brune				
2. Madariaga I				
3. Madariaga II				

Note: Since $\Delta\sigma \sim R^{-3}$ the estimate of stress drop very much depends on f_c , a parameter which can not be estimated very precisely from real spectral data. In the case of non-circular, e.g., rectangular fault ruptures, two corner frequencies may exist which are controlled by the width W and the length L of the rupture plane. In addition, differences in the assumed mode of crack propagation (e.g., unilateral, bilateral, or radial) and the velocity of crack propagation, v_{cr} , influence the parameters calculated from spectral data (see Information Sheet IS 3.1). Accordingly, stress drop values may be, in the worst case, uncertain up to about two orders of magnitude. Therefore, in studying possible systematic differences in source parameters derived from spectral data for events in a given area one should always stick to using one type of model. However, one must be reasonably sure about the validity of assuming that the events have similar modes of faulting and crack propagation.

5 Solutions

Although individual visual parameter readings from Figure 2 might be subjective, they should not differ by more than about $\pm 10\%$ from the values given here for tasks 1 to 5 but may be larger for 6. Acceptable average values for the read and calculated parameters are for:

Task 1: $f_1 = 2 \text{ Hz}, \quad f_2 = 30 \text{ Hz}$

Task 2: $u_0 = 3 \times 10^{-7} \text{ m s}$

Task 3: $n = 3$

Task 4: $f_{cp} = 14.4 \text{ Hz}$

Task 5: $r = 21.3 \text{ km} \quad i = 58^\circ, \quad S_a = 1.07, \quad M_0 = 6.8 \times 10^{13} \text{ N m}$

Task 6:

a) $R_1 = 129 \text{ m}, \quad A_1 = 5.23 \times 10^4 \text{ m}^2$
 $R_2 = 72 \text{ m}, \quad A_2 = 1.63 \times 10^4 \text{ m}^2$
 $R_3 = 79 \text{ m}, \quad A_3 = 1.96 \times 10^4 \text{ m}^2$

b) $\mu = 3.24 \times 10^{10} \text{ kg m}^{-1} \text{ s}^{-2} \quad D_1 = 4.0 \times 10^{-2} \text{ m}$
 $D_2 = 1.3 \times 10^{-1} \text{ m}$
 $D_3 = 1.1 \times 10^{-1} \text{ m}$

c) $\Delta\sigma_1 = 13.8 \text{ MPa}$
 $\Delta\sigma_2 = 79.7 \text{ MPa}$
 $\Delta\sigma_3 = 60.3 \text{ MPa}$

References

- Brune, J. N. (1970). Tectonic stress and the spectra of shear waves from earthquakes. *J. Geophys. Res.*, **75**, 4997-5009.
- Keilis Borok, V. I. (1959). On the estimation of the displacement in an earthquake source and of source dimensions. *Ann. Geofis.* 19, 205-214.

Madariaga, R. (1976). Dynamics of an expanding circular fault. *Bull. Seismol. Soc. Am.*, **66**, 639-666.